

Department of Electrical and Computer Engineering

Human Gait Analysis Using Inertial Measurement Unit for
Rehabilitation

Han Yi Chiew

This thesis is presented for the Degree of
Doctor of Philosophy
of
Curtin University

December 2019

DECLARATION

To the best of my knowledge and belief this thesis contains no material previously published by any other person except where due acknowledgment has been made.

This thesis contains no material which has been accepted for the award of any other degree or diploma in any university.

Human Ethics The research presented and reported in this thesis was conducted in accordance with the National Health and Medical Research Council National Statement on Ethical Conduct in Human Research (2007) – updated March 2014. The proposed research study received human research ethics approval from the Curtin University Human Research Ethics Committee (EC00262), Approval Number HRE2017-0834.

Signature:

Date: 03/12/2019

To whole of my beloved Han's family for raising and educating me.

ABSTRACT

Walking can become a difficult task for people with impaired gaits such as foot drop and knee osteoarthritis. The assessment of walking can help clinicians to determine and provide optimal care and treatments to patients. Currently, most clinical assessment is done based on visual inspection, which is subjective as it relies on the experience of the clinician. Although optical motion capture system can be used to make accurate estimation of 3-dimensional (3-D) orientation angles of human body parts, it is non-portable, expensive, and complex to set up. Inertial Measurement Units (IMUs), on the other hand, are portable, affordable, and easy to setup.

This research focuses on developing IMU-based gait analysis methods. Low cost IMUs consisting of gyroscopes and accelerometers were first designed and constructed. A new 3-D thigh and shank angles estimation algorithm, called 2-point error estimation algorithm, was then proposed and validated against gold standard Vicon optical motion capture system installed in Motion Analysis Lab of School of Physiotherapy and Exercise Science of Curtin Australia. Next, the estimated 3-D angles were used as input features of several machine learning algorithms to design a real-time standalone gait diagnosis device that lit up green and red LEDs when the gait was normal and abnormal, respectively. Additionally, a novel normal and abnormal gait phase detection method based on a single shank's IMU was proposed and validated against force sensors. The thigh and shank angle waveforms were also mathematically expressed using Fourier series with improved accuracy without increasing the number of harmonics through waveform scaling. The reconstructed waveforms were able to detect the gait phase accurately, while the scaled waveforms were able to increase the gait multi-class classification accuracy. In order to provide joint angle information to the clinicians for visual inspection, a method to temporally synchronize IMU data and video of a person walking was proposed and validated by blinking an LED. Finally, a new stride length estimation algorithm based on linear kinematics using a shank's gyroscope was proposed and validated against the Vicon system.

This thesis presents both applied and fundamental researches. The main contribution is an IMU-based system that detects and classifies a selection of gait anomalies to assist the medical practitioners in diagnosis of walking disorders.

ACKNOWLEDGEMENTS

My supervisors Dr. Kiing Ing Wong and Prof. Iain Murray have provided me invaluable supervision and support throughout my research. Their vision in developing healthcare technology inspired and motivated me in carrying out this research project.

The anonymous journal reviewers of Institute of Electrical and Electronics Engineers (IEEE) have also provided me valuable feedbacks on my works. Their voluntary works are highly appreciated.

I would like to thank to all volunteers who involved in the data collection for this research. Special thanks to Curtin University Australia for the permission to use Vicon optical motion capture system for data collection.

My family members Khim Kiat, Chau Kwang, Yun Ngo, Hee Kwang, Soon Len, Moi Wah, Moi Jee, Moi Heng, Moi Fang, Moi Nam, and Chang Kwang have provided me with great support since I am young. My friends Vicky Lau, Justin Lee, Ayshwarya, Basil Andy, and Hong Hui have also played important roles in making my study life enjoyable.

I would also like to thank the Faculty of Engineering of Curtin University Malaysia for approving my first and a half year tuition fee waiver application. The Higher Degree by Research Department then offers me Curtin Malaysia Postgraduate Research Scholarship which covers my tuition fees and living allowance for the remaining 1.5 years of my study.

TABLE OF CONTENT

ABSTRACT	III
ACKNOWLEDGEMENTS	IV
TABLE OF CONTENT	V
LIST OF FIGURES	X
LIST OF TABLES	XIV
LIST OF ABBREVIATIONS	XVI
LIST OF PUBLICATIONS	XVII
CHAPTER 1 - INTRODUCTION	1
1.1 Introduction	1
1.2 Problem Statements	1
1.3 Objectives	2
1.4 Novel Approaches	3
1.5 Outline	4
CHAPTER 2 - EXISTING TECHNOLOGIES AND LITERATURE REVIEW ON GAIT ANALYSIS	5
2.1 Introduction	5
2.2 Human Gait Cycle	5
2.3 Existing Motion Capture Technology	6
2.3.1 Visual Inspection	6
2.3.2 Force Sensor	6

2.3.3 Optical Motion Capture System	6
2.3.4 Inertial Sensors	7
2.3.4.1 Accelerometer	7
2.3.4.2 Gyroscope	8
2.3.4.3 Magnetometer	8
2.4 Existing Works in Literature	9
2.4.1 Angle Estimation using IMU	9
2.4.2 Gait Diagnosis	10
2.4.3 Gait Phase Detection	12
2.4.4 Gait Modelling	13
2.4.5 Temporal Synchronization of Video and IMU data	14
2.4.6 Stride Length Estimation	16
2.5 Chapter Summary	18
CHAPTER 3 - EXPERIMENTAL PLATFORM	20
3.1 Introduction	20
3.2 Design and Construction of IMUs	20
3.2.1 Hardware	20
3.2.2 Software	23
3.2.3 Data Loss	24
3.3 Force Sensors	25
3.4 Video Capture and IMUs with LED	26
3.5 Vicon Optical Motion Capture System	27
3.5 Chapter Summary	28
CHAPTER 4 - PROPOSED METHODS RELATED TO GAIT ANALYSIS	29
4.1 Introduction	29
4.2 Estimation of 3-D Thigh and Shank Angles using IMU	29

4.2.1 Introduction	29
4.2.2 Experimental Setup	30
4.2.3 Proposed Method	31
4.2.3.1 Overall flowchart	31
4.2.3.2 Starting and Stopping Time of Walking	32
4.2.3.3 Estimation of Accelerometer and Gyroscope Angles	33
4.2.3.4 2-Point Error Estimation Algorithm	34
4.2.4 Results and Discussion	35
4.2.5 Summary	41
4.3 Design and Construction of a Standalone Gait Diagnosis Device	42
4.3.1 Introduction	42
4.3.2 Experimental Setup	42
4.3.3 Proposed Method	45
4.3.3.1 Overall flowchart	45
4.3.3.2 Estimate 3-D Thigh and Shank Angles	45
4.3.3.3 Gait Cycle Extraction in Real Time	46
4.3.3.4 Feature Extraction (Resampling and Normalization)	48
4.3.3.5 Feature and Machine Learning Technique Selection	50
4.3.3.6 Memory Requirement	51
4.3.3.7 Standalone Gait Diagnosis Device based on Perceptron	52
4.3.4 Results and Discussion	54
4.3.5 Summary	64
4.4 Gait Phase Detection	65
4.4.1 Introduction	65
4.4.2 Experimental Setup	65
4.4.3 Proposed Method	67
4.4.3.1 Gait Cycle Extraction	67
4.4.3.2 Gait Phase Detection using Kinetic Parameters (FSRs) for Comparison	68
4.4.3.3 Gait Phase Detection using Shank's IMU for Comparison [50]	71
4.4.3.4 Heel Strike	72
4.4.3.5 Toe Strike	76
4.4.3.6 Toe Off	81

4.4.4 Results and Discussion	82
4.4.5 Summary	87
4.5 Accurate Gait Modelling based on Waveform Scaling before DFT	88
4.5.1 Introduction	88
4.5.2 Experimental Setup	88
4.5.3 Proposed Method	89
4.5.3.1 Gait Cycle Extraction	89
4.5.3.2 Waveform Transformation before DFT	90
4.5.3.3 Waveform Reconstruction	94
4.5.3.4 Possible Application 1: Gait Phase Detection	95
4.5.3.4 Possible Application 2: Gait Classification	95
4.5.4 Results and Discussion	96
4.5.5 Summary	106
4.6 Temporal Synchronization of Markerless Video and IMU Data	107
4.6.1 Introduction	107
4.6.2 Experimental Setup	107
4.6.3 Proposed Method	108
4.6.3.1 IMU Data Processing	108
4.6.3.2 Video Processing	110
4.6.3.3 Synchronization of Video and IMU Data	114
4.6.3.4 Validation of Proposed Method using Blinking LED	118
4.6.4 Results and Discussion	120
4.6.5 Summary	123
4.7 Stride Length Estimation based on a single Shank's Gyroscope	124
4.7.1 Introduction	124
4.7.2 Experimental Setup	124
4.7.3 Proposed Method	125
4.7.4 Results and Discussion	128
4.7.5 Summary	130
CHAPTER 5 – CONCLUSIONS AND FUTURE WORK	131
5.1 Conclusions	131

5.2 Future Work

133

REFERENCES

136

LIST OF FIGURES

Fig. 2.1: Human gait divided into eight sub-phases [6].....	5
Fig. 2.2: Human gait divided into four sub-phases [11].....	5
Fig. 2.3: Accelerometer x , y , and z -axes.	7
Fig. 2.4: Gyroscope angular velocity ω	8
Fig. 3.1: IMUs. (a) External view. (b) Internal view.....	21
Fig. 3.2: Dongle.....	21
Fig. 3.3: Hardware connections of IMUs.....	21
Fig. 3.4: Flowchart for IMU software development.....	23
Fig. 3.5: Format of compiled sensor data.....	23
Fig. 3.6: Flowchart for dongle software development.....	24
Fig. 3.7: IMU data loss with respect to distance.....	25
Fig. 3.8: IMUs with FSRs.	25
Fig. 3.9: FSR circuitry.....	25
Fig. 3.10: Format of compiled sensor data with FSR readings.	26
Fig. 3.11: IMUs with LED.	26
Fig. 3.12: Blinking of LED for validation of proposed method.....	27
Fig. 3.13: Vicon Optical Motion Capture System.	27
Fig. 4.1: Placement of IMUs.....	30
Fig. 4.2: Flowchart to estimate flexion/extension and adduction/abduction angles. .	31
Fig. 4.3: Flowchart to estimate internal/external rotation angle.....	31
Fig. 4.4: Flowchart to identify the starting or stopping time of walking.	33
Fig. 4.5: Estimated 3-D angles of the thigh and shank during normal walking on a flat surface.....	36
Fig. 4.6: Estimated 3-D angles of the thigh and shank during abnormal walking on a flat surface.	37
Fig. 4.7: Error of the estimated thigh and shank angles during normal walking on a flat surface.....	38
Fig. 4.8: IMUs' placement and axes direction.....	43
Fig. 4.9: Placement of IMUs.	43
Fig. 4.10: Standalone gait diagnosis device.....	44
Fig. 4.11: Overall flowchart to train a machine learning method.	45
Fig. 4.12: 3-D thigh and shank angles of a person walking abnormally.....	46
Fig. 4.13: Shank's flexion/extension angles of a normal gait. Dotted purple lines show	

the extracted gait cycle.	47
Fig. 4.14: Resampling and normalization of 3-D angles.	49
Fig. 4.15: Overall flowchart for standalone gait diagnosis device.	53
Fig. 4.16: Perceptron.....	54
Fig. 4.17: Accuracy, Specificity, and Sensitivity of RF and kNN.....	55
Fig. 4.18: Sensors placement.....	66
Fig. 4.19: Placement of IMUs and FSR.	66
Fig. 4.20: Shank’s flexion/extension angle for gait cycle extraction.	67
Fig. 4.21: FSR measurements during normal walking.....	70
Fig. 4.22: Ideal gait phases detected using FSRs.	71
Fig. 4.23: Detection of heel strike and toe off using shank’s angular velocity ω_{shank}	71
Fig. 4.24: Shank’s angular velocity ω_{shank} and ideal gait phases of a volunteer walking with different patterns.....	73
Fig. 4.25: ω_{shank} without 2 nd positive zero crossing.	74
Fig. 4.26: Proposed method to detect and diagnose heel strikes.	75
Fig. 4.27: Proposed method to detect normal toe strikes.	76
Fig. 4.28: Abnormal toe strike (Pattern 1).....	77
Fig. 4.29: Abnormal toe strike (Pattern 2).....	77
Fig. 4.30: Abnormal toe strike (Pattern 3).....	78
Fig. 4.31: Abnormal toe strike (Pattern 4).....	78
Fig. 4.32: Abnormal toe strike (Pattern 5).....	79
Fig. 4.33: Abnormal toe strike (Pattern 6).....	79
Fig. 4.34: Abnormal toe strike (Pattern 7).....	80
Fig. 4.35: Abnormal toe strike (Pattern 8).....	80
Fig. 4.36: Proposed method to detect and diagnose toe strikes.	81
Fig. 4.37: Proposed method to detect toe off using last local maximum of ω_{shank}	82
Fig. 4.38: Illustration of sample difference between proposed method and FSRs [9].	83
Fig. 4.39: Gait sub-phases for different types for walking.	85
Fig. 4.40: Detected gait sub-phases based on proposed method.	86
Fig. 4.41: Angle direction.....	89
Fig. 4.42: Gait cycle extraction using maximum backward swings of shank.	89
Fig. 4.43: Flowchart for waveform transformation before performing DFT.	90

Fig. 4.44: Region extraction for one cycle of an angle waveform.	91
Fig. 4.45: Time and amplitude-scaled waveforms.....	92
Fig. 4.46: Time and amplitude-scaled waveform repeated X times.	93
Fig. 4.47: Single-sided amplitude spectrums of a full cycle of scaled waveform.	93
Fig. 4.48: Flowchart to reconstruct a waveform.....	94
Fig. 4.49: Shank's angular velocity to detect gait phases.....	95
Fig. 4.50: Applying proposed method for gait classification.	96
Fig. 4.51: Plot of mean CORR against thresholds λ for conventional method when $H=6$	98
Fig. 4.52: Plot of mean CORR at Region B against thresholds λ when $H=6$ and 10.	98
Fig. 4.53: Plot of mean CORR against H	99
Fig. 4.54: Original and reconstructed angle waveforms.....	101
Fig. 4.55: Number of computations required per harmonic.	102
Fig. 4.56: Estimated shank's angular velocity to detect gait phases.	104
Fig. 4.57: IMU placement.	108
Fig. 4.58: IMU data processing.....	108
Fig. 4.59: Estimated angle. (a) Shank angle. (b) Foot angle.	109
Fig. 4.60: First maximum backward swing detection. (a) Shank angle. (b) Foot angle.	109
Fig. 4.61: Video processing flowchart.	110
Fig. 4.62: Video paused at a frame. (a) RGB video v . (b) Gray-scaled video g . (c) Detected motion M in black and white.	111
Fig. 4.63: Upper- and lower-part separation. (a) RGB. (b) Detected motion M	111
Fig. 4.64: Approximate extension of leg.....	112
Fig. 4.65: Total number of white pixels in M	113
Fig. 4.66: Estimated maximum backward swings of leg.....	114
Fig. 4.67: Flowchart to synchronize video and IMU data.	114
Fig. 4.68: Synchronize video and IMU data using the second minimum of E when the person starts to walk with right leg.	116
Fig. 4.69: Synchronize video and IMU data using the first minimum of E when the person starts to walk with left leg.	117
Fig. 4.70: Blinking LED to evaluate proposed method.....	118
Fig. 4.71: LED blink detection.....	119
Fig. 4.72: Synchronize video and IMU data using first LED flag and first LED blink.	

.....	119
Fig. 4.73: Synchronized output for visual inspection paused at 100 th frame.	122
Fig. 4.74: Gait cycle extraction based on shank angle, and the distance travelled measured with Vicon.	125
Fig. 4.75: Model to convert angular velocity to horizontal speed.	126
Fig. 4.76: Estimation of final velocity.....	127
Fig. 4.77: Best fitness value versus generation.	128
Fig. 4.78: Estimated stride lengths.	129

LIST OF TABLES

Table 3.1: Pin Connection for Transceiver nRF24L01+	22
Table 3.2: Pin Connection for Sensor MPU6050	22
Table 3.3: Cost of Electronic Components	22
Table 4.1: Average RMSE and CORR of 3-D Angles Estimated Using Proposed Method	39
Table 4.2: Average RMSE and CORR of Gyroscope Angles (eq. 4.10)	40
Table 4.3: Type of Walking Performed by Each Volunteer	43
Table 4.4: Cost of the Electronic Components used in the Standalone Gait Diagnosis Device	44
Table 4.5: Format of Features	50
Table 4.6: Selection of Dataset to Train and Test Machine Learning Methods	51
Table 4.7: Mean Accuracy of the Machine Learning Methods in Gait Diagnosis	56
Table 4.8: Mean Specificity of the Machine Learning Methods in Gait Diagnosis ..	57
Table 4.9: Mean Sensitivity of the Machine Learning Methods in Gait Diagnosis...	58
Table 4.10: Mean Accuracy of the Perceptron in Design Phase by Randomly Selecting Training and Testing Data.	59
Table 4.11: Memory Requirement: Approximated Number of Integers and Floating Numbers to be Stored on Gait Diagnosis Device.	59
Table 4.12: Mean Accuracy, Specificity and Sensitivity of the Standalone Gait Diagnosis Device.	60
Table 4.13: Mean Sensitivity of the Proposed Method Before and After Training with New Abnormal Walking Pattern.	61
Table 4.14: Feature based comparison among related work.	63
Table 4.15: Possible Gait Sub-Phases	67
Table 4.16: Fuzzy Rules for Gait Phase Detection using Kinetic Parameters	69
Table 4.17: Fuzzy Rules to Detect Heel and Toe on Ground using Kinetic Parameters	69
Table 4.18: Ideal Gait Diagnosis According to Gait Sub-Phases.....	70
Table 4.19: Mean Accuracy (%) of Gait Diagnosis using Proposed Method.	82
Table 4.20: Gait Phase Detection Error (in Sample Difference) when compared with FSRs [9].	84
Table 4.21: Gait Phase Detection Error (ms) when compared with FSRs [9].	84
Table 4.22: Comparison of Gait Phase Detection Methods among Literatures.....	87

Table 4.23: Mean CORR (%) between Original and Reconstructed Angle Waveforms.	100
Table 4.24: Approximate Number of Computations Required per Harmonic.	102
Table 4.25: Gait Phase Detection Error using Reconstructed Waveforms.....	104
Table 4.26: Multi-Class Classification Testing Accuracy.	105
Table 4.27: Synchronization Error of Proposed Method.	120
Table 4.28: Comparison of Video-Inertial Sensor Synchronization Methods among Literatures.	121
Table 4.29: Average Execution Time and Synchronization Error of Proposed Method at Different Frame Rates.....	122
Table 4.30: Comparison among different methods.....	129
Table 4.31: Different types of features used in different methods.	130

LIST OF ABBREVIATIONS

3-D	3-Dimensional
CORR	Correlation Coefficient
DFT	Discrete Fourier Transform
FSR	Force Sensitive Resistor
IC	Initial Contact
IMU	Inertial Measurement Unit
ISw	Initial Swing
LR	Loading Response
MAE	Mean Absolute Error
MAL	Motion Analysis Lab
MPU	Motion Processing Unit
MSt	Mid Stance
MSw	Mid Swing
PC	Personal Computer
PSw	Pre Swing
RMSE	Root Mean Square Error
Rx	Receive
TSt	Terminal Stance
TSw	Terminal Swing
Tx	Transmit

LIST OF PUBLICATIONS

Published journals contributed to this thesis:

Y. C. Han, K. I. Wong and I. Murray, "2-Point Error Estimation Algorithm for 3-D Thigh and Shank Angles Estimation Using IMU," in *IEEE Sensors Journal*, vol. 18, no. 20, pp. 8525-8531, Oct.15, 2018. doi: 10.1109/JSEN.2018.2865764

Y. C. Han, K. I. Wong and I. Murray, "Gait Phase Detection for Normal and Abnormal Gaits Using IMU," in *IEEE Sensors Journal*, vol. 19, no. 9, pp. 3439-3448, May1, 2019. doi: 10.1109/JSEN.2019.2894143

Y. C. Han, K. I. Wong and I. Murray, "Automatic Synchronization of Markerless Video and Wearable Sensors for Walking Assessment," in *IEEE Sensors Journal*, vol. 19, no. 17, pp. 7583-7590, Sept.1, 2019. doi: 10.1109/JSEN.2019.2916163

Y. C. Han, K. I. Wong and I. Murray, "Stride Length Estimation Based on a Single Shank's Gyroscope," in *IEEE Sensors Letters*, vol. 3, no. 10, pp. 1-4, Oct. 2019, Art no. 7001804. doi: 10.1109/LSENS.2019.2942177

Journal submitted for review:

Y. C. Han, K. I. Wong and I. Murray, "Comparison of Machine Learning Methods for the Construction of a Standalone Gait Diagnosis Device".

Y. C. Han, K. I. Wong and I. Murray, "Accurate Gait Modelling based on Waveform Scaling before DFT".

Corrections:

Y. C. Han, K. I. Wong and I. Murray, "Corrections to "Gait Phase Detection for Normal and Abnormal Gaits Using IMU"," in *IEEE Sensors Journal*, vol. 19, no. 19, pp. 8963-8963, Oct.1, 2019. doi: 10.1109/JSEN.2019.2923506

Statements of contribution:

In all journals listed above, Y. C. Han collected and analyzed the data with guidance from K. I. Wong and I. Murray. The journals were written by Y. C. Han with feedback from K. I. Wong and I. Murray.

CHAPTER 1 - INTRODUCTION

1.1 Introduction

According to World Health Organization, about 15% of the world's population has disability, of which about 3% suffer from significant functional problems such as a walking problem [1]. The assessment of walking helps clinicians to determine and provide optimal care and treatments to patients [2]. To perform gait analysis, the fundamental part is the estimation of joint angular displacement, and it involves the detection of joint position and orientation [3]. Currently, the gait evaluation is done based on visual inspection, but this inspection is subjective and depends on the experience of the medical personnel [4]. Although optical motion capture system can be used to make accurate estimation of 3-D orientation angles of human body part, it is non-portable, expensive, complex to set up, and requires an empty space without any optical obstruction [5]. Inertial Measurement Units (IMUs), on the other hand, are portable, affordable, easy-to-setup, and not limited to optical obstruction. This thesis focuses on developing gait analysis methods using IMUs.

This chapter lists the problem statements, objectives, novel approaches, and outline of the thesis.

1.2 Problem Statements

The problems identified and addressed in this thesis are listed as follows:

1. Optical motion capture technology is non-portable, expensive, and complex to setup. IMUs which are portable and easy to setup are favorable. However, commercialized IMUs are still expensive. There is a need to construct IMUs which are affordable.
2. Many researchers have focused on estimating the pitch angle using accelerometer and gyroscope, which consist of unwanted gravitational/motion acceleration component and drift error, respectively. Some researchers managed to estimate the roll angle. However, not many researchers had extended their research to estimate the yaw angle. For those who estimate yaw angle, the utilization of magnetometer is common, but it requires a more complex algorithm to tackle the magnetic interference. There is a need to develop a new 3-D angle estimation algorithm that is accurate and computationally efficient so that the IMUs can be built using low-cost microcontroller.
3. Current gait diagnosis method is done based on visual inspection, which is

subjective and depends on the experience of medical personnel. Therefore, there is a need to develop an electronic device which can evaluate the gait automatically.

4. Most of the existing IMU-based gait phase identification methods consider only normal walking condition. However, the gait sub-phases of people with impaired gaits could occur in different sequences. There is a need to develop a new method for abnormal gait phase detection.
5. Many researchers have worked on expressing human body movement mathematically. At current stage, the reconstructed waveforms either represent smoothed waveforms, fluctuate along the original waveforms, or require high number of computations. There is a need to develop a model that can represent the angle waveforms accurately with less computational requirement.
6. No numerical information is available to the clinicians during visual inspection. It is beneficial to synchronize inertial sensor data with video of a person walking so that joint angle information is available to the clinicians for visual inspection.
7. Most existing IMU-based stride length estimation algorithm depends on the accelerometer data. It is fundamental to investigate if the stride length can be estimated more accurately using the gyroscope data.

1.3 Objectives

The main aim of this research work is to develop gait analysis methods using Inertial Measurement Units (IMUs). Specific objectives are as follows:

1. Formulate efficient and accurate ($\leq 5^\circ$ RMSE) algorithms to estimate the flexion/extension, adduction/abduction and internal/external rotation of the thigh and shank during walking, and validate them against gold standard Vicon optical motion capture system. Then, design and construct an accurate ($\geq 90\%$) and low-cost standalone gait diagnosis device using the estimated 3-D angles.
2. Develop a method to detect normal and abnormal gait phases (≤ 2 sample difference) for gait diagnosis ($\geq 90\%$), and model the human gait pattern mathematically with high reconstruction accuracy ($\geq 99.99\%$) suitable for gait phase detection and diagnosis.
3. Provide joint angle information to the clinicians for visual inspection by synchronizing (≤ 2 frame difference) video and IMU data of a person walking.

1.4 Novel Approaches

A novel method, called ‘2-point error estimation algorithm’, was proposed to estimate the 3-D thigh and shank angles. The drifting direction of the gyroscope was assumed to be linear and the error was eliminated by calibrating the gyroscope data at 2 different timeframes (the 2-point), unlike existing methods updated the angle when certain conditions were fulfilled at 1 point. Validated against gold standard Vicon optical motion capture system, the proposed algorithm resulted a low average root mean square error (RMSE) of 2.9°, 3.6°, and 4.2° for flexion/extension, adduction/abduction, and internal/external rotation angles, respectively. The proposed algorithm is also very computationally efficient as only 2 “atan2()” functions are computed throughout the whole walking motion, and 7 additions and 4 multiplications to estimate each angle.

A new real-time standalone gait diagnosis device was designed and constructed. The device lit on red LED automatically when the user’s gait was abnormal. Green LED illuminated when the user’s gait was normal. The weights and bias of the trained perceptron were successfully transferred to a low-end microcontroller to construct a real-time standalone gait diagnosis device which cost only about US\$8. The mean accuracy of the standalone device was high at 96.5%. The key merits are the feature selection and the construction of the low-cost device.

A novel method to detect normal and abnormal gait phases using an IMU attached to the shank was proposed and validated against an existing method that placed force sensitive resistors (FSRs) under the foot. Some unique waveform patterns of the normal/abnormal shank’s angular velocity and acceleration were identified to detect the gait phases using different local maxima and minima of the angular velocity. The mean absolute error (MAE) of the heel strike, toe strike and toe off detections was low at around 2 sample difference, equivalent to 20ms difference.

A method to mathematically express the thigh and shank angle waveforms was also proposed. The angle waveforms were time and amplitude-scaled before performing discrete Fourier transform (DFT). The proposed method when number of harmonics $H=10$ averagely achieved the same correlation coefficient (CORR) as conventional method when $H = 24, 17, 14,$ and 15 for normal shank, normal thigh, abnormal shank, and abnormal thigh angle waveforms, respectively. This means a reduction of 4 to 14 DFT computations to achieve the same CORR as conventional method. It was also demonstrated that the reconstructed waveform based on proposed

method is able to detect the heel and toe strikes more accurately than conventional method by 1 to 4 sample differences, equivalent to 10ms to 40ms difference. The mean gait multi-class classification accuracy was also improved from below 85% to above 90% using the proposed method.

A method to temporally synchronize IMU data and video of a person walking was proposed so that the joint angle information was available to the clinicians for visual inspection. The synchronization was achieved by detecting and matching the maximum backward swing of the leg detected from video and IMU data. The proposed method was validated by blinking LED and sending LED flag to a computer at the same time. The mean absolute synchronization error of the proposed method was low at ± 1 frames.

Finally, a new stride length estimation algorithm based on a single shank's gyroscope was proposed and validated against gold standard Vicon optical motion capture system. 3 new important features for stride length estimation were identified based on linear kinematics. The new features are the average angular velocity during shank's flexion, the summation of angular velocity during the whole stride, and the duration of the shank's extension. This proposed method had resulted in a low MAE of 4.2cm with a standard deviation of 5.5cm.

1.5 Outline

This thesis is organized into 5 chapters:

1. Chapter 1 (Introduction) lists the problem statements, objectives, and novel approaches.
2. Chapter 2 (Existing Technologies and Literature Review on Gait Analysis) presents the current practices and technology for human gait analysis.
3. Chapter 3 (Experimental Platform) presents the design and construction of IMUs, and the details of some validation tools such as gold standard Vicon optical motion capture system.
4. Chapter 4 (Proposed Methods related to Gait Analysis) discusses the proposed methods, i.e. estimation of 3-D thigh and shank angles, design and construction of a standalone gait diagnosis device, gait phase detection, gait modelling, temporal synchronization of video and IMU data, and stride length estimation.
5. Chapter 5 summarizes the thesis and suggests future research work.

CHAPTER 2 - EXISTING TECHNOLOGIES AND LITERATURE REVIEW ON GAIT ANALYSIS

2.1 Introduction

The human gait cycle is presented in this chapter as the understanding is crucial in developing novel methods for human gait analysis. This chapter also discusses the pros and cons of existing technologies related to gait analysis.

2.2 Human Gait Cycle

Human walking cycle consists of two main phases, i.e. stance and swing phases [6]. The stance and swing phases can be further divided into more detailed 8 sub-phases [6] [7]: Initial Contact (IC), Loading Response (LR), Mid Stance (MSt), Terminal Stance (TSt), Pre Swing (PSw), Initial Swing (ISw), Mid Swing (MSw), and Terminal Swing (TSw), as shown in Fig. 2.1. In [8] [9] [10], the gait cycle is divided into 7 sub-phases, similar to Fig. 2.1 but combining IC and LR. In [11]-[14], the gait cycle is divided into 4 sub-phases: heel strike, stance, push off, and swing as shown in Fig. 2.2.

The primary motion of the leg is flexion/extension, while adduction/abduction and internal/external rotation also occur, but the amplitudes are less consistent among healthy individual due to soft tissue and bony constraints [15]. However, this may not be the case for people with impaired gaits. Therefore, it is needed to estimate the 3-D angles of the leg, instead of just the flexion/extension angle.

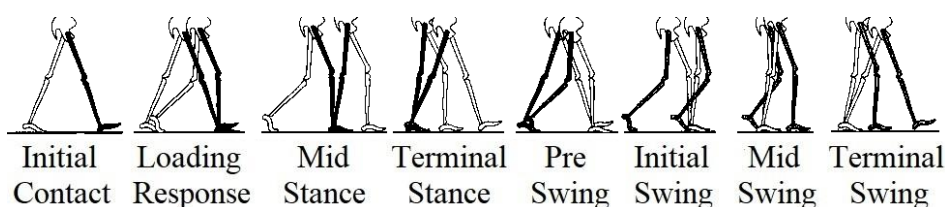


Fig. 2.1: Human gait divided into eight sub-phases [6].

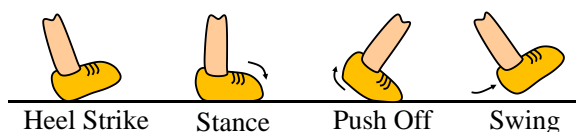


Fig. 2.2: Human gait divided into four sub-phases [11].

IC is the moment when the reference heel strikes onto the ground, and at this moment occurs the contralateral terminal stance. LR begins with initial contact and ends with contralateral toe off (initial swing). During MSt and TSt, the body weights are all supported by the reference leg as the other leg is swinging. MSt ends when the reference heel starts to leave the ground (heel off). TSt ends with contralateral initial contact. PSw ends when the reference toe leaves the ground (toe off). ISw ends with maximum knee flexion. MSw ends when the tibia (shank) is vertical, and TSw ends when the reference heel strikes onto the ground again.

2.3 Existing Motion Capture Technology

2.3.1 Visual Inspection

To perform gait analysis, the fundamental part is the estimation of joint angular displacement, and it involves the detection of joint position and orientation [3]. Currently, the gait evaluation is done based on visual inspection, but this inspection is subjective and depends on the experience of the medical personnel [4].

A common apparatus used by clinicians to measure joint angle is a goniometer [16]. Edwards *et al.* [17] reported that 45% of the visual estimates and 22% of the goniometer measurements had error greater than 5°. Additionally, the goniometer is suitable to measure angle when the patient is not moving, but not suitable when the person is walking.

2.3.2 Force Sensor

Force sensor measures the force exerted by an object. It can be placed under the foot to detect when the foot hits the ground for gait phase detection [12]. [18] used a force platform to evaluate the balance performance of body sway. [19] used force sensors to perform vertical jump analysis, and evaluate the condition of the knee cartilage. A disadvantage of force sensor is that it cannot be used to estimate angles.

2.3.3 Optical Motion Capture System

Optical motion capture system uses video cameras to track human movement. Most high-end optical motion capture systems track the absolute coordinates of reflective markers attached to human body. The measured position of the markers can be used to calculate useful information such as the joint angle, headings, angular velocity, and acceleration. Examples of commercially available optical motion capture

system are Vicon [20], PhaseSpace [21], and OptiTrack [22]. These systems typically consist of 8-16 cameras, and are suitable for full human motion capture.

Optical motion capture system is considered the gold standard in the motion capture field, and is used to validate the performance of other motion capture technology [23] [24]. However, optical motion capture system is expensive, complex to setup, and space-consuming. It is not suitable to perform gait analysis out of the laboratory.

2.3.4 Inertial Sensors

2.3.4.1 Accelerometer

Accelerometer measures linear acceleration [25], and its unit is in m/s^2 ($1g = 9.81m/s^2$). As of today's technology, linear acceleration from gravity g and movement A cannot be measured independently using an accelerometer. In practical, an accelerometer measures the addition of g (a negative value because gravity is pointing downwards) and A together with the offset and white noise n [25], as stated in (2.1).

$$a_j = g_j + A_j + n_j \quad (2.1)$$

Where a denotes the force vector an accelerometer experienced, and j denotes the x , y , and z -axes.

By eliminating the motion acceleration A and offset and noise n , the accelerometer readings are left with gravitational acceleration g as shown in Fig. 2.3. The pitch angle ϕ_{pitch} and roll angle ϕ_{roll} can be calculated using g , as stated in (2.2) and (2.3), respectively.

$$\phi_{pitch} = \text{atan2}(g_z, g_x) \quad (2.2)$$

$$\phi_{roll} = \text{atan2}(g_z, g_y) \quad (2.3)$$

Where g_x , g_y , and g_z are the projection of gravity vector g on x , y , and z -axes respectively.

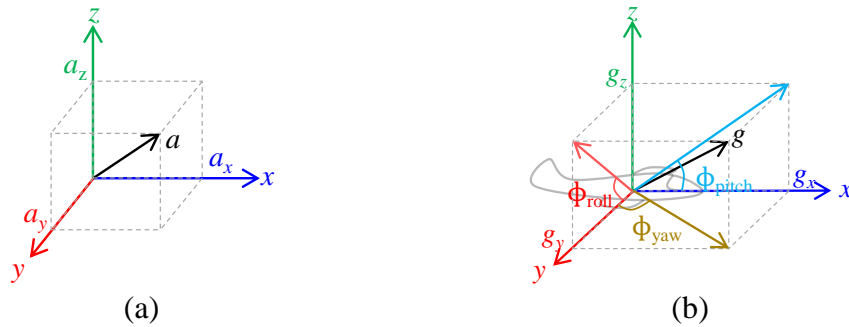


Fig. 2.3: Accelerometer x , y , and z -axes.

(a) Force vector a asserted on an accelerometer. (b) Gravitational acceleration g .

2.3.4.2 Gyroscope

A gyroscope measures angular velocity ω , and its unit is in $^{\circ}/s$ or rad/s . Fig. 2.4 shows the pitch, roll and yaw rotations around the gyroscope axes. Unlike an accelerometer, a gyroscope is unaffected by gravitational acceleration or any linear acceleration [25]. However, the gyroscope readings ω also contains zero-offset bias and noise n (2.4).

$$\omega_j = v_i + n_j \quad (2.4)$$

Where v denotes the angular velocity of the object without bias and noise, and j denotes the x , y , and z -axes.

Gyroscope pitch, roll and yaw angles ψ can be estimated using (2.5) where T denotes the sampling period, and i denotes i^{th} sample. However, (2.5) requires an initial angle to be known to begin the calculations of the remaining angles. This initial angle may be obtained from (2.2) and (2.3), or a pre-known sensor placement such as standing vertically straight. The integration of angular velocity can cause the error n to accumulate resulting the calculated angles to keep drifting away from true values.

$$\psi_i = \psi_{i-1} + \omega_i T \quad (2.5)$$

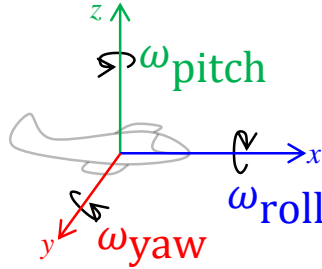


Fig. 2.4: Gyroscope angular velocity ω .

2.3.4.3 Magnetometer

Magnetometer measures magnetic flux density [25], and its unit is in tesla with symbol B . The magnetometer readings B_{measured} can be described as (2.6).

$$B_{\text{measured}} = B + D + n \quad (2.6)$$

Where B denotes the magnetic flux density, D denotes the magnetic disturbance, and n denotes the white noise.

The Earth magnetic field lines vary in strength and direction at different places of Earth according to the magnetic angle of inclination [26]. Ideally, a magnetometer should measure only the Earth magnetic field vector, which is crucial for estimating the yaw orientation angle. However, the presence of ferromagnetic objects or electrical

appliances D in the surroundings can cause the magnetic field vector to vary [27].

2.4 Existing Works in Literature

2.4.1 Angle Estimation using IMU

An IMU is an electronic device that consists of tri-axial accelerometers, tri-axial gyroscopes, and sometimes magnetometers to estimate 3-D angles [28]. One of the main challenges of estimating angles using IMU is that the gyroscope is prone to drift due to noise and surrounding interference such as temperature [29]. Most researchers perform data normalization and filtration to estimate the angles accurately [30]-[34]. Abhayasinghe *et al.* [31] compensated the gyroscope integration drift by updating the flexion/extension angle of the thigh using accelerometer data when the gyroscope read small angular velocity and when the accelerometer magnitude was close to $1g$. This resulted in a high mean CORR of 99.58% between IMU and Vicon system. Tong *et al.* [35] placed force sensors under the foot to detect mid-stance and used this information to remove gyroscope integration drift. When the foot was in contact with the ground, the algorithm automatically reset the estimated flexion/extension angle to 0° . The estimated flexion/extension angle had a mean CORR of 0.97, and a mean RMSE of 4.17° .

Marsico *et al.* [30] tilt various models of smartphones to read the reference values of each axes at $1g$ and offset at $0g$ to normalize the accelerometer data. It was reported that the estimated angles averagely improved up to 65%, but the normalization parameters could not be exported from one sensor to another, though of the same smartphone or sensor model.

Luinge *et al.* [32] designed and evaluated Kalman filter that fused accelerometer and gyroscope data. The authors observed that the forearm inclination estimate from Kalman filter was within 3° RMSE, which was significantly smaller than the errors obtained by accelerometer alone (within 10° RMSE). However, this technique is not possible to estimate yaw orientation accurately. This is because accelerometer reading consists of information about inclination only, but not the yaw. Hence, Global Positioning System (GPS) and magnetometer are usually used to estimate the yaw angle [33].

Madgwick *et al.* [34] used a method called Gradient Descent based Orientation Filter to estimate the 3-D orientation angles of an IMU which consisted of an accelerometer, a gyroscope, and a magnetometer. The proposed method achieved very

low RMSE of pitch, roll, and yaw angles at 0.625° , 0.668° , and 1.110° , respectively.

Roetenberg *et al.* [25] also used an accelerometer, a gyroscope and a magnetometer to estimate the 3-D angles. The authors took magnetic disturbance error into account, and Kalman Filter to minimize the data processing. When the magnetic field was disturbed by an iron object, the estimated angle of the method with magnetic disturbance compensation achieved a low mean error of 1.5° , compared to a big error up to 40° without using the compensation method.

Although a gyroscope can only measure the rate of change of the yaw angle [33], some researchers managed to estimate yaw angles accurately by using a gyroscope only. For example, Wu *et al.* [36] actively changed the orientation of the gyroscope to obtain relations between the gyroscope bias and tilt angle error, so that the gyroscope bias can be estimated and compensated. Using this method, the yaw angle drift, sometimes also known as the heading angle drift, was less than 4° after an hour, while the heading angle drift without using this method was more than 15° after an hour.

Additionally, Bonnet *et al.* [37] used a single gyroscope and a combination of Fourier Linear Combiner (FLC) and weighted FLC to estimate the 3-D orientation angles of the trunk. The authors compared the phase of measured angular velocity with the estimated angular velocity, and then modified the frequency weight to reduce the angle estimation error. The estimated 3-D angles had RMSE less than 1.0° , and CORR of about 0.85.

Some researchers [25] [38] tested their algorithms by rotating the IMU gradually, and achieved low RMSE. This shows that the algorithms are suitable to estimate the inclination of a static or slow-moving object. It is likely to have higher error when the IMU is used for estimating walking motion because there is a significant acceleration due to motion, especially during heel strike and toe-off [39].

Other than being used to estimate the orientation angles, it is worthwhile to note that the IMUs can also be used for indoor positioning. Do *et al.* [40] utilized vertical acceleration to estimate the horizontal displacement and achieved low average error of 1% for straight line paths. Yoon *et al.* [41] fused data from ultra-wideband system and IMUs to track the spatial location and motion.

2.4.2 Gait Diagnosis

Chen *et al.* [42] classified the gait of 2 healthy persons into 2 categories, i.e. holding and not holding a pole while walking, using deep convolutional neural

network based on multistatic radar micro-Doppler signatures. The authors used 20% out of a total of 200 samples to train the neural network and achieved an accuracy of over 99%.

Mikos *et al.* [43] classified freezing of gait, a common walking disorder among Parkinson's disease patients, using neural networks with three extracted features, i.e. freeze index calculated using the amplitude of the frequency components of the acceleration, stride peak, and standard deviation of the angular velocity. The remarkable achievement was the weights of the neural network could be updated to learn patterns that were inadequately trained before. This approach resulted in an overall sensitivity and specificity of 96% and 93%, respectively.

Costilla-Reyes *et al.* [44] classified spatio-temporal gait using raw tomography sensor data without the need to reconstruct tomography images. A total of 892 trials of varying walking speed, backward walking, side walking, right/left foot leading gait and walking with dual task were collected. 50% of the trials were used to train a convolutional neural network to learn the spatio-temporal features, resulting a high accuracy of $97.88 \pm 1.70\%$.

Dolatabadi *et al.* [45] distinguished healthy and pathological gait patterns using two machine learning methods, i.e. k-nearest neighbor and a dynamical generative classifier using Gaussian Process Latent Variable Model (GPLVM). Gait features, including the orientations of the trunk, and lower and upper limbs were collected from 20 healthy people and 20 people with impaired gaits. The gait classification accuracy of k-nearest neighbor was higher at over 94%, compared to GPLVM which achieved accuracy of 68-87%.

Slijepcevic *et al.* [46] classified normal and impaired gaits using support vector machine based on a wide range of spatio-temporal walking parameters collected using force platforms. 161 healthy people and 279 patients with gait disorders were participated in the data collection. The method achieved an accuracy of 91% in classifying the gaits into normal and abnormal categories.

Poschadel *et al.* [47] classified normal and impaired gaits based on sparse coding and dictionary learning. Walking acceleration of the pelvis, thigh, shank, and feet were measured from 23 healthy people and 15 subjects with gait disorders. The authors achieved an accuracy of about 93% in classifying normal and impaired gaits using pre-processed accelerometer data. The classification accuracy dropped to about 70% when raw data was used.

Mazzaro *et al.* [48] worked on activity recognition which includes waking, running, and walking up a staircase based on a model (in)validation viewpoint. Angles of the shoulder, elbow, hip, and knee were collected from 5 people. The authors associated a nominal model to each class of gaits, and then classified an activity by checking whether the angle waveform matched the given model by exploiting interpolation theory. The method achieved an accuracy of 83-86% in recognizing the activities.

2.4.3 Gait Phase Detection

Pappas *et al.* [12] placed 3 FSRs and a gyroscope on the foot to classify the 4 gait phases, i.e. heel strike, stance, heel off, and swing. Senanayake *et al.* [9] used 4 FSRs under the foot to detect IC, LR, MSt, TSt, and PSw. As the foot was in the air during swing phase, there are no forces exerted by the foot. Mukhopadhyay [49] used knee angle to estimate ISw, MSw, and TSw.

Martinez-Hernandez *et al.* [7] collected angular velocity of the thigh, shank and foot from 8 healthy male subjects. The authors classified 8 gait sub-phases based on probabilistic Bayesian formulation with a sequential analysis method, and achieved a mean accuracy of 98%.

Behboodi *et al.* [8] used the angular velocities of both shanks to identify LR, PSw and MSw using zero crossings, MSt and ISw using local maxima, and TSt and TSw using minima.

MacDonald *et al.* [10] used a fuzzy inference system to recognize 7 human gait phases using hip, knee and ankle angles. These joint angles were normalized to small, medium, and large as the input of the fuzzy inference system. The behavior of each joint was examined to determine appropriate rules to detect different gait phases.

Farah *et al.* [11] classified the gait into the 4 main gait phases using decision tree, random forest, multi-layer perceptron, and support vector machine. Features extracted were mean, variance, standard deviation, range, skewness, sum, integral, derivative, energy, power, and bfourth of the knee angle and thigh angular velocity and acceleration. The accuracies of the machine learning methods were greater than 96.4%. MSt was approximated by the mid time between heel strike and push off.

Wang *et al.* [13] detected the 4 main gait phases using an accelerometer strapped onto the lower part of the shank. The stance phase was detected when the accelerometer's vertical axis reading was close to 1g. The heel off, swing, and heel

strike were identified using a dynamic threshold which was calculated using the accelerometer data.

Behboodi *et al.* [8] estimated the MSt, TSt and PSw of the reference leg using the ISw, TSw and LR of the contralateral leg, respectively. The method in [8] is only true if both legs are normal. Maqbool *et al.* [50] only managed to detect the heel strike and toe off using the first and second local minimum of the shank's angular velocity, respectively. Abhayasinghe [51] was not able to identify the stance sub-phase, but stated that it might be approximated by a local maximum of the time derivative of thigh's gyroscope signal. Therefore, there is a research gap in identifying the stance sub-phases, i.e. when the foot flat (more specifically, the toe strike that happens after heel strike) on ground, using gyroscope and accelerometer.

Furthermore, the detection of the end of terminal stance, i.e. heel off, using IMU was not well researched, although [51] stated that it can be detected by the zero crossing of thigh gyroscope signal, but without any validation performed.

2.4.4 Gait Modelling

Mathematical representation of different gait waveforms is useful in many gait applications including activity recognition and medical diagnosis. For example, Ibrahim *et al.* [52] compared the discrete cosine transform coefficients of the hip's accelerometer signals to classify different walking patterns such as walking on flat surfaces, stairs, and ramps. Mostayed *et al.* [53] used the harmonic components of ankle-knee, knee-hip and hip-ankle angle waveforms to diagnose normal/abnormal gaits. Latt *et al.* [54] compared the acceleration patterns of the head and pelvis to detect gait abnormalities in patients with Parkinson's disease.

Gait modelling is also important for rehabilitation and robotics. In [55], a robotic assisted gait rehabilitation system was developed. In [56], normal gait pattern was generated for rehabilitation robots to avoid interaction forces between robot and human in case the patients walked correctly. In [111] and [57], walking pattern was generated for biped walking robots using human model. Other applications of gait modelling include animation [58], user identification [59], and sports [60].

A lot of efforts had been done for gait modelling in recent years. Qiuyang *et al.* [61] and Wark *et al.* [62] represented the thigh angle waveforms and waist accelerometer signals based on Fourier series. Both [61] and [62] used linear predictive model to estimate the key harmonic components of the waveforms. Luu *et al.* [63] used

neural networks to estimate the Fourier coefficient vectors of the lower limb joint angle waveforms. Sekine *et al.* [64] used discrete wavelet transform to approximate the signals of a tri-axial accelerometer attached to lower back. Hughes *et al.* [65] used genetic programming to perform symbolic regression for accelerometer data collected from smartphones placed in pockets.

However, it appears that the reconstructed waveforms based on the existing methods either represent smoothed waveforms [61] [62] [63] [64], or fluctuate along the original waveforms [59] [65]. A problem with smoothed or fluctuating waveforms is that the altered waveforms can provide wrong or suffer loss of gait information. For example, gait sub-phases such as heel and toe strikes, can be identified using the local maxima or minima of the original waveforms [8] [50] [66], but not the smoothed waveforms.

2.4.5 Temporal Synchronization of Video and IMU data

There are several advantages of synchronizing video and inertial sensor data. Chen *et al.* [67] recognized 27 different human motions such as walking and arm-swinging using a Microsoft Kinect camera and an IMU. The accuracy of activity recognition when camera and IMU were fused was about 10% higher than that of using camera or IMU alone. Farnoosh *et al.* [68] fused inertial data and video recorded from a smartphone for indoor navigation. The inertial sensor was used to estimate the smartphone orientation, and the navigation accuracy was improved compared to navigation without orientation estimation. Jatesiktat *et al.* [69] fused a Kinect's depth camera with two IMUs worn on the wrists to improve the accuracy of the upper-body joint tracking. Validated against the gold standard Vicon system, the authors have successfully improved the Kinect's skeleton tracking by 20%.

Bae *et al.* [70] designed a hardware module which connects a gyroscope and a camera for synchronization. In cases where the video cameras and inertial sensors are two separate systems without a synchronization hardware module, the recordings are hard to be initialized at the same time manually. Signal processing needs to be done to synchronize the video cameras and inertial sensors data. Plotz *et al.* [71] synchronized depth cameras connected to a computer and a wireless IMU connected via Bluetooth to the same computer. The transmission time delay between the cameras and the computer was estimated by blinking LEDs controlled by an Arduino board connected to the same computer. Cippitelli *et al.* [72] synchronized camera and accelerometer

data using cross-correlation based time-delay estimation. The horizontal and vertical hand gestures have low average error of 0.5 and 2 frames, respectively. However, circular and wave-like gestures have error more than 10 and 20 frames, respectively. Ryu *et al.* [73] used a position sensitive detector (PSD) camera module to identify the positions of markers attached to a moving object. Each marker consists of a radio frequency transmitter and an infrared LED. The LED blinked and at the same time transmitted a command that consists of the marker's identification number to the PSD to distinguish the identity of each marker. Ofli *et al.* [74] introduced Berkeley Multimodal Human Action Database which consists of temporally synchronized video, audio and accelerometer data of people performing activities such as jumping and sitting. The authors mentioned that the video, audio, and accelerometer data were recorded simultaneously.

Synchronization methods for multiple videos are also reviewed. Lin *et al.* [75] synchronized two videos captured at different angles. The authors first detected the upper body of the subjects, then compared the brightness of the upper body for correlation-matching between the videos. The average synchronization error was within 1 frame. Duong *et al.* [76] synchronized multiple versions of the same movie by matching the audio tracks.

It is proposed to match the maximum backward swing of the reference leg detected from video and inertial sensor for synchronization. There are several possible methods to detect the maximum backward swing of legs from the video. Vicon motion capture system [20] is the gold standard in estimating the joint position and orientation, but this system is expensive and requires multiple cameras. Meribout *et al.* [77] used a parallel hardware architecture to support a parallel Hough transform algorithm to recognize the shape of an object. The method can be extended to detect the shape of any kind of objects including legs, therefore the angle of legs can be estimated. Other edge detection method such as that proposed by Hu *et al.* [78] can also be used to detect the leg. Zhang *et al.* [79] proposed a joint gait-pose manifold-based visual gait generative model to estimate 3-D gait kinematics from a single video camera. Although the method in [79] is accurate enough for some applications, the estimated joint orientations still deviate greatly from the ground-truth at some video frames. On the other hand, existing inertial sensor-based orientation estimation algorithms have achieved higher accuracies [34] [80].

Overall, synchronizing video and inertial sensor data requires signal processing as

the recordings of video and inertial sensor data are hard to be initialized at the same time due to human and software delay. Additionally, the video and inertial sensor may be sampled at different rates.

2.4.6 Stride Length Estimation

Stride length estimation is important for many applications including indoor positioning and health monitoring [81]. Radio Frequency Identification (RFID) [82], WiFi [83], Bluetooth [84] and GPS [85] can be used for stride length estimation. These methods are reliable when the radio signals are stable, but can produce high errors at places where the radio signals are weak due to blockage from solid walls and obstacles. On the other hand, IMUs consisting of gyroscopes, accelerometers and sometimes magnetometer are not influenced by the strength of radio signals. IMUs can provide real-time motion data of the users for gait diagnosis [46], activity recognition [67], stride length estimation [86], and many other applications.

Many existing IMU-based stride length estimation algorithms are based on the data collected from upper body, such as waist, chest, back, and hand. Weinberg [86], Kim *et al.* [87], and Scarlett [88] proposed the relation between stride length and vertical acceleration (2.7)-(2.9).

$$L_{Weinberg} = k_1 \times \sqrt[4]{a_{\max} - a_{\min}} \quad (2.7)$$

$$L_{Kim} = k_2 \times \sqrt[3]{\bar{a}} \quad (2.8)$$

$$L_{Scarlett} = k_3 \times \sqrt{\frac{\bar{a} - a_{\min}}{a_{\max} - a_{\min}}} \quad (2.9)$$

Where L denotes the stride length, k denotes the ratio of the real stride length to the estimated stride length. a denotes the vertical acceleration within a stride. a_{\max} and a_{\min} denote the maximum and minimum value of a , respectively. \bar{a} denotes the average value of a .

In Ladetto [89], stride frequency f was added to the algorithm (2.10), and the stride length estimation accuracy was improved.

$$L_{Ladetto} = w_1 f + w_2 \sigma^2 + b \quad (2.10)$$

Where σ^2 denotes the variance of a . w denotes the weights of the features. b denotes the bias.

Lee *et al.* [90] introduced the total amount of vertical rotation R as a new feature. Each feature was also subtracted by the average value of the training data (2.11).

$$L_{Lee} = w_1(f - \bar{f}) + w_2(\sigma^2 - \bar{\sigma}^2) + w_3(R - \bar{R}) + \bar{L} \quad (2.11)$$

Where $R = \sum_{n=1}^N |\omega_n \times T|$, and ω denotes the vertical angular velocity measured by the gyroscope. $\bar{\sigma}^2$, \bar{R} , \bar{f} , and \bar{L} denote the pre-learned average σ^2 , R , f , and L of all training data, respectively.

There are also existing methods that estimate the stride length based on the IMU data collected from lower body. Diaz *et al.* [91] and Abhayasinghe [51] proposed to estimate stride length based on the opening angles of the thigh (2.12) (2.13).

$$L_{Diaz} = w(\varphi_{\max} - \varphi_{\min}) + b \quad (2.12)$$

$$L_{Abhayasinghe} = w_1 \sin |\varphi_{\max}| + w_2 \sin |\varphi_{\min}| + b \quad (2.13)$$

Where φ_{\max} and φ_{\min} denote the maximum and minimum flexion/extension angles of the thigh within a gait cycle.

Sijobert *et al.* [92] estimated the stride length by integrating the horizontal speed v of the shank (2.14).

$$v(t) = \int_0^{t_s} (\cos \theta(t) a_x(t) - \sin \theta(t) a_y) dt + \cos \theta(0)(-\omega(0)D) \quad (2.14)$$

$$L_{Sijobert} = \int_0^{t_s} (v(t) - \varepsilon(t)) dt$$

Where t_s denotes the duration of the stride. θ is the flexion/extension angle of the shank. x and y denote the vertical and horizontal axes of the IMU, respectively. D is the distance between the IMU and the ankle joint. ε is the error of the estimated v .

Hannink *et al.* [93] used deep convolutional neural networks to estimate the stride length based on the IMU placed on the shoe.

The algorithm proposed by Renaudin *et al.* [94] describes the relationship between height h of subject, stride frequency f , and stride length (2.15), and is not restricted by the IMU placement.

$$L_{Renaudin} = h(w_1 f + b_1) + b_2 \quad (2.15)$$

2.5 Chapter Summary

The primary motion of the leg is flexion/extension. Adduction/abduction and internal/external rotation occur among healthy individuals with less amplitudes due to soft tissue and bony constraints, but this may not be the case for people with impaired gaits. Therefore, it is needed to estimate the 3-D angles of the leg for gait diagnosis, instead of just estimating the flexion/extension angle. Existing gait analysis technologies include force sensors, optical motion capture system, and inertial sensors. Among these technologies, inertial sensors offer great advantages in term of portability and affordability. An efficient and accurate inertial sensor-based angle estimation algorithm is required to be developed. The estimation of 3-D angles is stated in Chapter 4.2.

Some researchers used machine learning methods for gait diagnosis and classifications. Most existing methods are only suitable for post-processing due to complex computations. A real-time standalone gait diagnosis device is needed to be developed. The construction and design of the diagnosis device is described in detail in Chapter 4.3.

For gait phase detection, many researchers used force sensors to detect when the foot hits the ground. Some researchers used IMUs to detect the gait phases of normal gaits. The main research gap is to develop a gait phase detection method for abnormal gaits using IMU. This is considered in detail in Chapter 4.4.

It appears that many research works focused on gait modelling using Fourier series. However, at current stage, the reconstructed waveforms either represent smoothed waveforms or fluctuate along the original waveforms. A problem with smoothed or fluctuating (noisy) waveforms is that the altered waveforms can provide wrong or suffer loss of gait information such as gait phase. An improved gait modelling method is needed to retain the gait phase information from the reconstructed waveforms. This is considered in detail in Chapter 4.5.

Synchronization of video and IMU data requires signal processing as the recordings of video and IMU data are hard to be initialized at the same time due to human and software delay, and the sampling rates may be different. A method to synchronize markerless video and IMU data is needed to be developed. The synchronization method is stated in Chapter 4.6.

IMU-based stride length estimation remains as a challenging problem despite many researchers have tried to use frequency, vertical acceleration, and/or angle to

estimate the stride length. Existing IMU-based stride length estimation algorithms mostly depend on the accelerometer data. It is fundamental to investigate if the stride length can be estimated more accurately using the gyroscope data, and the proposed method is described in Chapter 4.7.

CHAPTER 3 - EXPERIMENTAL PLATFORM

3.1 Introduction

The work presented in this thesis used custom-made IMUs, custom-made IMUs with force sensors, custom-made IMUs with red LED, smartphone camera, and Motion Analysis Lab (MAL) for data collection. The design and construction of the custom-made IMUs are discussed in Chapter 3.2. The force sensitive resistors (FSRs) are added to the IMUs in Chapter 3.3 for validation of the proposed gait phase detection method in Chapter 4.4. A red LED is added to the IMUs for validation of proposed synchronization method in Chapter 4.6. The optical motion capture system used to validate the IMU angles is described in Chapter 3.4.

3.2 Design and Construction of IMUs

3.2.1 Hardware

Fig. 3.1 shows the IMUs constructed for data collection. The model of the inertial sensor used for the IMUs is MPU6050, which consists of a tri-axis accelerometer and a tri-axis gyroscope. The selected sensitivity of the accelerometer is $\pm 2g$, while the sensitivity of the gyroscope is $\pm 250^\circ/s$, both in 16-bit resolution [95]. The sensors are sampled at 100Hz.

The processor used for the IMUs is Arduino Pro Mini 3.3V, which consists of an ATmega328 8-bit microcontroller [96]. The IMU is also equipped with a wireless transceiver nRF24L01+. This transceiver operates in 2.4GHz band, with a data transmission rate of 2Mbps [97].

A rechargeable 3.7V lithium-polymer (Lipo) battery was initially selected as the power supply of the IMUs, but later changed to 2pcs AAA batteries connected in series amounting to nominal 3.0V. This is because it took time to recharge the LiPo battery, and replacing the non-rechargeable batteries seemed to be more convenient.

Fig. 3.2 shows the dongle used to receive wireless data from the IMUs. The dongle consists of transceiver nRF24L01+ and an Arduino Uno R3 connected to a computer through USB.

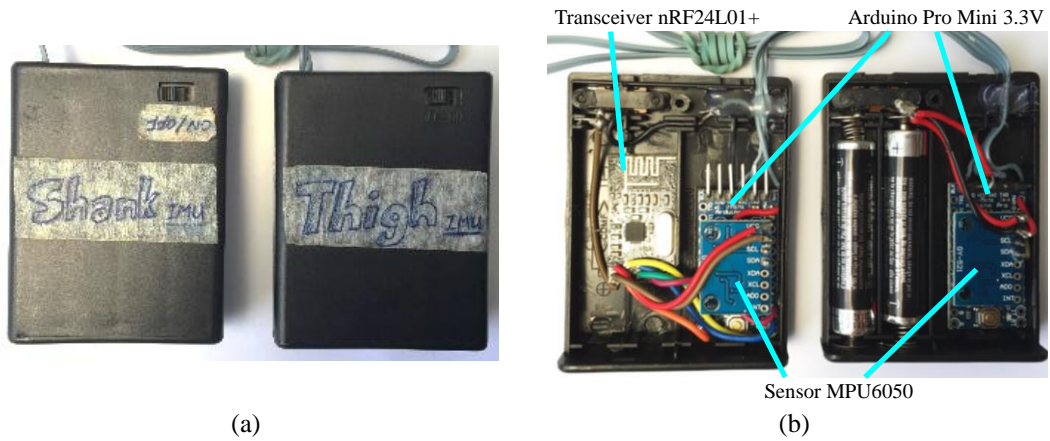


Fig. 3.1: IMUs.
 (a) External view. (b) Internal view.

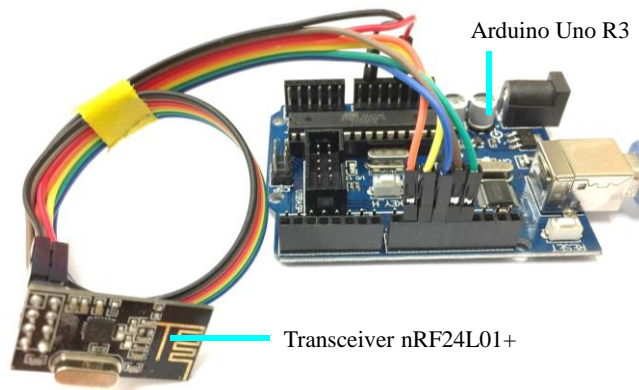


Fig. 3.2: Dongle.

Fig. 3.3 shows that the two microcontrollers of the IMUs are connected together through Rx/Tx lines. Tables 3.1 and 3.2 show the pin connections for transceiver, sensors, and Arduinos.

The electronic components used to construct IMUs and dongle were purchased from www.Taobao.com. The total cost of the electronic components including shipping fees to Malaysia was about 58MYR (\approx US\$14), as listed in Table 3.3.

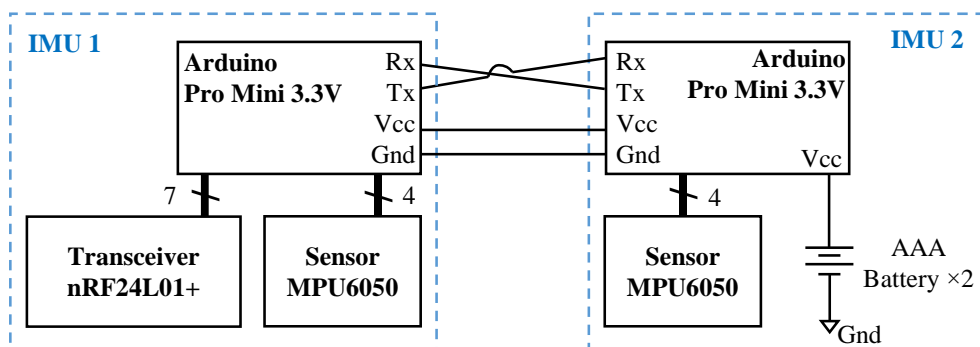


Fig. 3.3: Hardware connections of IMUs.

Table 3.1: Pin Connection for Transceiver nRF24L01+

nRF24L01+ pin	Arduino pin
1 – GND	GND
2 – VCC	VCC 3.3V
3 – CE	9
4 – CSN	10
5 – SCK	13
6 – MOSI	11
7 – MISO	12
8 – interrupt	unused

Table 3.2: Pin Connection for Sensor MPU6050

MPU9150 pin	Arduino pin
VCC	VCC 3.3V
GND	GND
SDA	A4
SCL	A5

Table 3.3: Cost of Electronic Components

	Components	Quantity	Price per Unit (MYR)	Total Cost (MYR)
IMUs	Arduino Pro Mini 3.3V	2	10.73	21.46
	Sensor MPU6050	2	4.35	8.70
	Transceiver nRF24L01+	1	2.99	2.99
	AAA Battery	2	1.50	3.00
Dongle	Arduino Uno R3	1	18.57	18.57
	Transceiver nRF24L01+	1	2.99	2.99
	Total Cost			57.71

3.2.2 Software

The main challenge to tackle for the software development of IMUs is sensor data synchronization. To solve this, the 2 IMUs are connected together through Rx/Tx lines. As shown in Fig. 3.4, the first IMU (named as IMU 1) sends a signal to the second IMU (IMU 2) every 10ms, equivalent to 100Hz. As soon as IMU 2 receives the signal, both IMUs start to read the sensor at the same time (within less than 0.5ms difference). After reading the sensors, IMU 2 sends its raw sensor data to IMU 1, and IMU 1 will compile the raw data from both IMUs according to the format in Fig. 3.5. The data is then transmitted from IMU 1 to the dongle wirelessly. Each transmission consists of 13 sensor data and 1 timer, where each data is 16-bit. In order to reduce data loss, IMU 1 transmits the same compiled sensor data three times. All these are completed in less than 8ms, and the IMUs are ready to repeat the process in the 10thms.

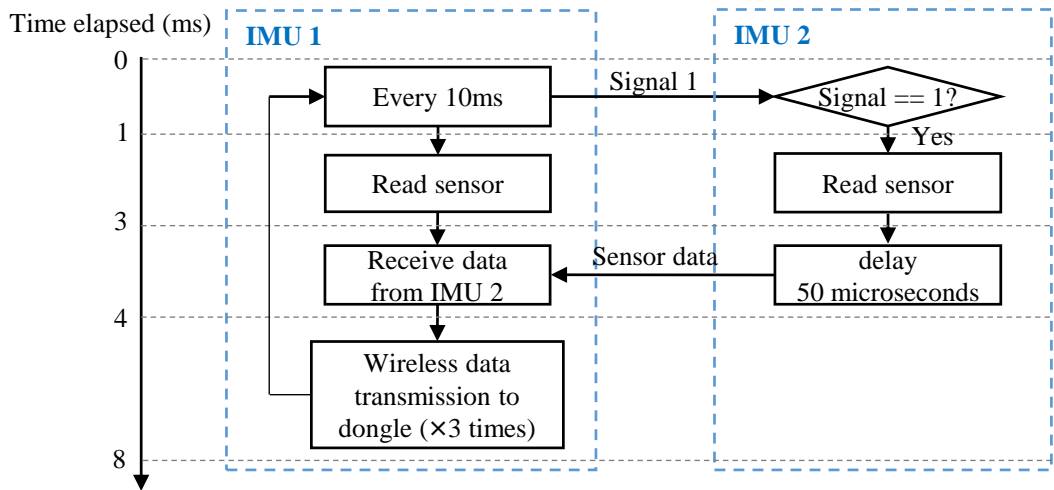


Fig. 3.4: Flowchart for IMU software development.

No.	1	2	3	4	5	6	7	8	9	10	11	12	13
Data	timer	a_x	a_y	a_z	ω_x	ω_y	ω_z	a_x	a_y	a_z	ω_x	ω_y	ω_z
		Data from IMU 1						Data from IMU 2					

a denotes accelerometer data
 ω denotes gyroscope data
 x , y , and z denote sensor axes

Fig. 3.5: Format of compiled sensor data.

As shown in Fig. 3.6, as soon as the dongle receives data from the IMU, the data received is immediately printed at the serial monitor on a computer. The baud rate was set as 115200bps. As the IMU sends the same data three times to reduce data loss, it is possible that the dongle receives multiple repeated IMU data. The dongle will not send repeated data to the computer, and this is achieved by checking the timer value in the received data.

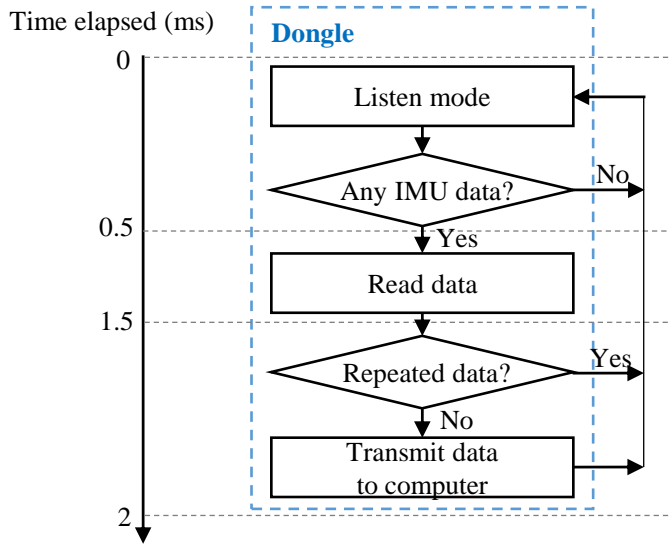


Fig. 3.6: Flowchart for dongle software development.

3.2.3 Data Loss

As IMU data transmission to dongle is wireless, it is needed to identify the optimum separation distance between the IMUs and dongle before the real data collection takes place so that there is minimum data loss in transmission. To do so, the IMU was placed line of sight with the dongle at different distances, and the dongle was set to record 30 seconds of IMU data at each distance. Fig. 3.7 shows the percentage of data loss at varying distances. The data loss was very low ($\ll 1\%$) when the separation distance was within 5 meters. The data loss increased to 2% when the separation distance was 7 meters, most likely due to interference from other nearby devices that operated in the 2.4GHz band. The loss is still considered low ($< 2\%$ loss) even at a separation distance of 19 meters. At a separation distance of 25 meters, the percentage of data loss was high (about 10%). Therefore, it is recommended to use the IMU system within 19 meters. The lost data D_i at i^{th} sample is predicted using (3.1).

$$D_i = \frac{D_{i+N} - D_{i-1}}{N + 1} + D_{i-1} \quad (3.1)$$

Where D_{i-1} and D_{i+N} are the data successfully received by the dongle.

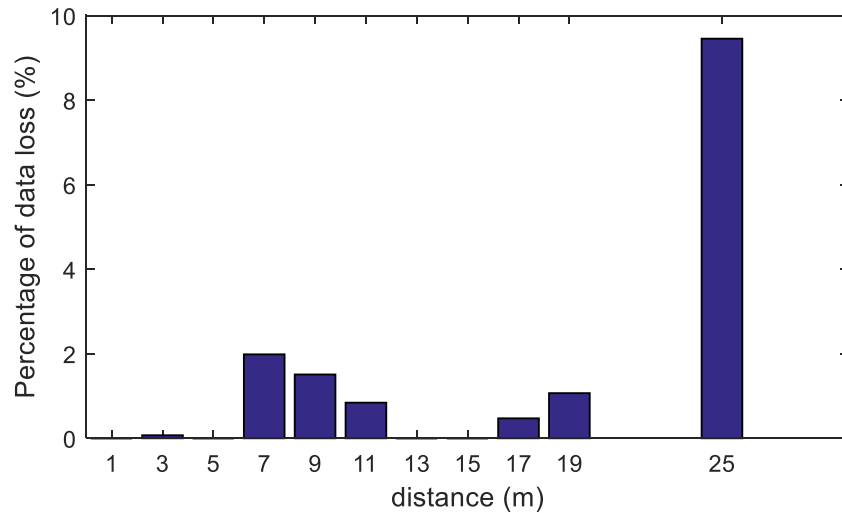


Fig. 3.7: IMU data loss with respect to distance.

3.3 Force Sensors

In Chapter 4.4, the gait phases detected using shank’s IMU are needed to be validated against FSRs. Instead of creating additional device, 4 FSRs are added to IMU 2 as shown in Fig. 3.8. As shown in Fig. 3.9, each FSR is connected in series with a 100kΩ resistor. The forces exerted on the FSRs are measured right after (<2ms) the IMU 2 reads the accelerometer and gyroscope.



Fig. 3.8: IMUs with FSRs.

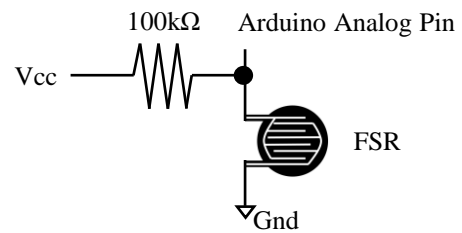


Fig. 3.9: FSR circuitry.

Fig. 3.10 shows the format to compile IMU data and FSR readings before transmitting to dongle. As there are only sixteen 16-bit slots per data transmission using nRF24L01+, the remaining 3 slots (Slots 14, 15, and 16) are used to encode the readings of 4 FSRs. Each FSR reading is 10-bit (maximum value = 1023). The reading of FSR₁ is placed in Slot 14, while the readings of the remaining FSRs are encoded in Slots 15 and 16.

No.	1	2	3	4	5	6	7	8	9	10	11	12	13
Data	timer	a_x	a_y	a_z	ω_x	ω_y	ω_z	a_x	a_y	a_z	ω_x	ω_y	ω_z
		Data from IMU 1						Data from IMU 2					

No.	14	15, 16
Data	FSR ₁	FSR ₂ , FSR ₃ , FSR ₄

Fig. 3.10: Format of compiled sensor data with FSR readings.

3.4 Video Capture and IMUs with LED

In Chapter 4.6, a method to temporally synchronize video and IMU data is proposed. The video camera used in this research is the front camera of an iPhone 6 Plus, which records 720p HD video with a resolution of 1280×720 pixels at a frame rate of 30fps [98].

Inspired from the method in [73] which used blinking LEDs and RF transmitters to synchronize video and markers, a blinking LED and the nRF24L01+ transceiver are utilized to synchronize video and IMU data, for validation of the proposed synchronization method in Chapter 4.6.

As shown in Fig. 3.11, a red LED is connected to the IMUs through wires. The LED blinks for 10ms whenever there is a positive zero crossing of the shank's angular velocity and either one of the previous 10 shank's angular velocities is lower than a threshold $-100^\circ/s$. At the same time of the LED blinks, an LED flag = 1 is encoded in the IMU wireless data transmission to the computer, as shown in Fig. 3.12.

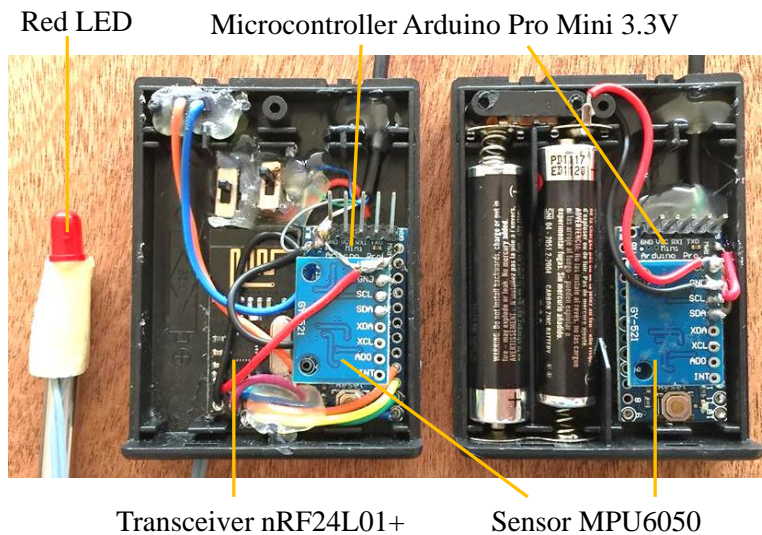


Fig. 3.11: IMUs with LED.

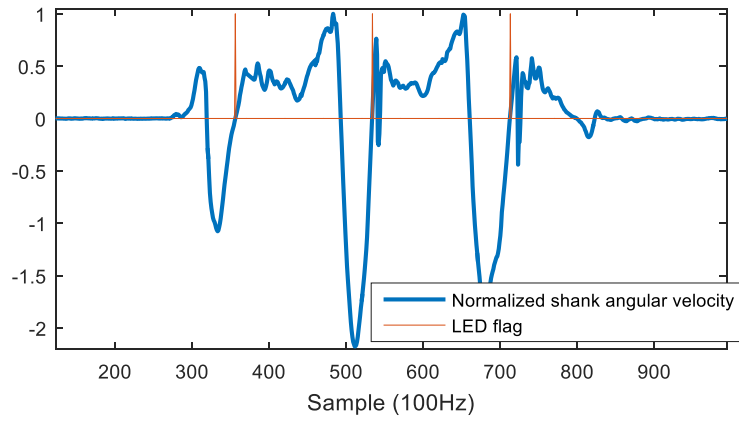


Fig. 3.12: Blinking of LED for validation of proposed method.

3.5 Vicon Optical Motion Capture System

In order to validate the angles estimated using the custom-made IMUs, Vicon optical motion capture system [5] installed in Motion Analysis Lab of School of Physiotherapy and Exercise Science of Curtin Australia was used. The Vicon system consists of 18 cameras to track the 3-D coordinates of reflective markers as shown in Fig. 3.13. The sampling rate was set at 300Hz. The software used was Vicon Nexus 1.8.5 motion processing software.

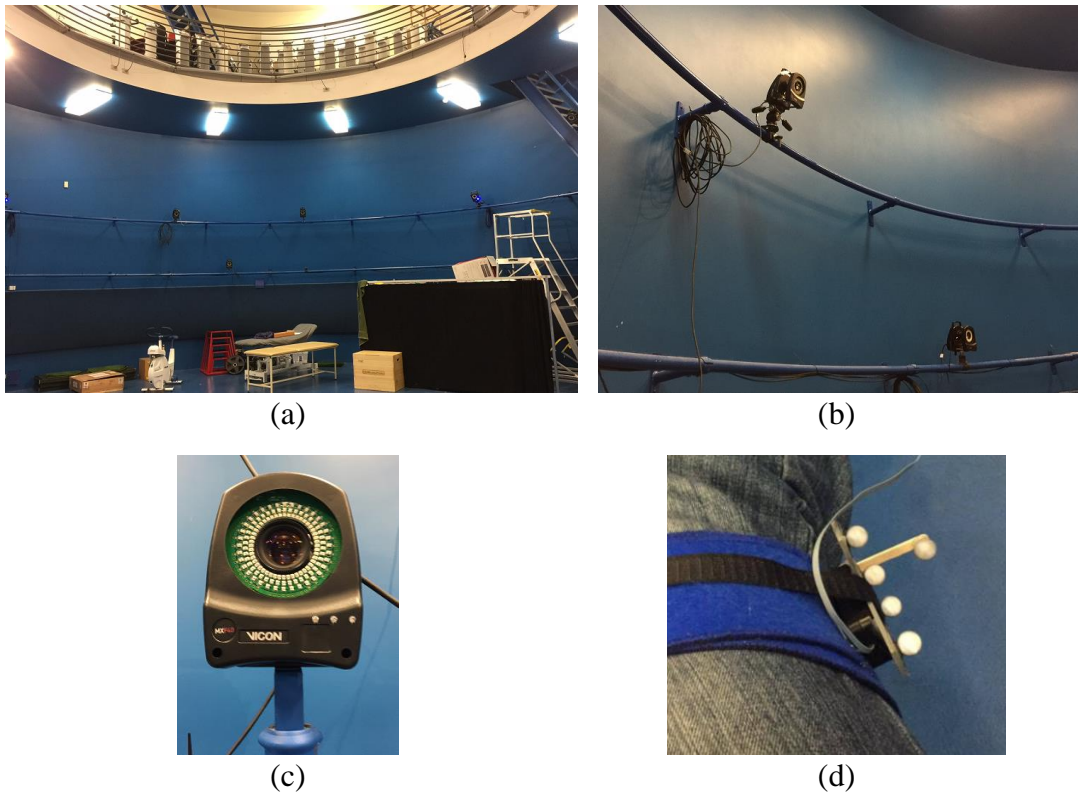


Fig. 3.13: Vicon Optical Motion Capture System.
 (a) MAL. (b) Cameras surround MAL. (c) Camera. (d) Markers.

3.5 Chapter Summary

In this chapter, the hardware and software components of the custom-made IMUs were described. The wireless data transmission loss of the IMUs was low when the distance between IMUs and dongle was within 19 meters, therefore the IMU data collection should take place within ± 19 meters. For validation of proposed methods, the IMUs were added with FSRs and a red LED. A smartphone camera and the Vicon system used in this research were also described.

CHAPTER 4 - PROPOSED METHODS RELATED TO GAIT ANALYSIS

4.1 Introduction

The main contributions of the thesis are presented in this chapter. The proposed methods are presented in details, followed by results and discussions in each sub chapters. The proposed methods included in this chapter are listed as follows:

- Estimation of 3-D Thigh and Shank Angles using IMU
- Design and Construction of a Standalone Gait Diagnosis Device
- Gait Phase Detection for Normal and Abnormal Gaits
- Accurate Gait Modelling based on Waveform Scaling before DFT
- Temporal Synchronization of Markerless Video and IMU data
- Stride Length Estimation using a Single Shank's Gyroscope

4.2 Estimation of 3-D Thigh and Shank Angles using IMU

4.2.1 Introduction

In this chapter, a new 3-D thigh and shank angles estimation algorithm, called 2-Point Error Estimation algorithm, is proposed. The gold standard Vicon optical motion capture system in Curtin Australia's Motion Analysis Lab is used to validate the proposed method.

Chapter 4.2 is covered by the following publication with minor amendment:

Y. C. Han, K. I. Wong and I. Murray, "2-Point Error Estimation Algorithm for 3-D Thigh and Shank Angles Estimation Using IMU," in *IEEE Sensors Journal*, vol. 18, no. 20, pp. 8525-8531, Oct.15, 2018.

doi: 10.1109/JSEN.2018.2865764

© 2018 IEEE

4.2.2 Experimental Setup

Fig. 4.1 shows that the IMUs, consisting of a tri-axial accelerometer and a tri-axial gyroscope, were strapped at the outer side of the thigh and shank using Velcro straps. The details of the IMUs are described in Chapter 3.2.1. The sampling rate of the IMUs was 100Hz.

The 3-D angles estimated using IMUs were to be validated against the gold standard Vicon optical motion capture system. The Vicon system is described in Chapter 3.5. The sampling rate of the Vicon system was set at 300Hz. The markers of the Vicon system were placed on the IMUs. The 3-D movement of the thigh and shank were tracked simultaneously using IMUs and the Vicon system.

The subjects were requested to stand still for 3 to 5 seconds, then walk straight on a flat surface for 3 to 5 steps, and finally stood still for another 3-5 seconds. Although more steps were always preferred per trial, 3 to 5 walking steps would be sufficient to capture the walking pattern of an individual for gait analysis as walking is a repetitive motion. Additionally, since the focus of this research is for walking assessment, a patient may not be able to walk for a long distance. For the first 3 trials, each volunteer walked straight normally. For another 3 trials, the volunteers were requested to walk straight but intentionally move their legs outwards in each walking cycle to simulate abnormal walking. A total of 60 walking trials were collected from 10 healthy adults (male: 8; female: 2; age: 22-35; height: 160-177cm; weight: 55-94kg).

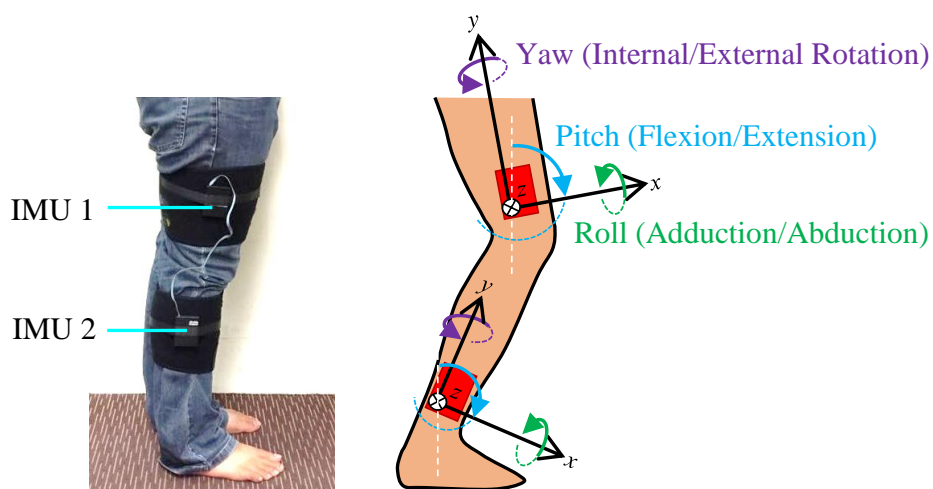


Fig. 4.1: Placement of IMUs.

4.2.3 Proposed Method

4.2.3.1 Overall flowchart

Fig. 4.2 and 4.3 show the overall flowchart to estimate 3-D angles. The proposed method consists of 3 main steps, i.e. identifying the starting and stopping time of walking, followed by estimating the accelerometer and gyroscope angles, and finally the proposed 2-Point Error Estimation algorithm.

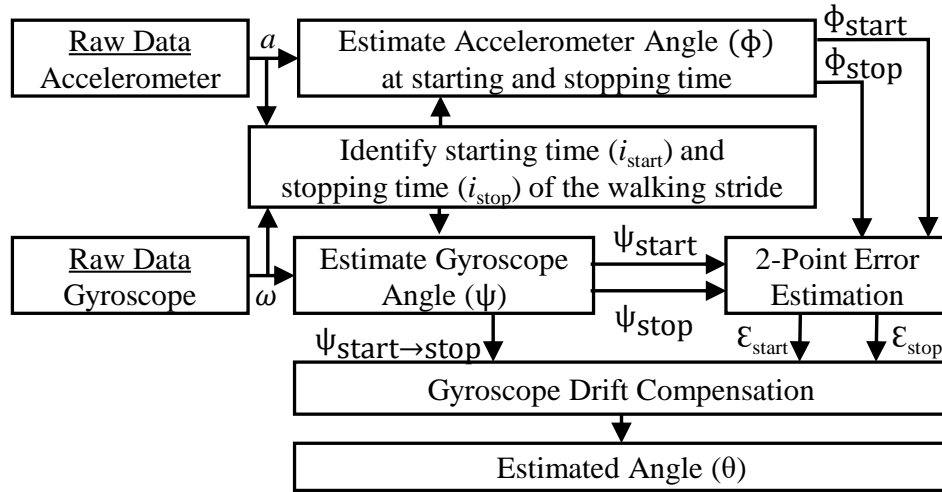


Fig. 4.2: Flowchart to estimate flexion/extension and adduction/abduction angles.

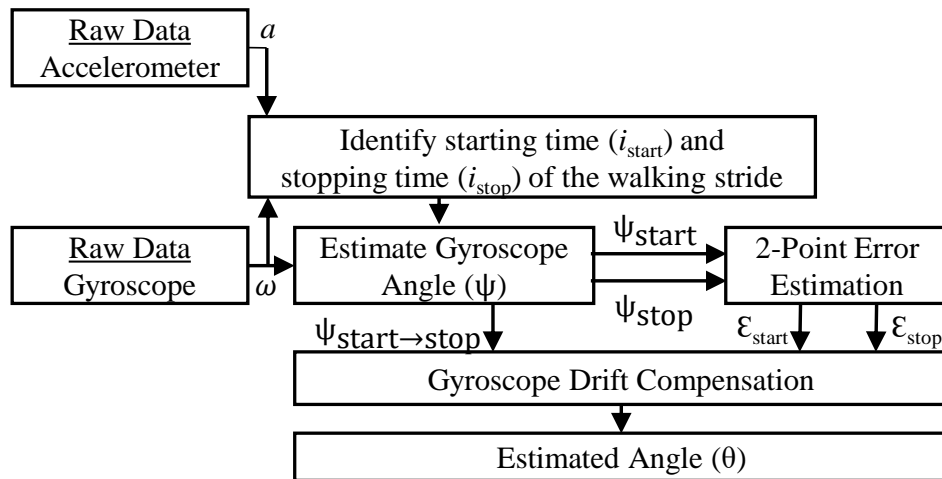


Fig. 4.3: Flowchart to estimate internal/external rotation angle.

4.2.3.2 Starting and Stopping Time of Walking

The 2-Point Error Estimation algorithm developed requires the starting and stopping time of walking to be known. The starting and stopping time can be recorded manually using a timer before and after each walking movement. However, manual time recording is tedious and prone to human error. For a more accurate identification of the starting and stopping time of a walking trial, it is necessary to create an algorithm to do so automatically.

To utilize accelerometer and gyroscope to identify the starting and stopping time of walking, it is necessary to know the parameters that are measured by these two inertial sensors. The measured accelerometer data a can be modelled as (4.1) where g denotes the gravitational acceleration, A denotes the linear acceleration due to movement, n_a denotes the accelerometer DC offset plus noise. The measured gyroscope data ω is modelled as (4.2) where v denotes the angular velocity, n_ω denotes the gyroscope DC offset plus noise.

$$a = g + A + n_a \quad (4.1)$$

$$\omega = v + n_\omega \quad (4.2)$$

When the person is standing still, the linear motion A is minimized, and hence accelerometer measures $a \approx g + n_a$. On the other hand, when the person is standing still, gyroscope will ideally measure zero angular velocity v , and hence $\omega \approx n_w$. Assuming the DC offset and noise n of the accelerometer and gyroscope are negligible, the measured values are now $a \approx g$ and $\omega \approx 0$.

As the Earth's gravitational acceleration is 1g pointing vertically downwards, the vertical axis of the accelerometer would ideally measure 1g, while the other two horizontal axes would ideally measure 0g when the person is standing still. Therefore, $|a| = (a_x^2 + a_y^2 + a_z^2)^{0.5} \approx 1g$, where x , y , and z are the axes of the sensor. For the gyroscope, all three axes would ideally measure 0°/s when the person is standing still. Therefore, by fulfilling (4.3) and (4.4), the period of which the person is standing still can be identified, where thresholds λ_1 and λ_2 are approaching 0. In this research, λ_1 and λ_2 were set as 0.07g and 10°/s respectively due to the offset and noise of the sensors. The threshold values were obtained through trials and errors.

$$1 - (a_x^2 + a_y^2 + a_z^2)^{0.5} < \lambda_1 \quad (4.3)$$

$$|\omega_j| < \lambda_2 \quad \text{for } j = x, y, z \quad (4.4)$$

Fig. 4.4 shows the flowchart to identify the starting and stopping time of walking. The algorithm checks (4.3) and (4.4) from the middle of the dataset which is when the

person is walking, and progress towards the start or end of walking. When (4.3) and (4.4) are first fulfilled for a continuous number of λ_3 time, the starting or stopping time can be identified. The threshold λ_3 is set to be 50 in this research.

It must be noted that the ideas of (4.3) and (4.4) are inspired from [51], but the researcher in [51] used these equations to decide whether to use accelerometer or gyroscope data to estimate the flexion/extension angle, while the application of these two equations in this proposed method is to identify the starting and stopping time of walking.

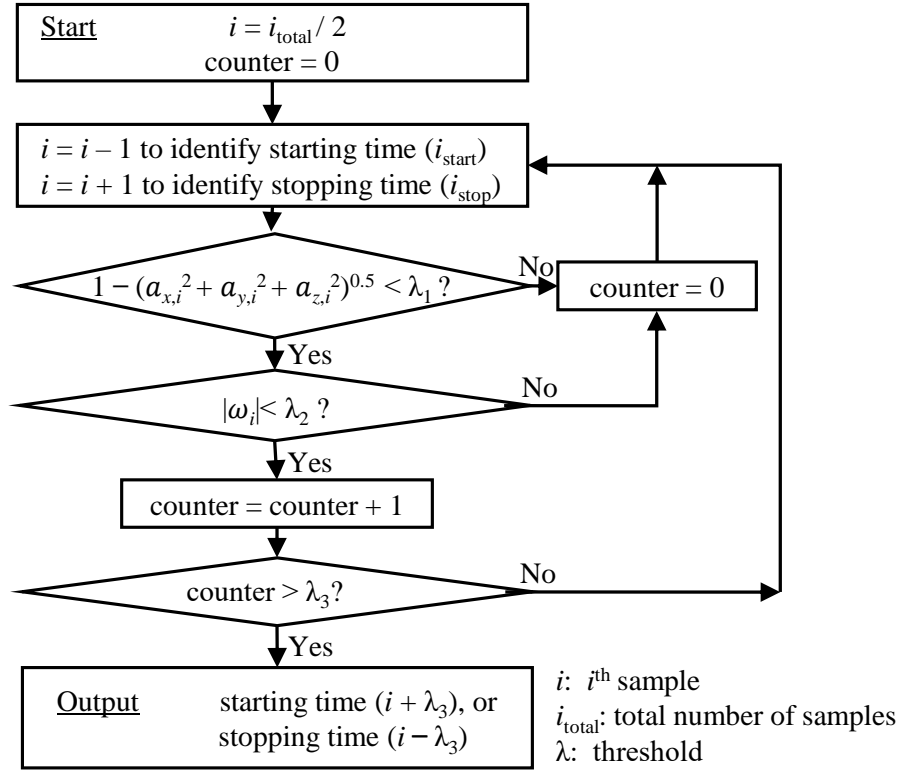


Fig. 4.4: Flowchart to identify the starting or stopping time of walking.

4.2.3.3 Estimation of Accelerometer and Gyroscope Angles

In this research, the accelerometer data a is lowpass filtered using a simple moving average in (4.5), where \bar{a} denotes the filtered accelerometer data. The value of k used in this research is 30.

$$\bar{a}_i = \frac{1}{2k} \sum_{i=i-k}^{i+k} a_i \quad \text{for } \begin{matrix} i < i_{\text{start}} \\ i > i_{\text{stop}} \end{matrix} \quad (4.5)$$

Accelerometer can estimate the pitch angle ϕ_{pitch} and roll angle ϕ_{roll} according to (4.6) and (4.7), respectively. However, accelerometer cannot be used to estimate yaw

angle ϕ_{yaw} because gravitational acceleration is a vertical reference, but the estimation of the yaw angle requires a horizontal reference.

$$\phi_{\text{pitch}} = \text{atan2}(\bar{a}_x, \bar{a}_y) \quad (4.6)$$

$$\phi_{\text{roll}} = \text{atan2}(\bar{a}_z, \bar{a}_y) \quad (4.7)$$

The initial gyroscope pitch angle ψ_{pitch} and roll angle ψ_{roll} are set as the accelerometer angles as stated in (4.8), respectively. The initial yaw angle is set as 0° as stated in (4.9) because the person is facing straight initially. The gyroscope 3-D angles can then be estimated using (4.10) which is the integration of measured angular velocity ω , where $T=0.01\text{s}$ is the sampling time.

$$\psi_1 = \phi_1 \quad \text{for } \psi_{\text{pitch}} \text{ and } \psi_{\text{roll}} \quad (4.8)$$

$$\psi_1 = 0 \quad \text{for } \psi_{\text{yaw}} \quad (4.9)$$

$$\psi_i = \psi_{i-1} + \omega_i T \quad \text{for } i = 2, 3, 4, \dots \quad (4.10)$$

4.2.3.4 2-Point Error Estimation Algorithm

To compensate the gyroscope integration drift, a 2-Point Error Estimation algorithm is proposed. The error of the estimated gyroscope angle is first estimated at starting time i_{start} and stopping time i_{stop} of walking. The error at these two points are called the 2-point error. To estimate the 2-point error, the gyroscope angle is compared with the accelerometer angle using (4.11) by calculating their difference \mathcal{E} .

$$\mathcal{E}_i = \psi_i - \phi_i \quad \text{for } \begin{matrix} i = i_{\text{start}}, i_{\text{stop}} \\ \text{pitch and roll angles} \end{matrix} \quad (4.11)$$

As mentioned, the initial yaw angle at i_{start} is assumed to be 0° because accelerometer cannot estimate the yaw angle. Since the heading before and after a person walks straight should ideally remain the same, the final yaw angle at i_{stop} is also assumed to be 0° . The 2-point error of the gyroscope yaw angle can then be estimated using (4.12) by subtracting the estimated gyroscope yaw angle with 0° .

$$\mathcal{E}_i = \psi_i - 0 = \psi_i \quad \text{for } \begin{matrix} i = i_{\text{start}}, i_{\text{stop}} \\ \text{yaw angle} \end{matrix} \quad (4.12)$$

The 2-point error calculated in (4.11) and (4.12) are then used to estimate the error of the gyroscope angles during walking motion, i.e. from i_{start} to i_{stop} . The error of the gyroscope angle from i_{start} to i_{stop} is estimated by linearly distributing the 2-point error (4.13) using a linearly distributed weight W calculated in (4.14). The final estimated 3-D angles θ can be calculated using (4.15) by removing the estimated error from the estimated gyroscope angle.

$$\varepsilon_i = \varepsilon_{\text{start}}(1 - W_i) + \varepsilon_{\text{stop}}W_i \quad (4.13)$$

$$W_i = \frac{i - i_{\text{start}}}{i_{\text{stop}} - i_{\text{start}}} \quad (4.14)$$

$$\theta_i = \psi_i - \varepsilon_i \quad (4.15)$$

for $i = i_{\text{start}}, i_{\text{start}}+1, i_{\text{start}}+2, \dots, i_{\text{stop}}$
pitch, roll, yaw angles

The pitch and roll angles when the person is standing still, i.e. before starting time i_{start} and after stopping time i_{stop} , can be estimated using (4.6) and (4.7), respectively.

4.2.4 Results and Discussion

Fig. 4.5 and 4.6 show the 3-D orientation angles of the thigh and shank of the same individual. The blue lines are the angle waveforms estimated using gold standard Vicon optical motion capture system. The red lines are the angle waveforms estimated using the proposed 2-Point Error Estimation algorithm. The yellow lines are the angle waveforms estimated using (4.10) which is prone to gyroscope integration drift.

Fig. 4.7 shows the error of the estimated 3-D angles in Fig. 4.5. The errors of the gyroscope angles before and after walking were mostly linear. However, the error of the gyroscope angles (pink lines) was fluctuating while the person was walking. Drawing a straight line (dotted green line) connecting the gyroscope angles at starting time i_{start} and stopping time i_{stop} , it was assumed in this research that the drifting direction of the gyroscope angles was linear.

Referring to the thigh flex/ext. in Fig. 4.7, the gyroscope drifting direction (dotted green line) was almost linear at all time. However, there are cases, for example the thigh add/abd. in the same figure, that the estimated drifting direction of the gyroscope angles were different before, during, and after walking. Therefore, a 2-point gyroscope error estimation, i.e. estimating the error based on pre- and post-calibration method, was proposed, while many researchers estimated the sensor error based on pre-calibration method only [8].

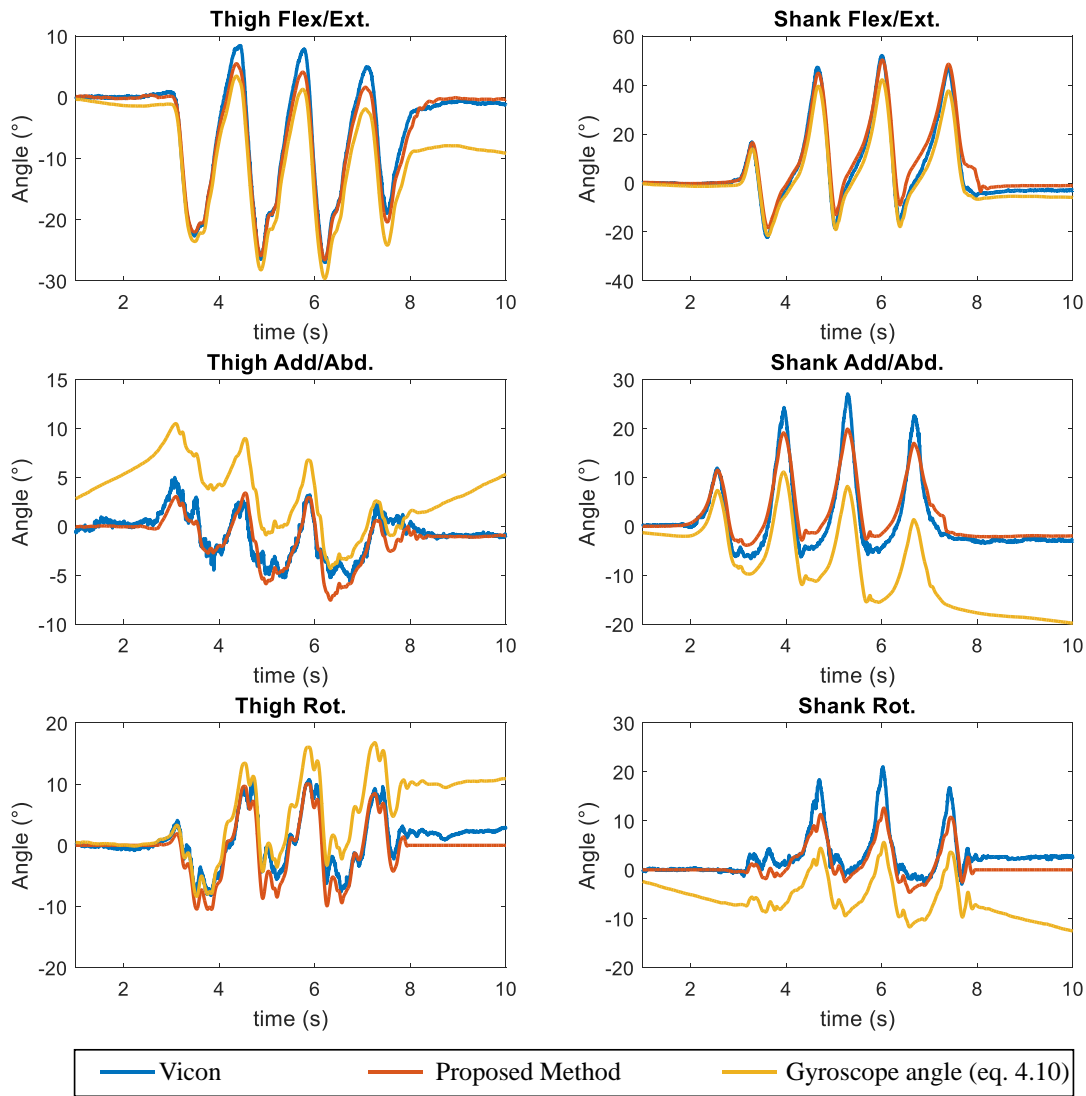


Fig. 4.5: Estimated 3-D angles of the thigh and shank during normal walking on a flat surface.

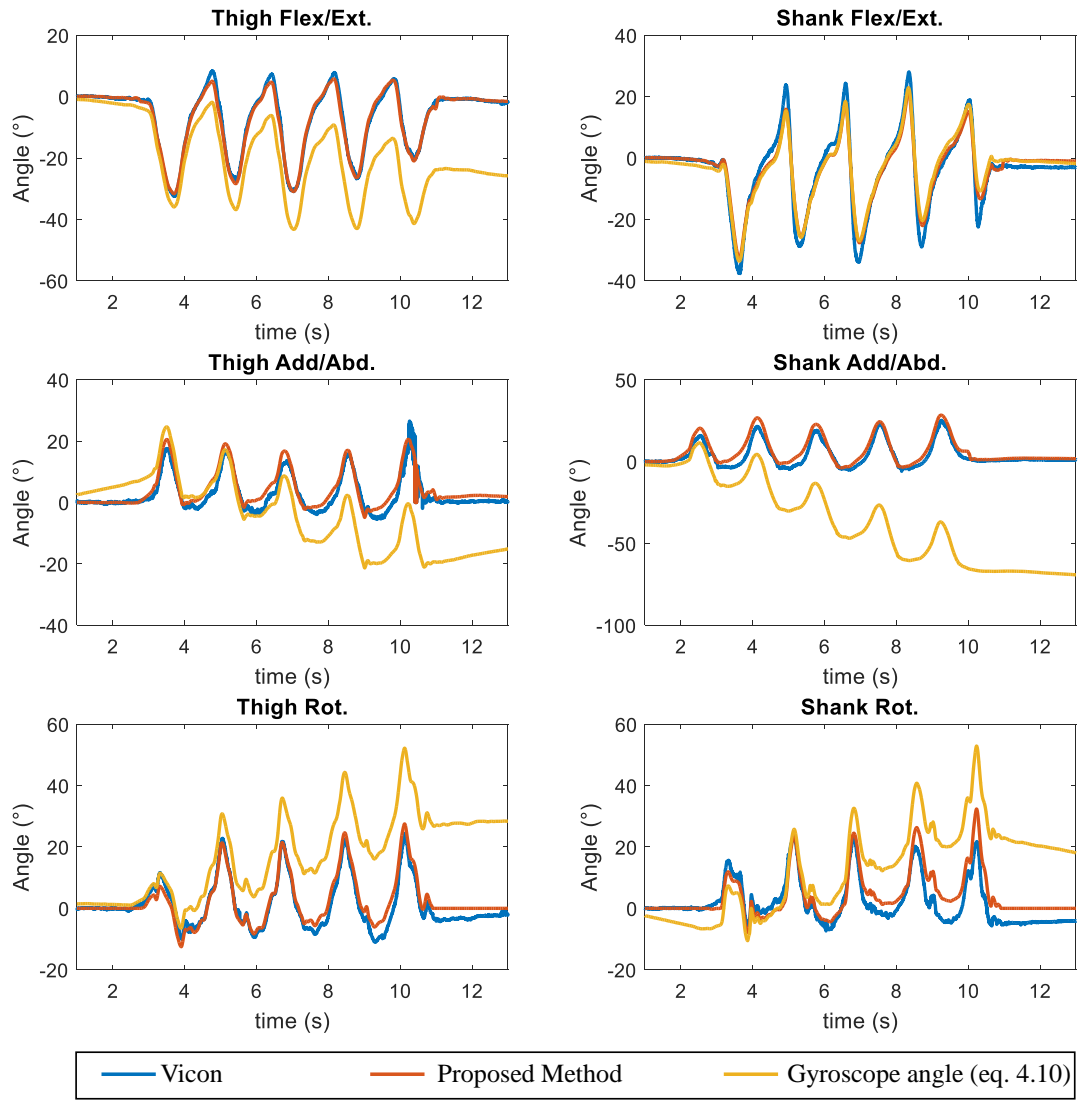


Fig. 4.6: Estimated 3-D angles of the thigh and shank during abnormal walking on a flat surface.

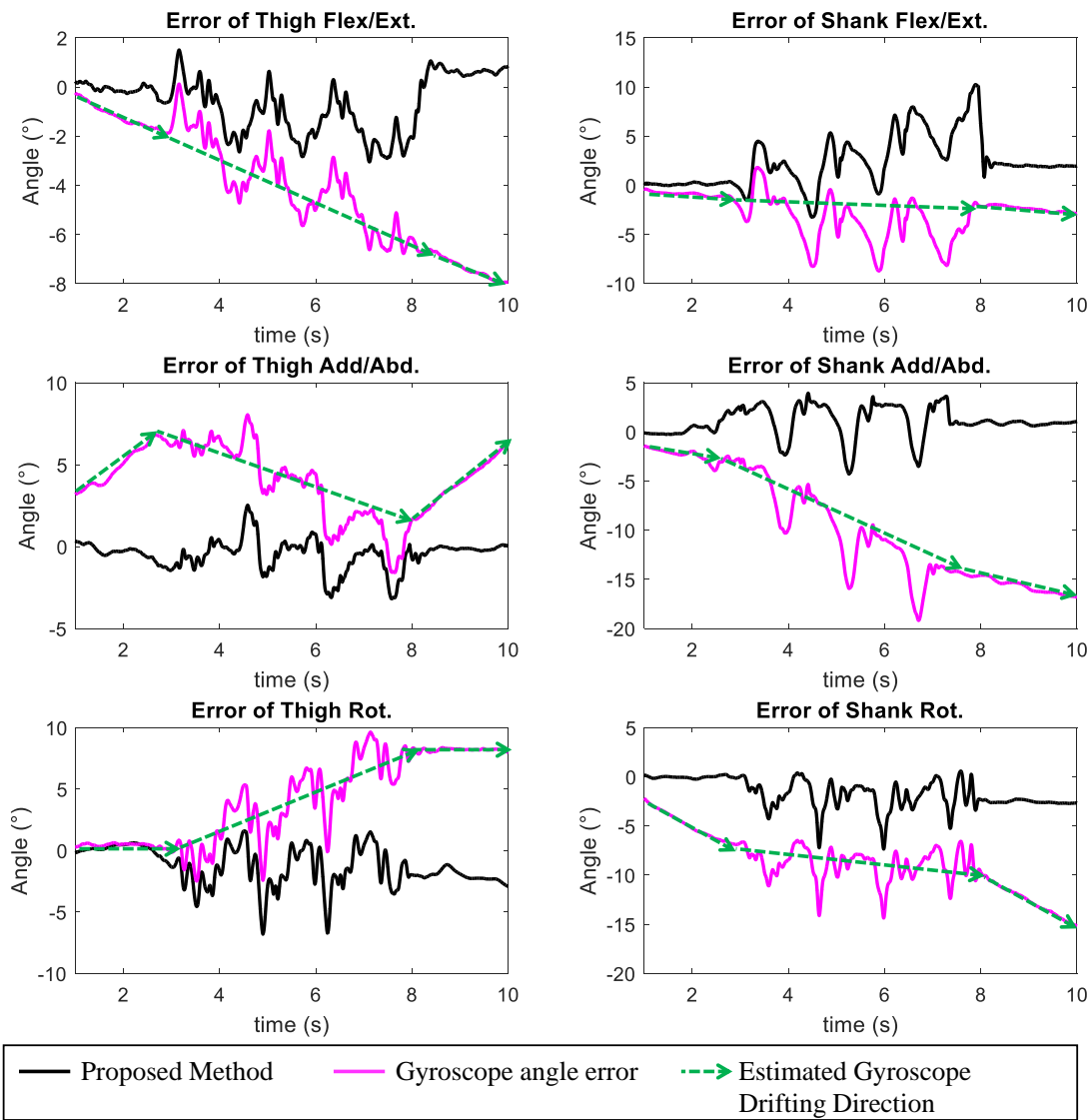


Fig. 4.7: Error of the estimated thigh and shank angles during normal walking on a flat surface.

The RMSE and CORR in Tables 4.1 and 4.2 were calculated for the walking period, i.e. from starting time i_{start} to stopping time i_{stop} . This better describes the accuracy of the method compared to considering the standing period which had very little movement. The results improved when the standing still period was considered.

Referring to Table 4.1, the proposed 2-point Error Estimation algorithm resulted an averagely low RMSE of less than 5° for all 3-D angles of the thigh and shank, in normal and abnormal walking conditions. Comparing with the angles estimated by directly integrating the gyroscope data (4.10), the proposed 2-point error estimation algorithm is proven effective in compensating the gyroscope drift. The RMSE of the angles estimated by directly integrating gyroscope data was high at $7-36^\circ$ as shown in Table 4.2.

The flexion/extension angle estimated using the proposed algorithm achieved high CORR of 98.8% for thigh, and 97.7% for shank. The adduction/abduction and internal/external rotation angles estimated using proposed algorithm achieved lower CORR of 83-93% compared to the flexion/extension angle. However, comparing Tables 4.1 and 4.2, the proposed algorithm improved the adduction/abduction and internal/external rotation angles from 43-77% to 83-93%, i.e. an improvement of 16-40%.

Table 4.1: Average RMSE and CORR of 3-D Angles Estimated Using Proposed Method

	Walking on flat surface	Flexion/Extension		Adduction/Abduction		Internal/External Rotation	
		Thigh	Shank	Thigh	Shank	Thigh	Shank
RMSE ($^\circ$)	Normal	1.934	3.685	2.017	4.701	3.604	4.039
	Abnormal	2.270	3.589	2.729	4.952	4.184	4.920
	Overall	2.102	3.637	2.373	4.826	3.894	4.479
CORR (%)	Normal	98.90	96.70	92.40	79.50	81.60	87.20
	Abnormal	98.60	98.60	93.20	85.40	90.70	90.10
	Overall	98.80	97.70	92.80	82.50	86.20	88.60

Table 4.2: Average RMSE and CORR of Gyroscope Angles (eq. 4.10)

	Walking on flat surface	Flexion/Extension		Adduction/Abduction		Internal/External Rotation	
		Thigh	Shank	Thigh	Shank	Thigh	Shank
RMSE (°)	Normal	7.93	6.69	11.12	23.43	7.88	14.45
	Abnormal	14.46	10.55	13.02	36.09	16.13	18.53
	Overall	11.20	8.62	12.07	29.76	12.00	16.49
CORR (%)	Normal	94.20	97.90	81.20	45.20	72.80	82.10
	Abnormal	87.70	94.90	71.90	40.40	63.50	62.90
	Overall	90.90	96.40	76.50	42.80	68.20	72.50

An advantage of the proposed method is that the filtration of raw gyroscope data is not required. This reduces smoothing or alteration of the angle waveform patterns. The waveform patterns of the estimated 3-D angles are relatively similar to that of Vicon system, as shown in Fig. 4.5 and 4.6.

This proposed algorithm is also computationally efficient as only two “atan2()” functions were computed in (4.6) and (4.7) throughout the whole walking motion, and 7 additions and 4 multiplications for each angle estimated using (4.10) to (4.15).

A disadvantage of the proposed algorithm is that it is only suitable to estimate the 3-D angles for a short duration of time. However, as walking cycle is expected to be repetitive with slight differences [6], 3 to 5 walking steps is sufficient to evaluate the gait pattern of a person. Based on the experimental results, the proposed algorithm can at least estimate the 3-D angles accurately up to 15 seconds, which is sufficient to capture 5 walking steps of a person.

Moreover, this proposed method is unable to estimate angles in real time, but real-time angle estimation is not necessary for applications such as gait evaluation.

Furthermore, many researchers utilize magnetometer to estimate yaw angle [25] [34] [99]. Although a magnetometer can be added to improve the accuracy of internal/external rotation angle, the proposed 2-point error estimation algorithm does not require a magnetometer. As magnetometer is prone to magnetic interference [100], avoiding it has drastically improved the computational efficiency. However, the assumption that the yaw angle remains before and after walking is only true for walking in a straight line. This assumption has resulted a considerably accurate

estimation of the yaw angle with low average RMSE of 3.9° for thigh and 4.5° for shank.

The proposed algorithm requires the users to stand still before and after walking. As this system is designed for clinical application, it is possible that some patients with impaired gaits would have involuntarily shaky legs [101]. This creates a problem that there is no standing still period for the algorithm to estimate the 2-point error. To solve this, the thresholds in (4.3) and (4.4) can be increased to values slightly higher than the average values of accelerometer and gyroscope data collected in the first second, respectively. The increased thresholds would treat the shaky legs as standing still, and then the walking motion could be identified when the thigh flexes/extends above these thresholds.

4.2.5 Summary

A method to estimate the 3-D angles of the thigh and shank was proposed. The proposed algorithm was not only accurate, but also computationally efficient. Validated against the Vicon optical motion capture system, the proposed algorithm resulted in low average RMSE of 2.9° , 3.6° , and 4.2° for flexion/extension, adduction/abduction, and internal/external rotation angles of the thigh and shank, respectively. The angle waveform pattern is very similar to that of Vicon as the gyroscope data was not needed to be filtered. In term of computational efficiency, only two “atan2()” functions were needed to be computed throughout the whole walking motion, and 7 additions and 4 multiplications for estimating each angle.

4.3 Design and Construction of a Standalone Gait Diagnosis Device

4.3.1 Introduction

The performance of machine learning strongly depends on its input data. Frequently chosen machine learning input data for gait analysis are spatio-temporal walking parameters, whereas in this chapter the feasibility of selecting 3-D thigh and shank angles as the features of machine learning methods is investigated. 4 machine learning methods, i.e. random forest, k-nearest neighbour, support vector machine and perceptron, are compared in term of accuracy and memory usage. The end result is a real-time standalone gait diagnosis device that is constructed using low-end microcontrollers.

The contents in Chapter 4.3 has been submitted for review for possible publication. Once published, the publication can be searched as:

Y. C. Han, K. I. Wong and I. Murray, "Comparison of Machine Learning Methods for the Construction of a Standalone Gait Diagnosis Device".

4.3.2 Experimental Setup

Fig. 4.8 and 4.9 show the IMUs were strapped in front of the right thigh and shank using Velcro straps. As shown in Fig. 4.9(b), the right knee was bandaged to simulate knee problem, while in Fig. 4.9(c) an 8-cm high left slipper was worn to simulate leg length discrepancy.

5 healthy adults (male: 3; female: 2; age: 22-32; height: 160-177cm; weight: 55-90kg) participated in the data collection during the design phase. The volunteers stood still for about 5 seconds, then walk straight on a flat surface for 3 to 5 steps, and finally stood still for another 5 seconds to collect the 3-D rotation angles of the right thigh and shank. Table 4.3 lists the types of walking performed by each volunteer.

40 walking trials were collected from each volunteer, resulting in a total of 200 walking trials. A total of 152 normal walking cycles and 461 abnormal walking cycles were extracted from the collected walking trials in the design phase.

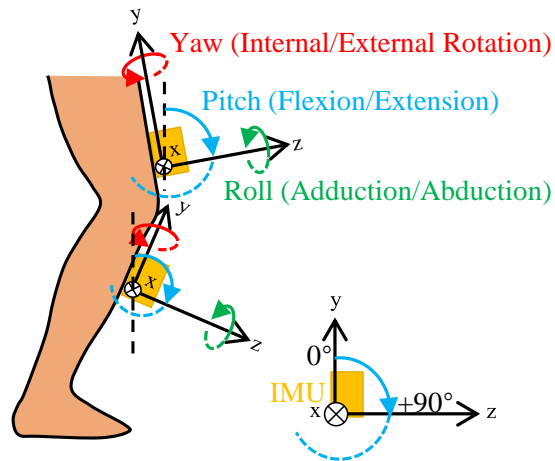


Fig. 4.8: IMUs' placement and axes direction.

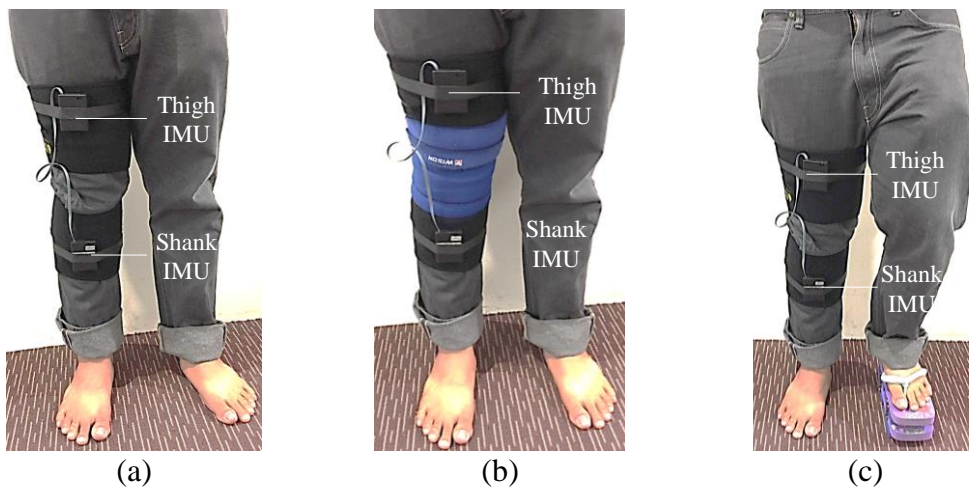


Fig. 4.9: Placement of IMUs.

- (a) Placement of the IMUs in front of the right thigh and shank using Velcro straps.
 (b) Bandaged knee to stimulate knee problem. (c) Wearing a left slipper to simulate leg length discrepancy.

Table 4.3: Type of Walking Performed by Each Volunteer

Trial	Type of Walking
1 – 10	Walk normally
11 – 20	Walk abnormally by swinging the right leg outwards to simulate foot drop
21 – 30	Walk abnormally by bandaging the knee as shown in Fig. 4.9 (b) to simulate knee problem
29 – 40	Walk abnormally by wearing an 8cm-high slipper on the left leg as shown in Fig. 4.9 (c) to simulate leg length discrepancy

In the prototype-construction phase, 2 IMUs as shown in Fig. 4.10 were constructed to process the sensor data locally and in real time. The electronic components used in the standalone IMUs were similar to that in Fig. 3.1, except there was no transceiver, and a green and a red LEDs were added to show normal and abnormal gaits, respectively. The total cost of the electronic components used to construct the standalone IMUs was about 34MYR (\approx US\$8) as listed in Table 4.4.

To test the standalone gait diagnosis device, another 15 healthy adults (male: 11; female: 4; age: 22-38; height: 158-177cm; weight: 52-90kg) were involved. Each volunteer performed the same walking as described in Table 4.3, and a total of 600 walking trials were used to test the standalone gait diagnosis device.

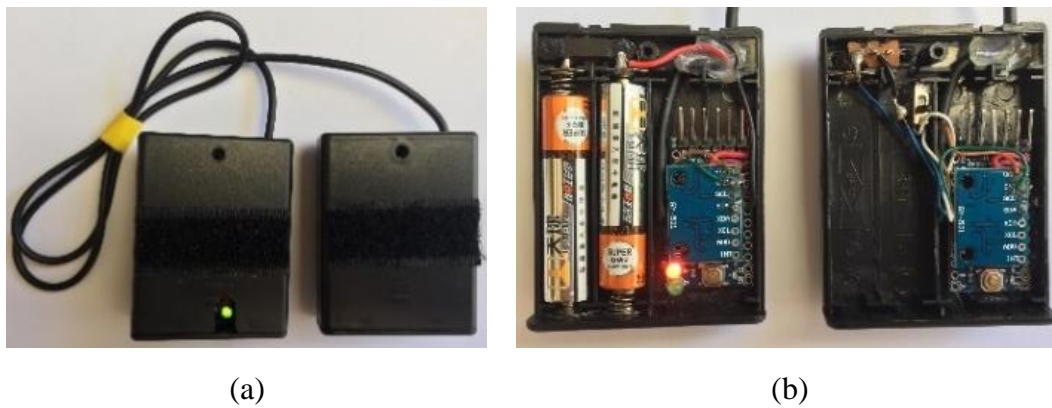


Fig. 4.10: Standalone gait diagnosis device.

(a) Standalone IMUs as a gait diagnosis device. Green LED lights up to show the gait is normal. (b) Internal view. Red LED lights up to show the gait is abnormal.

Table 4.4: Cost of the Electronic Components used in the Standalone Gait Diagnosis Device

Components	Quantity	Price per Unit (MYR)	Total Cost (MYR)
Arduino Pro Mini 3.3V	2	10.73	21.46
Sensor MPU6050	2	4.35	8.70
AAA Battery	2	1.50	3.00
LED	2	0.50	1.00
Total Cost			34.16

4.3.3 Proposed Method

4.3.3.1 Overall flowchart

This section investigates which combination of 3-D thigh and shank angles can result in the highest classification accuracy for normal and abnormal gaits. The machine learning methods were also compared in term of accuracy and memory requirement. The flowchart in Fig. 4.11 shows the overall flowchart to train a machine learning method.

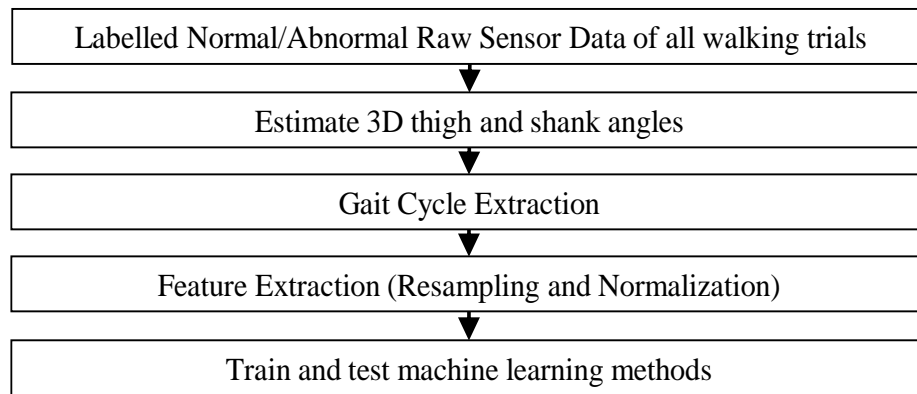


Fig. 4.11: Overall flowchart to train a machine learning method.

4.3.3.2 Estimate 3-D Thigh and Shank Angles

Fig. 4.12 shows the 3-D thigh and shank angles estimated using the method in Chapter 4.2 which had been validated against gold standard Vicon optical motion capture system. The same sensors, microcontrollers, and sampling frequency (100Hz) were used.

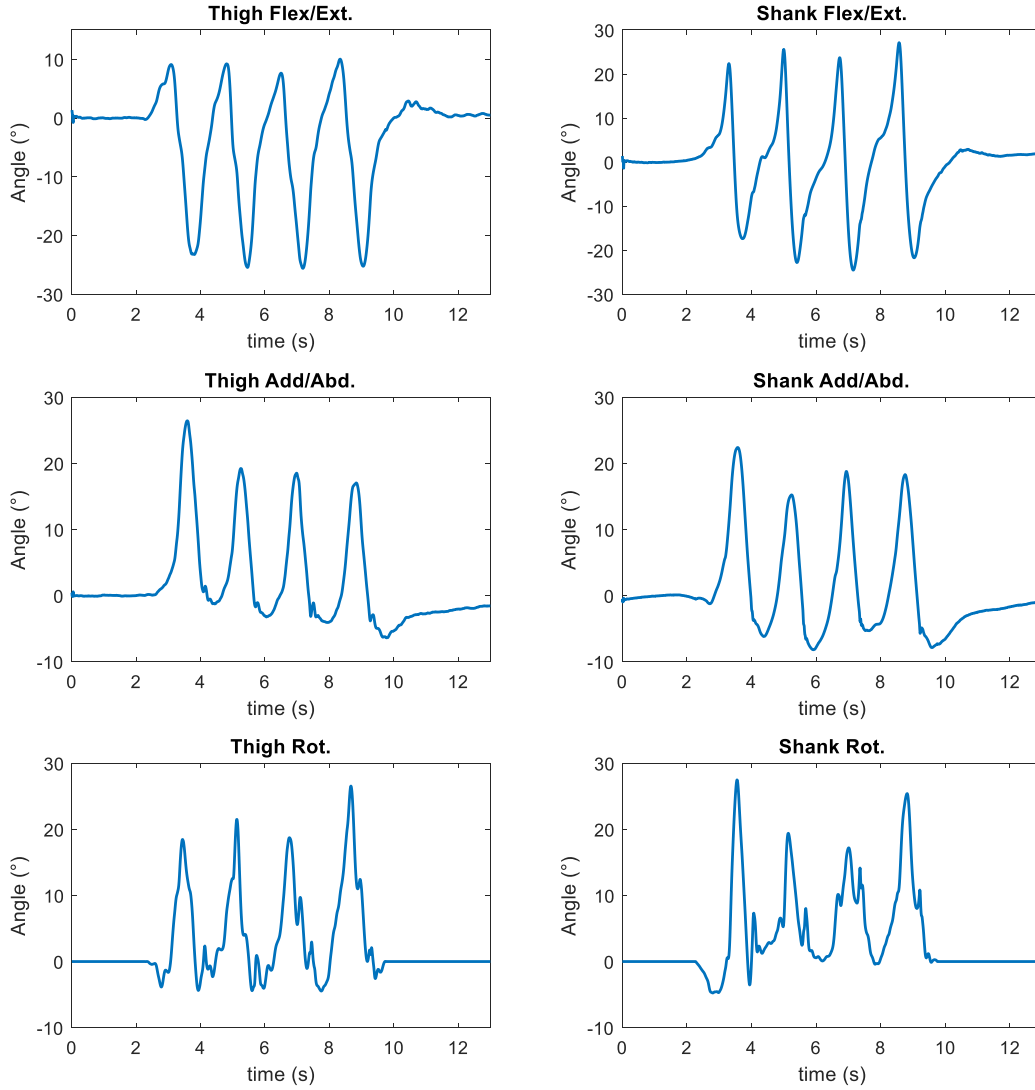


Fig. 4.12: 3-D thigh and shank angles of a person walking abnormally.

4.3.3.3 Gait Cycle Extraction in Real Time

Each gait cycle was extracted using the maximum swings of the shank. In other words, a gait cycle starts with a maximum swing of the shank, and ends with a subsequent maximum swing of the same shank.

In order to identify the maximum swings of the shank, 5 conditions in (4.16) – (4.20) within a sliding window of 200 samples (grey portion) need to be fulfilled, as illustrated in Fig. 4.13. This gait cycle extraction method can be employed in real time using Arduino.

$$M_1 - m > 10^\circ \quad (4.16)$$

$$M_2 - m > 10^\circ \quad (4.17)$$

$$i_{M1} < i_m < i_{M2} \quad (4.18)$$

$$i_m = 100 \quad (4.19)$$

$$i_{M_2} - i_{M_1} > 90 \quad (4.20)$$

Where M_1 and M_2 are the first and second maxima within the sliding window of 200 samples, respectively. m denotes the minimum angle. i is the i^{th} sample of the latest 200 samples.

The maximum angles M_1 and M_2 need to be greater than the minimum angle by at least 10° as stated in (4.16) and (4.17) to make sure the gait cycle is extracted only when the person is walking. This is because the difference between the maximum and minimum angles was much less than 10° when the person was standing still. (4.18) states that M_1 should happen first, then m , and finally M_2 .

(4.19) made sure the minimum angle m occurred at the mid of the latest 200 samples, i.e. m occurs at the 100th latest sample. This is to make sure the gait cycle was only extracted once. If (4.19) was not considered, the same gait cycle extracted in Fig. 4.13 would be re-extracted when a new sample was collected. Additionally, M_1 and M_2 would happen within 100 samples before and after m , respectively.

The final condition (4.20) states that the duration of the gait cycle needs to be more than 0.9 seconds. This is because the average duration of a gait cycle is 1.01 seconds/step [102].

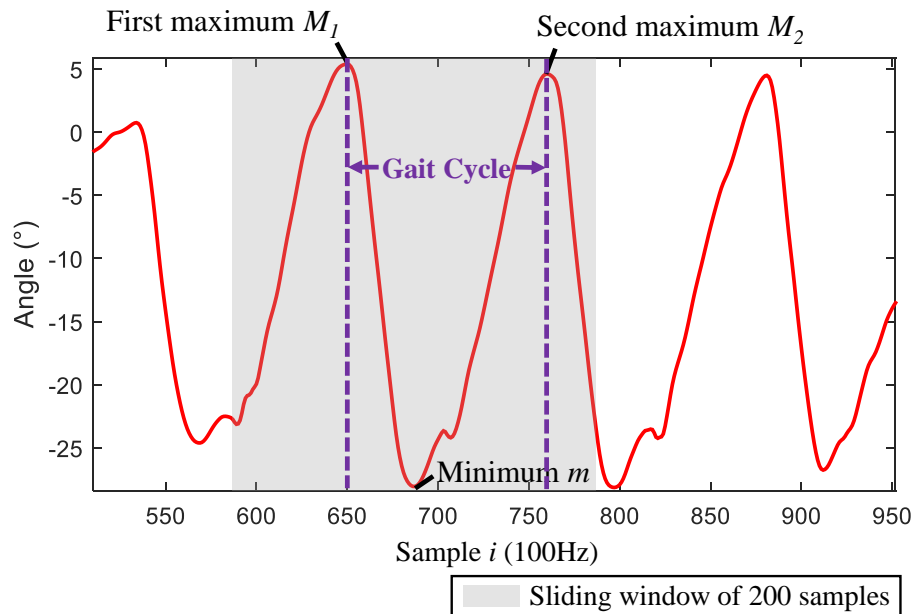


Fig. 4.13: Shank's flexion/extension angles of a normal gait. Dotted purple lines show the extracted gait cycle.

4.3.3.4 Feature Extraction (Resampling and Normalization)

After extracting the gait cycle, the estimated angles θ within a gait cycle were resampled to 11 points, where the first and last samples remained as the first and last angles of the gait cycle, respectively. The remaining 9 samples were resampled with equivalent time interval as shown in Fig. 4.14 (green cross). The resampled angle $\bar{\theta}$ can be obtained in (4.21).

$$\bar{\theta}_j = \theta_{i_{M1} + \lfloor \frac{j-1}{10}(i_{M2} - i_{M1}) \rfloor} \quad \text{for } j = 1, 2, \dots, 11 \quad (4.21)$$

Where i denotes the i^{th} sample of the latest 200 samples. $\lfloor \cdot \rfloor$ is a floor function.

The resampled angles $\bar{\theta}$ waveform patterns were linearly transformed according to (4.22) such that the last angle $\bar{\theta}_{11}$ was ‘corrected’ to be the same as the first angle $\bar{\theta}_1$. This is reasonable because walking is a repetitive motion, and hence the first and last angles of a gait cycle should ideally be almost the same. φ (blue cross in Fig. 4.14) denotes the ‘corrected’ angle.

$$\varphi_j = \bar{\theta}_j - \frac{j-1}{10}(\bar{\theta}_{11} - \bar{\theta}_1) \quad \text{for } j = 1, 2, \dots, 11 \quad (4.22)$$

Next, the negative angles are removed by subtracting all angles φ from the minimum angle according to (4.23). α (black cross in Fig. 4.14) is the extracted features for the machine learning algorithms. As the first and last resampled angles were transformed to have the same amplitudes in (4.22), 10 angles are used as the features α of the machine learning algorithms.

$$\alpha_n = \varphi_n - \min(\varphi_{1 \rightarrow 10}) \quad \text{for } n = 1, 2, \dots, 10 \quad (4.23)$$

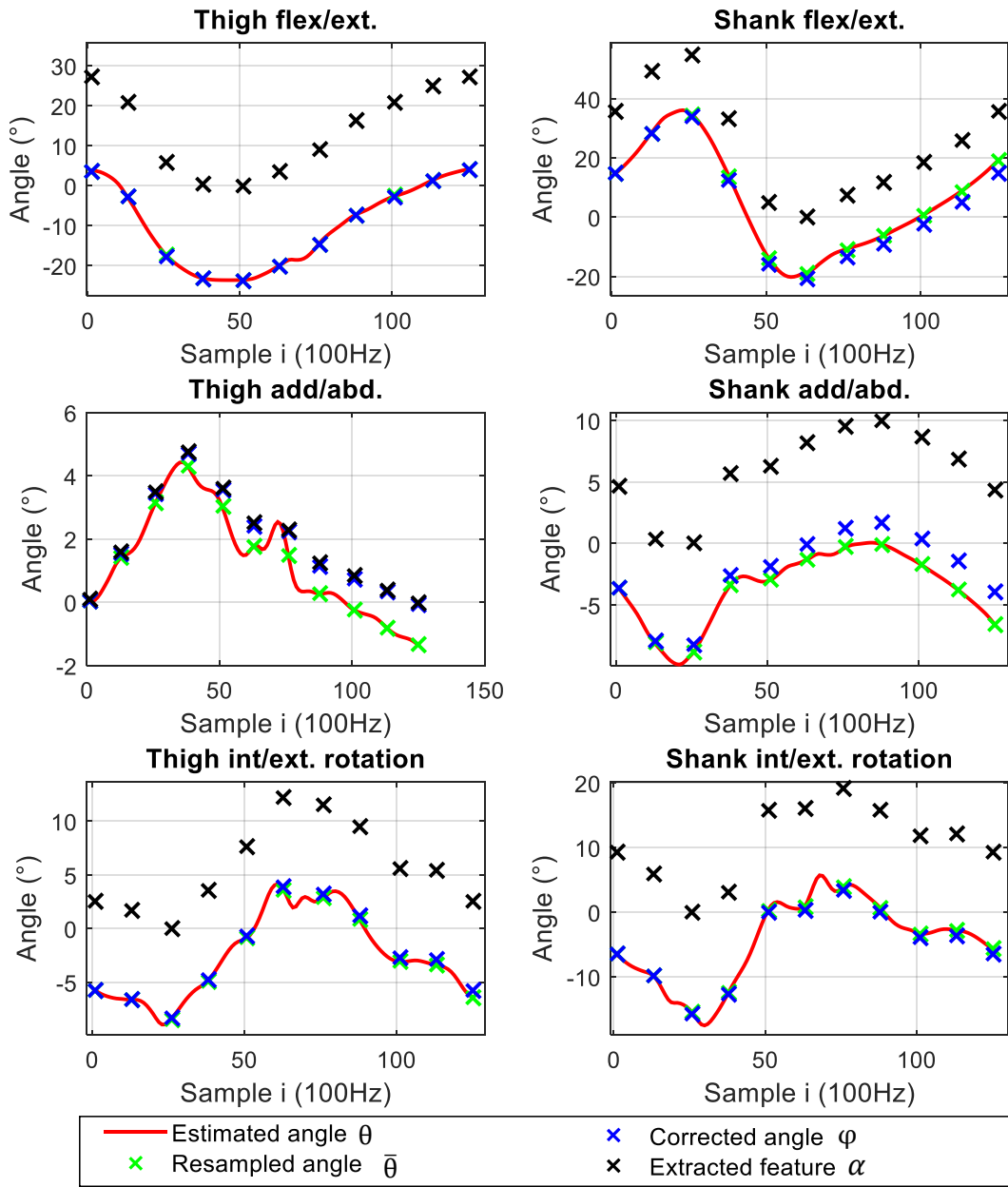


Fig. 4.14: Resampling and normalization of 3-D angles.

4.3.3.5 Feature and Machine Learning Technique Selection

4 machine learning methods, i.e. random forest (RF), k-nearest neighbor (kNN), support vector machine (SVM), and perceptron, were compared in this chapter. These machine learning methods were run using MATLAB default setting. The performance of machine learning strongly depends on its input data [103]. Therefore, different configurations of features α were input to the machine learning algorithms, in order to identify which 3-D angles are useful in gait diagnosis. Table 4.5 shows the format of the features. For example, in the 3rd configuration, the features α_1 to α_{10} are P_{thigh} , while α_{11} to α_{20} are R_{thigh} .

Table 4.5: Format of Features

Configuration	Features α					
	α_1 - α_{10}	α_{11} - α_{20}	α_{21} - α_{30}	α_{31} - α_{40}	α_{41} - α_{50}	α_{51} - α_{60}
1	P_{thigh}	-	-	-	-	-
2	P_{shank}	-	-	-	-	-
3	P_{thigh}	R_{thigh}	-	-	-	-
4	P_{shank}	R_{shank}	-	-	-	-
5	P_{thigh}	R_{thigh}	Y_{thigh}	-	-	-
6	P_{shank}	R_{shank}	Y_{shank}	-	-	-
7	P_{thigh}	P_{shank}	-	-	-	-
8	P_{thigh}	P_{shank}	R_{thigh}	-	-	-
9	P_{thigh}	P_{shank}	R_{shank}	-	-	-
10	P_{thigh}	P_{shank}	R_{thigh}	R_{shank}	-	-
11	P_{thigh}	P_{shank}	R_{thigh}	R_{shank}	Y_{thigh}	Y_{shank}

P , R and Y represent the resampled and normalized pitch (flexion/extension), roll (adduction/abduction), and yaw (internal/external rotation) angles, respectively. For example, P_{thigh} is the thigh's resampled and normalized pitch angle. R_{shank} is the shank's resampled and normalized roll angle.

Walking data from 4 volunteers were used to train the machine learning methods, while the data from the remaining volunteer was used for testing (See Table 4.6).

The accuracy of the machine learning methods was calculated using (4.24), while the average correct detection of normal and abnormal gaits was calculated using (4.25) and (4.26), respectively.

$$\text{Accuracy} = \frac{\text{Number of correctly classified gaits}}{\text{Total number of gait cycles}} \quad (4.24)$$

$$\text{Specificity} = \frac{\text{Number of correctly classified normal gaits}}{\text{Total number of normal gait cycles}} \quad (4.25)$$

$$\text{Sensitivity} = \frac{\text{Number of correctly classified abnormal gaits}}{\text{Total number of abnormal gait cycles}} \quad (4.26)$$

Table 4.6: Selection of Dataset to Train and Test Machine Learning Methods

Training Data	Testing Data	Repeat
1 st , 2 nd , 3 rd , 4 th volunteers	5 th volunteer	50 times
1 st , 2 nd , 3 rd , 5 th volunteers	4 th volunteer	50 times
1 st , 2 nd , 5 th , 4 th volunteers	3 th volunteer	50 times
1 st , 5 th , 3 rd , 4 th volunteers	2 nd volunteer	50 times
5 th , 2 nd , 3 rd , 4 th volunteers	1 st volunteer	50 times

4.3.3.6 Memory Requirement

Another requirement of the standalone gait diagnosis device is that it needs to be built using low-end microcontroller so that the cost of the device can be kept as low as possible. A low-end microcontroller like Atmega168 used in Arduino Pro Mini 3.3V has a flash memory of 16 kB (of which 2kB is used for bootloader), 1 kB of SRAM and 512 bytes of EEPROM [96]. Therefore, there is a limited number of integers or floating numbers that can be stored on the gait diagnosis device.

The number of integers and floating numbers needed to store a trained random forest N_{RF} on the standalone device can be approximated using (4.27). Based on observations, each decision tree used an average of 15 comparators. Therefore, there will be an average of 15 comparators and 15 floating numbers per decision tree.

$$N_{RF} \approx 30N_{tree} \quad (4.27)$$

The amount of floating numbers used by a trained k-nearest neighbor N_{kNN} can be approximated using (4.28). k-nearest neighbor requires the training data to be stored

on the device so that the distance between new features and the training data can be calculated for classification. The ideal group of the training data is also needed to be stored.

$$N_{kNN} \approx N_{cycle} N_{features} \quad (4.28)$$

Where N_{cycle} denotes the number of gait cycles used for training, and $N_{features}$ denotes the number of features used.

The number of support vectors are dependent on the training data. Based on observations, the number of support vectors is 3% of N_{cycle} in this research. The total number of floating numbers N_{SVM} in the support vectors can be approximated using (4.29).

$$N_{SVM} \approx 0.03 N_{cycle} N_{features} \quad (4.29)$$

In perceptron, each feature is multiplied by a weight, and finally a bias is added. The number of floating numbers required for perceptron $N_{Perceptron}$ is a small number as stated in (4.30).

$$N_{Perceptron} = N_{features} + 1 \quad (4.30)$$

4.3.3.7 Standalone Gait Diagnosis Device based on Perceptron

Fig. 4.15 shows the overall flowchart for the standalone gait diagnosis device. A real-time and computationally-efficient angle estimation algorithm is required for the standalone gait diagnosis device. The simplest angle estimation method in (4.31) which is prone to gyroscope drift is used. The gyroscope drift was not a problem as it would be ‘corrected’ through normalization in (4.22).

$$\begin{aligned} \theta_i &= 0^\circ & \text{for } i = 1 \\ \theta_i &= \theta_{i-1} + \omega_i T & \text{for } i = 2, 3, 4, \dots \end{aligned} \quad (4.31)$$

Where θ denotes the estimated angles, i denotes the i^{th} sample, ω denotes the raw angular velocity measured by gyroscope, and $T = 0.01\text{s}$ denotes the sampling period.

The gait cycle extraction, resampling and normalization methods used in the standalone gait diagnosis device are the same as that in Chapters 4.3.3.3 and 4.3.3.4.

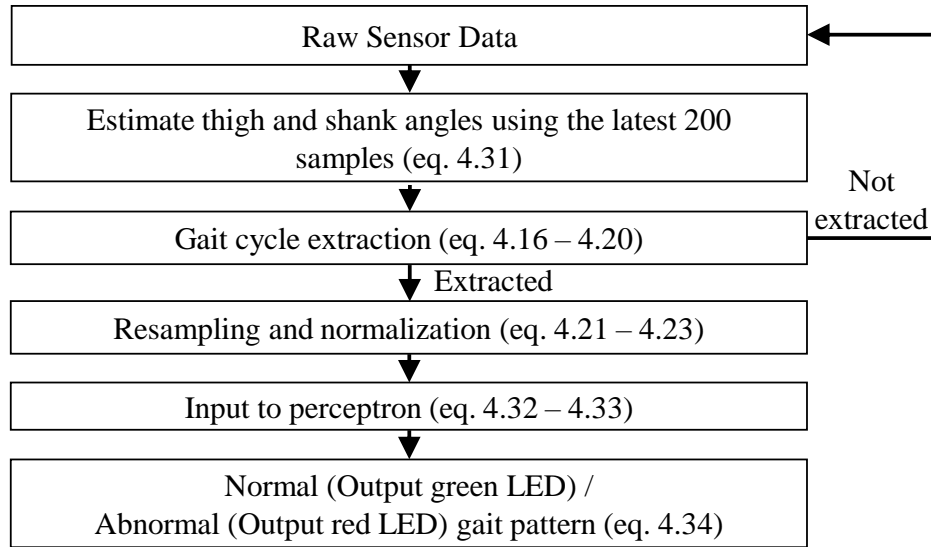


Fig. 4.15: Overall flowchart for standalone gait diagnosis device.

After comparing the different machine learning techniques (in Chapter 4.3.4), the classification algorithm selected for the gait diagnosis device is perceptron. The perceptron consists of 1 hidden layer with 1 neuron, and 1 output Y as shown in Fig. 4.16. The weights W and bias b of the trained perceptron were stored in the gait diagnosis device.

Each feature α is multiplied with a weight W . The multiplication of α and W is then added together with a bias b as stated in (4.32). The perceptron output Y was scaled to a range of ± 1 using a hyperbolic tangent sigmoid transfer function in (4.33).

$$c = b + \sum_{n=1}^N \alpha_n W_n \quad (4.32)$$

$$Y = \frac{2}{1 + e^{-2c}} - 1 \quad (4.33)$$

Where e denotes the exponential function.

A gait was identified as normal when the output y was greater than 0.5. The gait was identified as abnormal when the output Y was lower than and equal to 0.5. The green LED connected to the device lights up when normal gait is identified, while red LED lights up when abnormal gait is identified.

$$\begin{aligned} Y > 0.5 & \quad \text{normal gait} \\ Y \leq 0.5 & \quad \text{abnormal gait} \end{aligned} \quad (4.34)$$

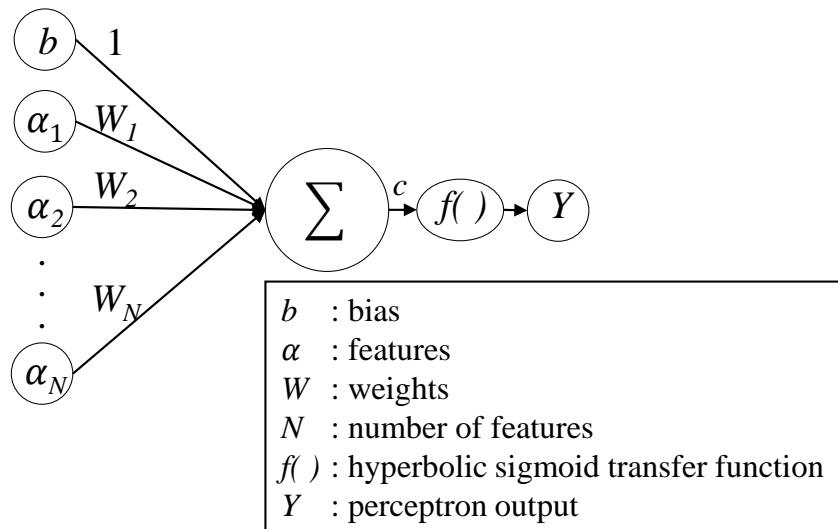


Fig. 4.16: Perceptron.

4.3.4 Results and Discussion

For better accuracy comparison among the machine learning techniques, the number of decision trees T for RF and value of K for kNN first need to be decided. Feature configuration 11 (refer to Table 4.5), i.e. all features extracted from the 3-D thigh and shank angles, were used to determine the mean accuracy, specificity and sensitivity of the RF and kNN at varying parameters as shown in Fig. 4.15. $T=15$ for RF and $K=10$ for kNN were selected as these parameters resulted in considerably high accuracy when compared among larger parameter values. The box constraint of the SVM was also tuned, but it did not result in any large improvement in classification accuracy, therefore MATLAB default value 1 was used instead.

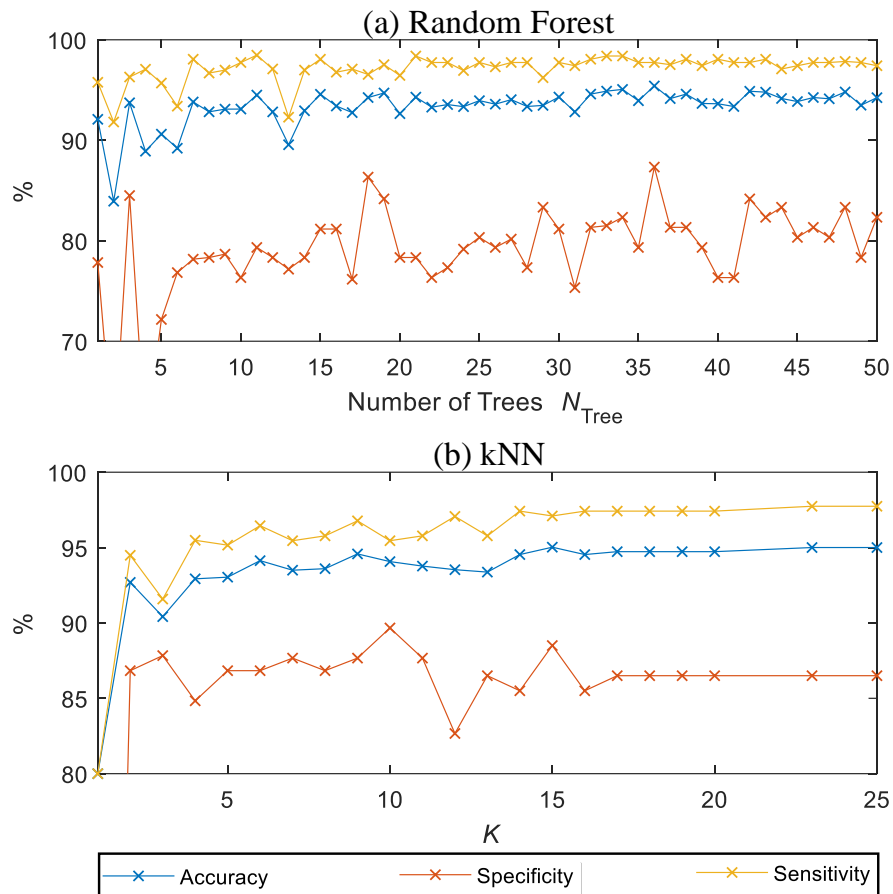


Fig. 4.17: Accuracy, Specificity, and Sensitivity of RF and kNN.

The machine learning techniques were then tested with different input feature configuration. Based on Table 4.7, support vector machine and perceptron resulted in the top two highest accuracy. Based on Table 4.8, perceptron resulted in the highest specificity. Based on Table 4.9, random forest, support vector machine and perceptron had the top three highest specificity. Overall, random forest resulted in the lowest accuracy, while k-nearest neighbor resulted in the second lowest accuracy. Therefore, support vector machine and perceptron were recommended for the standalone gait diagnosis device.

Table 4.7: Mean Accuracy of the Machine Learning Methods in Gait Diagnosis

Features α	Mean Accuracy (%)			
	Random Forest ($N_{tree}=15$)	k-Nearest Neighbor ($K=10$)	Support Vector Machine	Perceptron
P_{thigh}	96.23	96.87	96.13	95.56
P_{shank}	93.10	92.88	97.70	96.79
P_{thigh}, R_{thigh}	93.67	95.93	98.62	97.12
P_{shank}, R_{shank}	85.86	87.92	97.63	96.84
$P_{thigh}, R_{thigh}, Y_{thigh}$	93.62	90.75	98.54	96.65
$P_{shank}, R_{shank}, Y_{shank}$	91.20	90.75	94.87	96.82
P_{thigh}, P_{shank}	95.22	95.98	98.17	98.45
$P_{thigh}, P_{shank}, R_{thigh}$	94.98	94.69	97.25	97.52
$P_{thigh}, P_{shank}, R_{shank}$	94.22	96.15	97.29	98.27
$P_{thigh}, P_{shank}, R_{thigh}, R_{shank}$	93.53	93.96	97.97	97.75
$P_{thigh}, P_{shank}, R_{thigh}, R_{shank}, Y_{thigh}, Y_{shank}$	93.62	90.06	96.47	97.98

This result was obtained by training and testing the methods based on Table 4.6.

Grey colour means $\geq 96\%$ accuracy.

Table 4.8: Mean Specificity of the Machine Learning Methods in Gait Diagnosis

Features α	Mean Specificity (%)			
	Random Forest ($N_{\text{tree}}=15$)	k-Nearest Neighbor ($K=10$)	Support Vector Machine	Perceptron
P_{thigh}	89.02	93.68	97.50	88.98
P_{shank}	85.00	90.67	94.17	91.21
$P_{\text{thigh}}, R_{\text{thigh}}$	77.17	87.33	95.83	97.15
$P_{\text{shank}}, R_{\text{shank}}$	73.17	80.83	92.50	91.07
$P_{\text{thigh}}, R_{\text{thigh}}, Y_{\text{thigh}}$	74.83	67.42	95.35	93.26
$P_{\text{shank}}, R_{\text{shank}}, Y_{\text{shank}}$	76.33	88.83	90.33	91.03
$P_{\text{thigh}}, P_{\text{shank}}$	84.33	92.50	97.20	96.34
$P_{\text{thigh}}, P_{\text{shank}}, R_{\text{thigh}}$	83.33	90.83	95.00	96.53
$P_{\text{thigh}}, P_{\text{shank}}, R_{\text{shank}}$	86.33	89.67	93.33	96.59
$P_{\text{thigh}}, P_{\text{shank}}, R_{\text{thigh}}, R_{\text{shank}}$	77.17	87.00	94.00	97.20
$P_{\text{thigh}}, P_{\text{shank}}, R_{\text{thigh}}, R_{\text{shank}}, Y_{\text{thigh}}, Y_{\text{shank}}$	79.00	89.50	88.83	95.49

This result was obtained by training and testing the methods based on Table 4.6.

Grey colour means $\geq 96\%$ specificity.

Table 4.9: Mean Sensitivity of the Machine Learning Methods in Gait Diagnosis.

Features α	Mean Sensitivity (%)			
	Random Forest ($N_{tree}=15$)	k-Nearest Neighbor ($K=10$)	Support Vector Machine	Perceptron
P_{thigh}	97.90	97.46	95.46	97.15
P_{shank}	95.40	93.86	98.71	98.55
P_{thigh}, R_{thigh}	97.95	97.96	99.30	97.10
P_{shank}, R_{shank}	89.65	90.38	99.03	98.65
$P_{thigh}, R_{thigh}, Y_{thigh}$	98.70	96.02	99.19	97.31
$P_{shank}, R_{shank}, Y_{shank}$	95.46	91.56	95.90	98.59
P_{thigh}, P_{shank}	98.38	96.97	98.27	98.99
$P_{thigh}, P_{shank}, R_{thigh}$	98.06	95.88	97.83	97.87
$P_{thigh}, P_{shank}, R_{shank}$	96.40	98.00	98.30	98.72
$P_{thigh}, P_{shank}, R_{thigh}, R_{shank}$	97.74	95.98	99.00	97.94
$P_{thigh}, P_{shank}, R_{thigh}, R_{shank}, Y_{thigh}, Y_{shank}$	97.42	90.69	98.73	98.79

This result was obtained by training and testing the methods based on Table 4.6.

Grey colour means $\geq 96\%$ sensitivity.

Other than Table 4.6, another method to train and test a machine learning method is by selecting the training and testing data randomly. Referring to Table 4.10, the average accuracy of the perceptron was high (96-97%) even when only 10% of randomly chosen training data was used. This showed that the number of walking trials collected in this research was more than sufficient. The accuracy increased as the number of training data increased.

It has to be noted that the accuracy of the perceptron in Table 4.10 is higher than that in Table 4.6. This is because by randomly selecting data, it is possible to train the gait pattern of a person to test the gait pattern of the same person. In Table 4.6, however, the trained perceptron was tested using the gait pattern of different person. Therefore, the training and testing method in Table 4.6 better described the accuracy of the proposed method.

Table 4.10: Mean Accuracy of the Perceptron in Design Phase by Randomly Selecting Training and Testing Data.

Features α	Accuracy (%)		
	Training data 10%	Training data 30%	Training data 50%
P_{thigh}	96.05	97.27	97.45
$P_{\text{thigh}}, P_{\text{shank}}$	97.22	98.82	99.14
$P_{\text{thigh}}, P_{\text{shank}}, R_{\text{shank}}$	97.14	98.27	99.40
$P_{\text{thigh}}, P_{\text{shank}}, R_{\text{thigh}}, R_{\text{shank}},$ $Y_{\text{thigh}}, Y_{\text{shank}}$	96.77	98.59	98.61

This result was obtained by randomly selecting training and testing data. For example, training data = 30%; testing data = remaining 70%. Each result was the average of 50 runs. Grey colour means $\geq 96\%$.

Table 4.11 shows the approximated number of integers and floating numbers to be stored on the gait diagnosis device. Perceptron required the least amount of floating numbers to be stored on the gait diagnosis device, followed by support vector machine, random forest, and finally k-nearest neighbor.

Table 4.11: Memory Requirement: Approximated Number of Integers and Floating Numbers to be Stored on Gait Diagnosis Device.

Features α	Random Forest ($N_{\text{tree}}=15$)	k-Nearest Neighbor ($K=10$)	Support Vector Machine	Perceptron
$\alpha_1 - \alpha_{10}$	450	6130	184	11
$\alpha_1 - \alpha_{20}$	450	12260	368	21
$\alpha_1 - \alpha_{30}$	450	18390	552	31
$\alpha_1 - \alpha_{40}$	450	24520	736	41
$\alpha_1 - \alpha_{50}$	450	30650	920	51
$\alpha_1 - \alpha_{60}$	450	36780	1104	61

As perceptron results in the top two highest accuracy and having the lowest memory requirement, perceptron was chosen to be the classification algorithm for the

standalone gait diagnosis device. Based on Tables 4.7 to 4.9, the following analysis was made to identify the best feature configuration for the perceptron.

- 1) Using P_{thigh} or P_{shank} alone resulted in lower accuracy
 - P_{thigh} resulted in the lowest accuracy among other configurations.
 - P_{shank} resulted in 2% lower accuracy than the maximum accuracy.
- 2) R only helped to improve the accuracy in certain cases.
 - ' $P_{thigh} R_{thigh}$ ' increased the accuracy by 1.5% compared to ' P_{thigh} ' alone.
 - ' $P_{shank} R_{shank}$ ' and ' P_{shank} ' resulted in almost the same accuracy.
 - ' $P_{shank} R_{shank}$ ' resulted in 0.2-1.0% higher accuracy compared to ' $P_{thigh} P_{shank} R_{thigh}$ ', ' $P_{thigh} P_{shank} R_{shank}$ ' and ' $P_{thigh} P_{shank} R_{thigh} R_{shank}$ '.
- 3) Y slightly reduced the accuracy.
 - ' $P_{thigh} R_{thigh} Y_{thigh}$ ' and ' $P_{shank} R_{shank} Y_{shank}$ ' resulted in slightly lower accuracy compared to ' $P_{thigh} R_{thigh}$ ' and ' $P_{shank} R_{shank}$ ', respectively.
- 4) ' $P_{thigh} P_{shank}$ ' and ' $P_{thigh} P_{shank} R_{shank}$ ' resulted in the top two highest accuracy.

Therefore, possible feature configurations are ' $P_{thigh} R_{shank}$ ' and ' $P_{thigh} P_{shank} R_{shank}$ '. These two configurations are further tested using the standalone gait diagnosis device. Referring to Table 4.12, when ' $P_{thigh} P_{shank}$ ' was used, the mean accuracy of the standalone gait diagnosis device was low at 79.5%. The main reason was the trained perceptron performed badly for the second type of walking, i.e. leg moving outwards.

However, when ' $P_{thigh} P_{shank} R_{shank}$ ' was used, the mean accuracy improved to 96.50%. The main reason for this improvement was R_{shank} contained the information to detect whether the leg adducted/abducted. Therefore, the final choice of feature configuration for the standalone gait diagnosis device is ' $P_{thigh} P_{shank} R_{shank}$ '.

Table 4.12: Mean Accuracy, Specificity and Sensitivity of the Standalone Gait Diagnosis Device.

Perceptron input α	Accuracy (%)	Specificity (%)	Sensitivity (%)
P_{thigh}, P_{shank}	79.50	94.00	74.67
$P_{thigh}, P_{shank}, R_{shank}$	96.50	98.00	96.00

This result was obtained from 15 volunteers. Each volunteer was requested to perform 10 trials per type of walking as stated in Table 4.3. Grey colour means $\geq 96\%$.

The proposed method was also tested with new types of abnormal walking as shown in Table 4.13. ‘Walk with heel’ had considerably high sensitivity at 92% initially, most likely because the knee angle was low almost similar to trained pattern ‘knee bandaged’. For the ‘walk with toe’, ‘cat walk’ and ‘mechanical perturbations’, the sensitivity of the device was very low as the perceptron was not trained using these new walking types.

Then, the perceptron was re-trained with new types of walking pattern. The newly trained perceptron then provides a high mean sensitivity of at least 94% for the new abnormal walking patterns. Therefore, it was proven that the accuracy of the proposed method could be improved by increasing the types of abnormal walking pattern in perceptron training.

Table 4.13: Mean Sensitivity of the Proposed Method Before and After Training with New Abnormal Walking Pattern.

Type of Walking	Sensitivity (%)	
	Before	After
Walk with heel	92.00	96.00
Walk with toe	32.00	94.00
Cat walk	10.00	94.00
Mechanical perturbations [104]	0.00	98.45

- ‘Walk with heel’, ‘walk with toe’ and ‘cat walk’ dataset was collected by 7 volunteers, each performed 10 walking trials per type of walking. Dataset from 5 volunteers were used for training, while dataset for another 2 volunteers were used for testing.
- ‘Mechanical permutations’ dataset is obtained from [104]. This dataset consists of more than 20,000 perturbed walking gait cycles which were caused by random speed change in treadmill belt. For balanced training dataset, only 150 randomly selected abnormal walking gait cycles from [104] were used for training with the 152 normal walking cycles and 461 abnormal walking cycles collected in Chapter 4.3.2, while the remaining abnormal gait cycles from [104] were used for testing.
- Grey colour means $\geq 96\%$.

It is also worthwhile to compare the proposed method with some existing methods for feature-based comparison. In [53], Fourier transform of the gait data waveforms were used for gait classification. This is reasonable because Fourier transform could reconstruct all amplitudes of the 3-D angles. 5 to 6 harmonic components were usually used to reconstruct the angle waveforms [62] [66]. In this experiment, 5 harmonic components (consisting of 5 instantaneous amplitudes and 5 phases) of the angle waveforms were chosen as features, so that the number of features is the same as proposed method (10 angles extracted from an angle waveform). It is also worthwhile to compare the proposed method with existing method that uses acceleration and angular velocity for gait classification. Mikos *et al.* [43] extracted 3 features, i.e. freeze index from the acceleration, stride peak of the angular velocity, and standard deviation of the angular velocity.

Although RF and kNN performed worse than SVM and perceptron using the extracted features in proposed method, kNN outperformed SVM and perceptron when DFT features were used. As shown in Table 4.14, AccGy and DFT features resulted in higher accuracy than the proposed method when RF and kNN were used. However, the proposed method resulted in higher accuracy than AccGy and DFT features when SVM and perceptron were used. The drawback of the AccGy and DFT features are that the feature extraction requires Fourier transform which is considered computationally expensive for low-end microcontrollers. The proposed method is preferable when using SVM and perceptron as the feature extraction is computationally lightweight which is especially important when the purpose is to construct a low-cost standalone gait diagnosis device.

Table 4.14: Feature based comparison among related work.

	Feature	RF <i>T</i> =15	RF <i>T</i> =25	kNN <i>K</i> =10	kNN <i>K</i> =25	SVM	Perceptron
Accuracy	AccGy	94.00	95.17	90.67	91.17	92.50	91.88
	DFT	95.26	95.70	96.69	97.33	93.32	95.06
	Prop.	93.62	93.94	94.07	95.00	96.47	97.98
Specificity	AccGy	77.39	79.13	75.65	79.13	82.61	83.67
	DFT	81.00	87.50	90.50	92.33	90.00	89.70
	Prop.	79.00	80.33	89.67	86.50	88.83	95.49
Sensitivity	AccGy	97.94	98.97	94.23	94.02	94.85	93.83
	DFT	99.35	97.95	98.39	98.71	94.32	96.53
	Prop.	97.42	97.74	95.46	97.74	98.73	98.79

- AccGy stands for acceleration and gyroscope. The extracted features are similar to that of Mikos *et al.* [43].
- DFT stands for discrete Fourier transform. The features are the first 5 harmonic components (5 instantaneous amplitudes and 5 phases) of the angle waveform.
- These results were obtained using all features extracted from 3-D thigh and shank sensor data.
- Grey colour means $\geq 96\%$.

4.3.5 Summary

4 machine learning methods (random forest, k-nearest neighbor, support vector machine, and perceptron) were compared. Perceptron was chosen for the standalone gait diagnosis device as it resulted in the top two highest accuracy, and used the lowest memory. The combination of the thigh and shank's flexion/extension angles, and shank's adduction/abduction angle as input feature of the perceptron resulted in the highest accuracy among other configurations of 3-D thigh and shank angles. It was discovered that the adduction/abduction angle was able to improve the classification accuracy. Internal/external rotation angles of the thigh and shank did not improve the accuracy in this research. The weights and bias of the trained perceptron were successfully transferred to a low-end microcontroller to construct a real-time standalone gait diagnosis device which cost about US\$8 only. The constructed standalone gait diagnosis device lit up green or red LEDs when normal or abnormal gaits was identified, respectively. The mean accuracy of the standalone device was high at 96.5%. However, this device could only diagnose certain walking pattern as the perceptron was only trained with 4 types of walking pattern. This can be solved by training the perceptron with more patterns.

4.4 Gait Phase Detection

4.4.1 Introduction

The importance of gait phase detection is that it is one of the methods used to evaluate and diagnose the gaits [105]. However, the current gait phase analysis is done based on visual inspection which is subjective and strongly depends on the experience of the clinicians [4]. Therefore, there is a need for autonomous gait phase detection.

In this chapter, a method to detect normal and abnormal gait phases using a single IMU attached to the shank is proposed. The local maxima, minima and zero crossings of the shank's angular velocity are used to detect heel strike, toe strike, and toe off. Some unique waveform patterns of normal/abnormal shank's angular velocity are also identified for gait diagnosis and classification. The proposed method is validated against force sensors.

Chapter 4.4 is covered by the following publication with minor amendment:

Y. C. Han, K. I. Wong and I. Murray, "Gait Phase Detection for Normal and Abnormal Gaits Using IMU," in *IEEE Sensors Journal*, vol. 19, no. 9, pp. 3439-3448, May1, 2019.

doi: 10.1109/JSEN.2019.2894143

© 2019 IEEE

4.4.2 Experimental Setup

Fig. 4.18 and 4.19 show that the IMUs were strapped in front of the right thigh and shank using Velcro straps. The IMUs were used to collect the angular velocity and acceleration of the thigh and shank. The data collected from the shank's IMU was used to detect the gait phases. The data collected from the thigh's IMU was unused in this chapter.

Similar to [9], 4 FSRs were placed under the heel, first metatarsal head, fifth metatarsal head, and the hallux, as most of the body weights were exerted on these positions during walking [6]. In contrast with [9] which integrates the FSRs in a shoe-insole, the FSRs in this research were attached directly under the foot using double-sided tape. This is because in [9], the shoe-insole of fixed size resulted in higher gait phase detection error due to different foot sizes of the test subjects. By attaching the FSRs directly under the foot using double-sided tape, the FSRs can be placed accurately under the foot of all test subjects. The FSRs were used to validate the

proposed method.

10 healthy adults (male: 7; female: 3; age: 21-28; height: 151-182cm) were participated in the data collection. Each person was asked to walk on a flat surface for about 30 continuous gait cycles per type of walking as listed in Table 4.15. A total of 1146 gait cycles was collected.

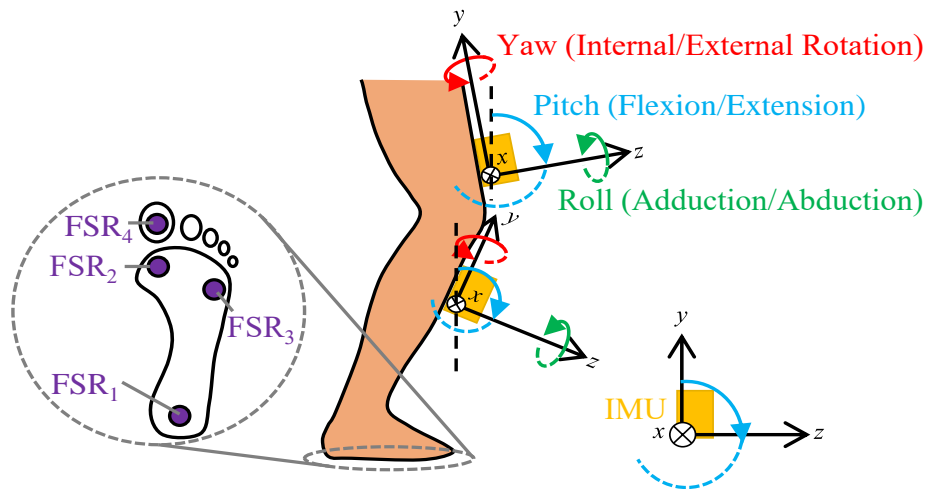


Fig. 4.18: Sensors placement.

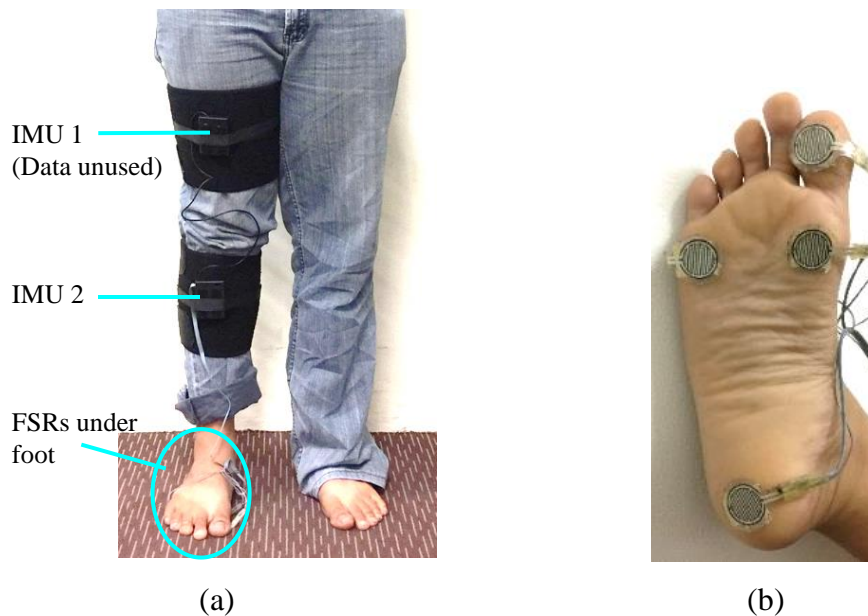


















Fig. 4.19: Placement of IMUs and FSR.

(a) Placement of IMUs in front of the right thigh and shank using Velcro stripes. (b) Placement of FSRs under the right foot using double-sided tape.

Table 4.15: Possible Gait Sub-Phases

Type of Walking	Simulation	Initial Contact	MSt	PSw	Swing
1	Normal				
2	Habit				
3	Foot drop				
4	Bandaged knee				

The greyed region is where the part of foots on ground. The white region is where the parts of foot not on ground. Note: in normal gait ‘initial contact’ is the heel strike, but in abnormal gait ‘initial contact’ could be different.

4.4.3 Proposed Method

4.4.3.1 Gait Cycle Extraction

Fig. 4.20 shows the shank’s flexion/extension angle estimated using the method in Chapter 4.2 which had been validated against gold standard Vicon optical motion capture system. The gait cycles were extracted using the maximum swings of the shank such that a gait cycle starts with a maximum swing of the shank, and ends with a subsequent maximum swing of the same shank.

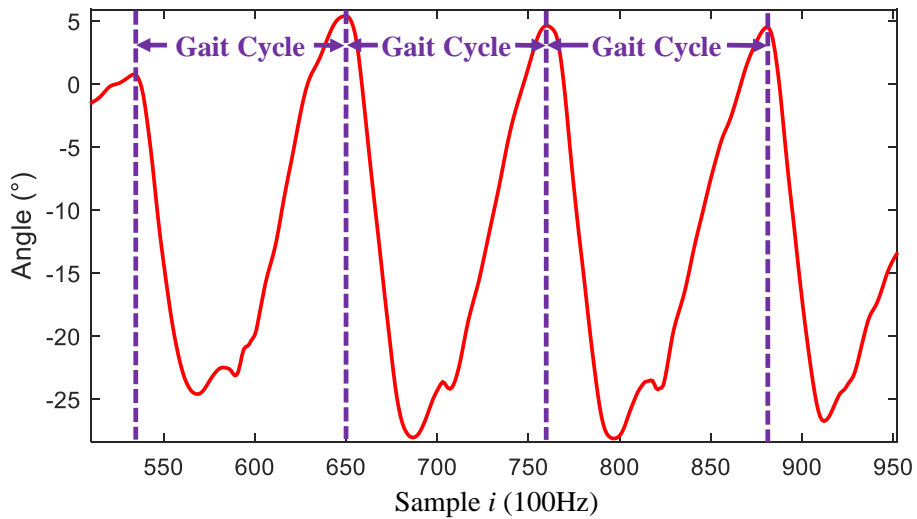


Fig. 4.20: Shank’s flexion/extension angle for gait cycle extraction.

4.4.3.2 Gait Phase Detection using Kinetic Parameters (FSRs) for Comparison

In this section, the method proposed in [9] that uses fuzzy logic to detect LR, MSt, TSt and PSw, is discussed. In [9], normal LR is detected when ‘large’ force is exerted on FSR 1, while the remaining FSRs measure ‘small’ forces. However, the initial contact (IC) of an abnormal gait pattern, such as walking type 3 in Table 4.15, may not be a heel strike, but a toe strike. Therefore, an extra condition is added in the last column (proposed method) of Table 4.16, so that abnormal LR can be detected correctly if the IC is toe strike.

The LR of walking types 2 and 4, for example, is when all FSRs detect ‘large’ forces. However, according to [9], the IC of walking types 2 and 4 would have been wrongly identified as MSt. Therefore, if the IC consists of toe and heel strikes, abnormal LR can be detected correctly using the fuzzy logic.

FSR 1 is used to detect whether the heel is on ground. FSRs 2 to 4 are used to detect whether the toe is on ground. In order to identify when the heel and toe strikes, the fuzzy logic in Table 4.17 is applied. The first moment when the heel hits the ground is called the heel strike. Similarly, the first moment when the toe hits the ground is called the toe strike. The first moment when the toe leaves the ground is called toe off.

The sigmoid functions (4.35) and (4.36) used in [9] are used to differentiate ‘large’ and ‘small’ forces applied to the FSRs. In order to fulfill the first condition in Table 4.16, for example, the AND function or minimum between $f_{\text{large}}(\text{FSR } 1)$, $f_{\text{small}}(\text{FSR } 2)$, $f_{\text{small}}(\text{FSR } 3)$, and $f_{\text{small}}(\text{FSR } 4)$ needs to be ‘1’. Detailed explanation of this method can be found in [9].

$$f_{\text{large}}(V_i) = \frac{1}{1 + e^{-V_{\text{stand}}(V_i - V_{\text{air}})}} \quad (4.35)$$

$$f_{\text{small}}(V_i) = 1 - f_{\text{large}}(V_i) \quad (4.36)$$

Where V_i denotes the voltage measured by an FSR at i^{th} sample. V_{max} is the FSR voltage when the person is applying maximum body weight onto the FSR. V_{min} is the FSR voltage when no body weight is applied onto the FSR. e is an exponential function.

Table 4.16: Fuzzy Rules for Gait Phase Detection using Kinetic Parameters

FSR 1	FSR 2	FSR 3	FSR 4	Gait phase	
				Normal [9]	Proposed method
Large	Small	Small	Small	LR	-
Large	Large	Large	Large	MSt	LR if IC
					MSt if not IC
Small	Large	Large	Large	TSt	LR if IC
					TSt if not IC
Small	Small	Small	Small	PSw	PSw

Based on Table 4.17 and the sigmoid functions (4.35) (4.36), the moment when the heel or toe is on ground can be identified as shown in Fig. 4.21.

As shown in Fig. 4.22, the heel and toe strikes occur at the same time for walking types 2 and 4. However, a normal toe strike should occur after the heel strike (as shown in walking type 1), therefore the toe strike is diagnosed as abnormal. In the 3rd type of walking, toe strike and heel strike occur in the wrong sequence, therefore both heel and toe strikes are identified as abnormal. Table 4.18 shows the ideal gait diagnosis for the 4 different types of walking stated in Table 4.17.

Table 4.17: Fuzzy Rules to Detect Heel and Toe on Ground using Kinetic Parameters

FSR 1	FSR 2	FSR 3	FSR 4	Interpretation
Large	-	-	-	Heel on ground (First moment is heel strike)
Small	-	-	-	Heel not on ground (First moment is heel off)
-	Large	Large	Large	Toe on ground (First moment is toe strike)
-	Small	Small	Small	Toe not on ground (First moment is toe off)

The 'dash' denotes don't care.

Table 4.18: Ideal Gait Diagnosis According to Gait Sub-Phases

Type of Walking	Heel Strike	Toe Strike	Toe Off
1	Normal	Normal	Normal
2	Normal	Abnormal	Normal
3	Abnormal	Abnormal	Normal
4	Normal	Abnormal	Normal

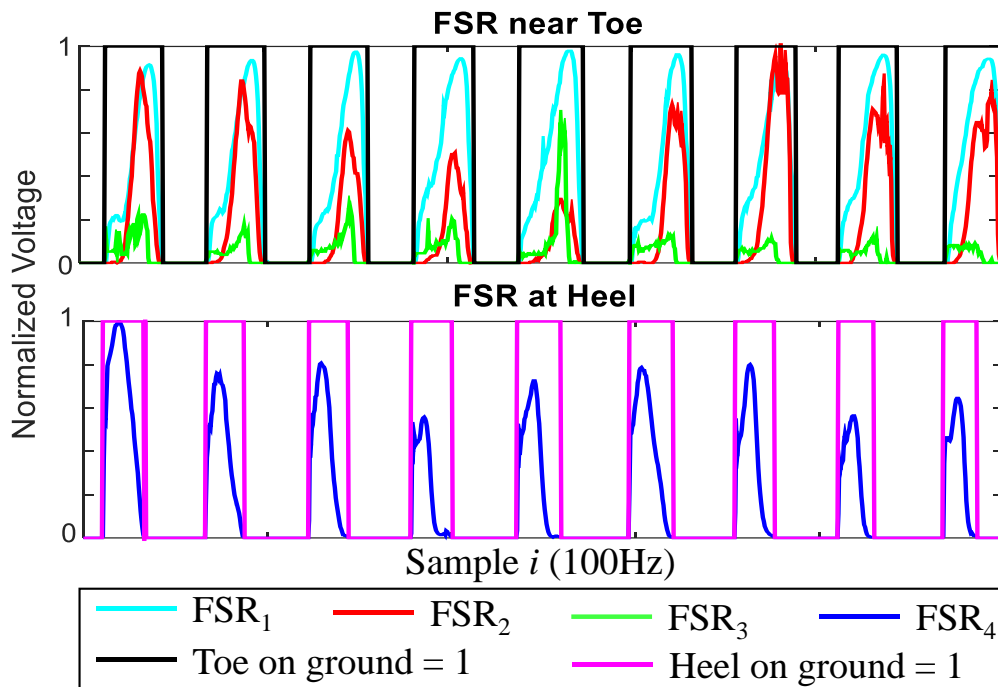


Fig. 4.21: FSR measurements during normal walking.

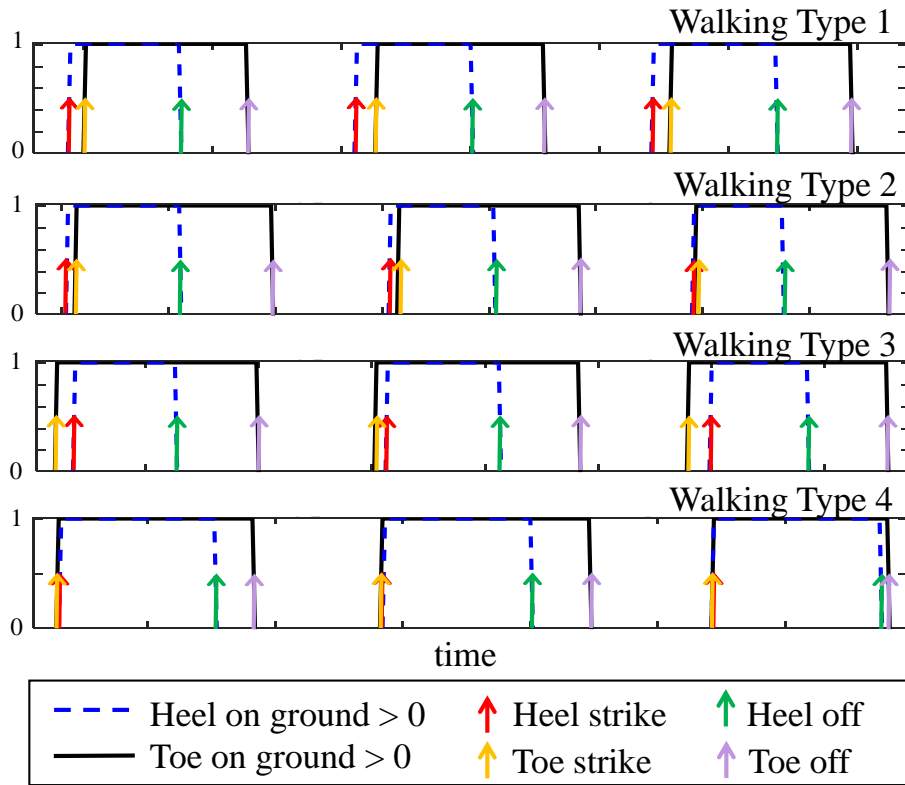


Fig. 4.22: Ideal gait phases detected using FSRs.

4.4.3.3 Gait Phase Detection using Shank's IMU for Comparison [50]

In [50], the heel strike and toe off are detected using the first and last local maxima of the shank's angular velocity respectively, as shown in Fig. 4.23. As the proposed method (to be discussed in Chapters 4.4.3.4 to 4.4.3.6) is also based on the local minima and maxima of the shank's angular velocity, it is worthwhile to compare the proposed method with [50]. The comparison can be found in Chapter 4.4.4.

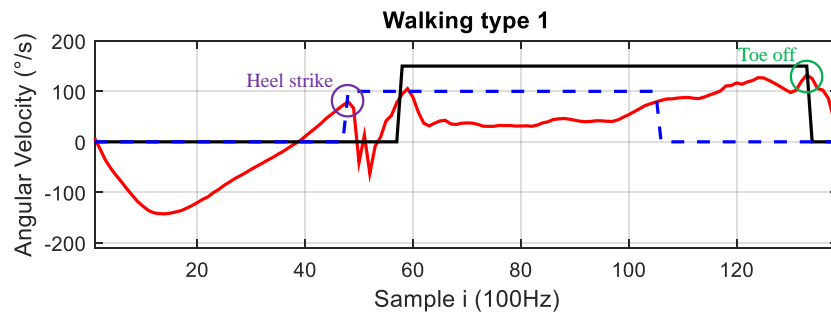


Fig. 4.23: Detection of heel strike and toe off using shank's angular velocity ω_{shank} .

4.4.3.4 Heel Strike

As shown in Fig. 4.24, when there is a 2nd positive zero crossing Z_2 of ω_{shank} , all heel strikes can be estimated using the 1st local maximum A_n of ω_{shank} before the 1st negative zero crossing Z_n .

As shown in the last gait cycle in Fig. 4.24, the heel strike is classified as abnormal when Z_n (first negative zero crossing after the first positive zero crossing) and Z_2 (second positive zero crossing) are ‘far’ (separated by more than 5 samples equivalent to 50ms). If this condition is not fulfilled, the heel strike is estimated as normal when the estimated heel strike at A_n is ‘near’ (within ± 5 samples) to A_1 (first local maximum after the first positive zero crossing) (See 1st, 2nd and 4th gait cycles in Fig. 4.24). The third gait cycle in Fig. 4.24 tells that when the above two conditions are not fulfilled, the heel strike is abnormal.

However, there are cases, as shown in all gait cycles in Fig. 4.25, that there is no second positive zero crossing Z_2 . In such case, the heel strikes are not estimated using A_n . Based on observations, such as the first gait cycle in Fig. 4.25, the heel strike is estimated using the first local maximum A_1 of ω_{shank} when A_1 has the lowest amplitudes among the first three local maxima (A_1, A_2, A_3). As seen in the second and third gait cycles in Fig. 4.25, both A_1 do not have the lowest amplitudes among A_1, A_2 and A_3 , therefore the heel strikes are not detected using A_1 , and the detection will be decided later.

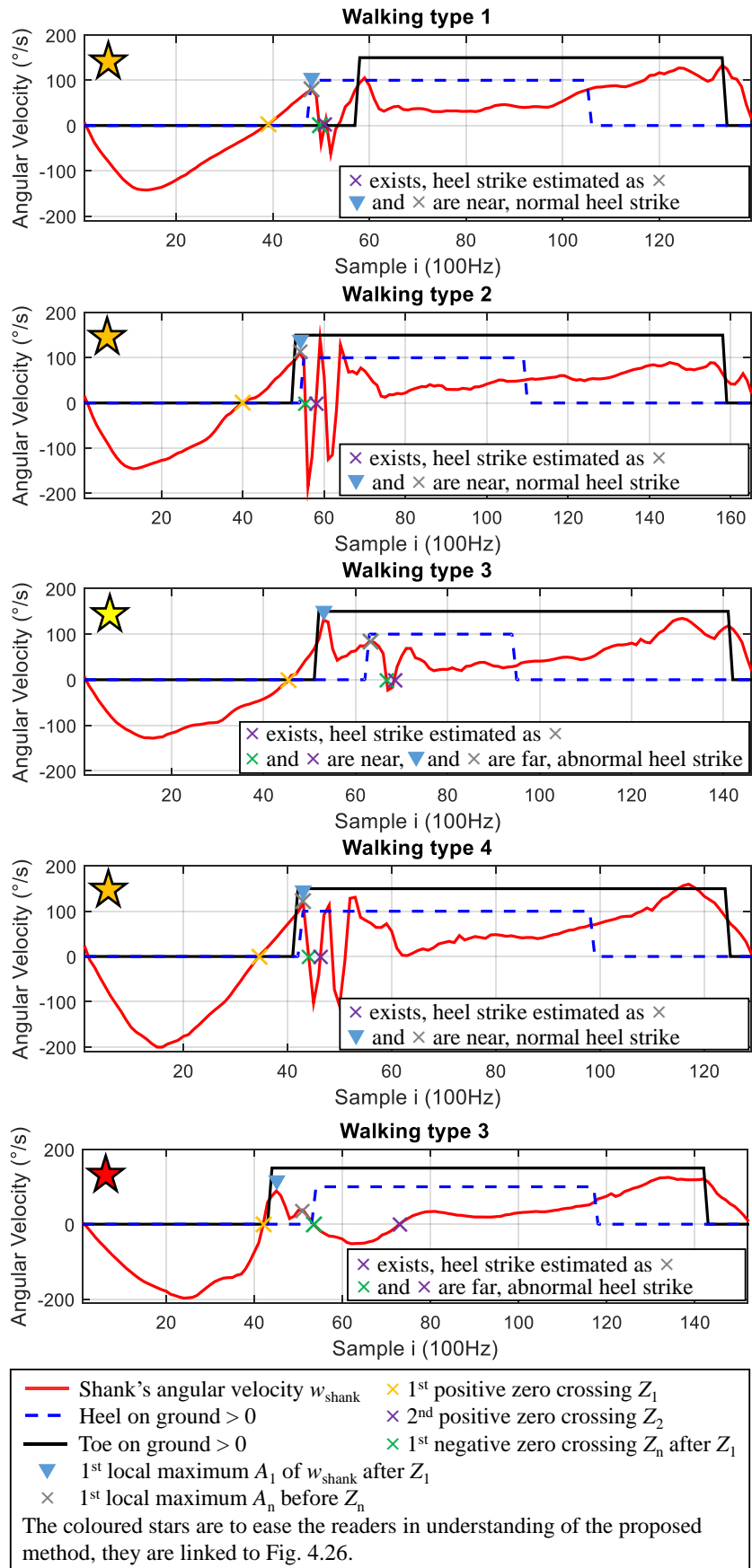


Fig. 4.24: Shank's angular velocity ω_{shank} and ideal gait phases of a volunteer walking with different patterns.

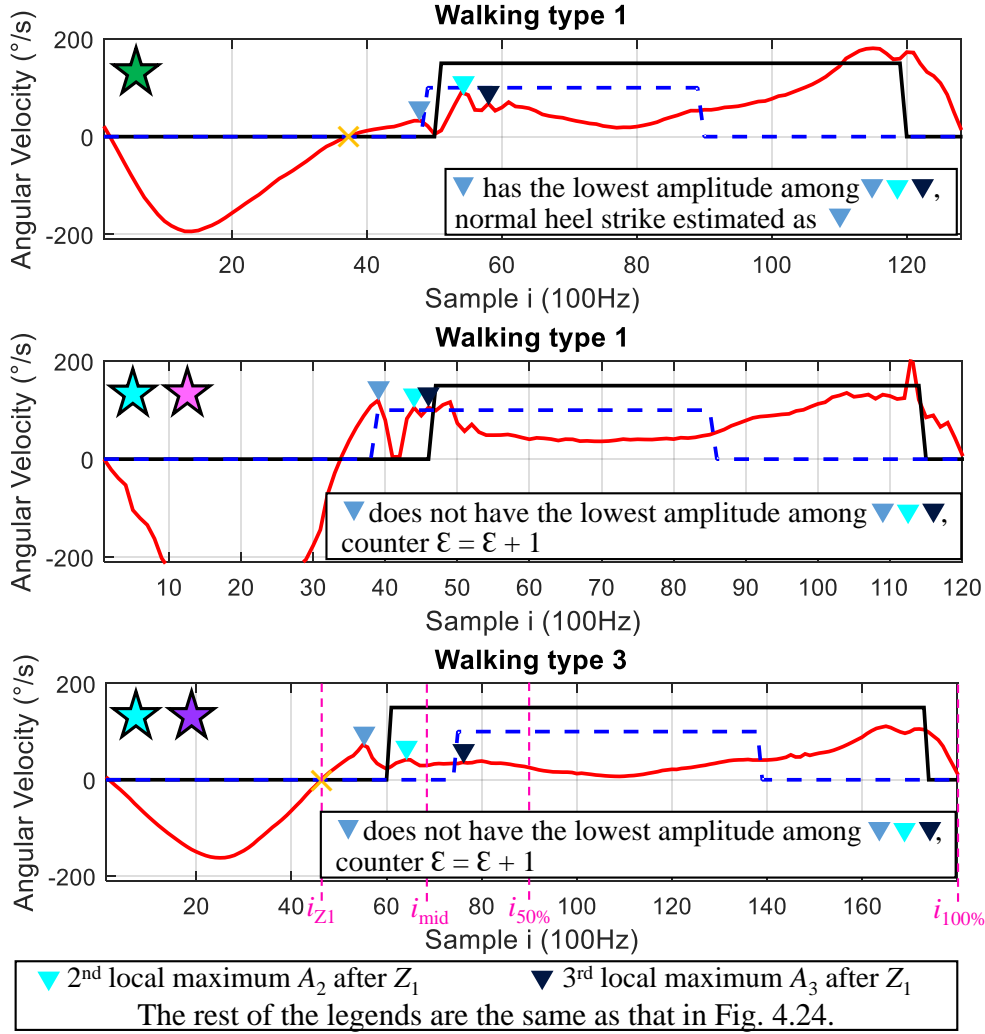


Fig. 4.25: ω_{shank} without 2nd positive zero crossing.

A counter ε is incremented by 1 whenever a heel strike is to be decided later. Counter ε is also incremented by 1 every time an abnormal heel strike is detected. After processing all gait cycles, by majority voting concept, if counter ε is greater than half of the total number of collected gait cycles, the heel strikes that are yet to be decided are now estimated using the midpoint i_{mid} between the first positive zero crossing i_{z1} and 50% of the extracted gait cycle $i_{50\%}$ (See Fig. 4.25 3rd gait cycle). i_{mid} can be calculated using (4.36) where i denotes the i^{th} sample.

$$i_{\text{mid}} = i_{z1} + \left(\frac{i_{z1} + i_{50\%}}{2} \right) \quad (4.36)$$

If ε is smaller than half of the total number of collected gait cycles, the heel strikes that are yet to be detected are now detected using i_{A1} .

Fig. 4.26 summarizes the observations for heel strike detection and diagnosis discussed in this section.

Run this first for all gait cycles collected from a subject: Before 50% of the extracted gait cycle ($i_{50\%}$),	
If Z_2 exists,	
<p>If Z_n and Z_2 are separated by more than 5 samples (50ms),</p> <ul style="list-style-type: none"> ➤ Abnormal heel strike ★ ➤ $i_{HS} = i_{An}$ ➤ counter $\mathcal{E} = \mathcal{E} + 1$ 	
<p>Else if A_n occurs within $A_1 \pm 5$ samples,</p> <ul style="list-style-type: none"> ➤ Normal heel strike ★ ➤ $i_{HS} = i_{An} \approx i_{A1}$ 	
<p>Else</p> <ul style="list-style-type: none"> ➤ Abnormal heel strike ★ ➤ $i_{HS} = i_{An}$ ➤ counter $\mathcal{E} = \mathcal{E} + 1$ 	
Else	
<p>If A_1 has the lowest amplitude among A_1, A_2 and A_3,</p> <ul style="list-style-type: none"> ➤ Normal heel strike ★ ➤ $i_{HS} = i_{A1}$ 	
<p>Else</p> <ul style="list-style-type: none"> ➤ Normal/Abnormal estimates later. ★ ➤ i_{HS} estimates later. ➤ counter $\mathcal{E} = \mathcal{E} + 1$ 	
After processing all gait cycles using the method above, run this for the gait cycles that have not been estimated yet:	
<p>If $\mathcal{E} > (\text{total number of gait cycles}) \times 0.5$</p> <ul style="list-style-type: none"> ➤ Abnormal heel strike ★ ➤ $i_{HS} = i_{mid}$ 	
<p>Else</p> <ul style="list-style-type: none"> ➤ Normal heel strike ★ ➤ $i_{HS} = i_{A1}$ 	
<p>i_{HS} denotes the time when the heel strikes. The rest of the legends are the same as that in Fig. 4.24.</p>	

Fig. 4.26: Proposed method to detect and diagnose heel strikes.

4.4.3.5 Toe Strike

As shown in Fig. 4.27, normal toe strikes (walking type 1) can be estimated using the first local maximum of low pass filtered ω_{shank} . Abnormal toe strikes (walking types 2, 3 and 4) can be detected using the first local maximum of ω_{shank} .

$\bar{\omega}_{\text{shank}}$ denotes the low pass filtered ω_{shank} . The low pass filter used is a moving average as stated in (4.37). The size k used in this research was 10, obtained through trials and errors.

$$\bar{\omega}_i = \frac{1}{2k} \sum_{i=i-k}^{i+k} \omega_i \quad (4.37)$$

The detection of toe strike for walking type 3 can be achieved using the proposed method for heel strike detection. In order to distinguish normal/abnormal toe strikes for walking types 1, 2 and 4, some unique waveform patterns of normal/abnormal shank's angular velocity ω_{shank} , angle θ_{shank} , and acceleration are identified.

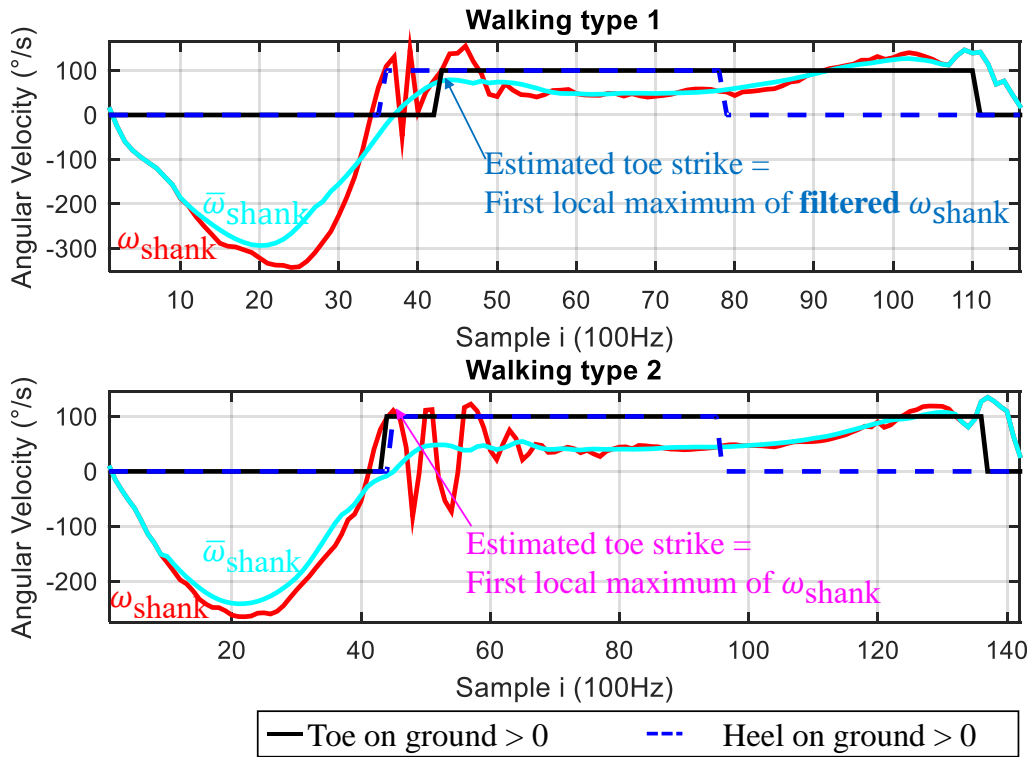


Fig. 4.27: Proposed method to detect normal toe strikes.

It is observed that ω_{shank} of normal toe strikes has less than 7 local maxima A from i_{z1} to $i_{50\%}$. Therefore, abnormal toe strikes can be identified when the total number of local maxima is equal than or greater than 7, as stated in (4.38). Fig. 4.28 shows an

example of ω_{shank} with total number of $A = 7$, fulfilling (4.38), which means the toe strike is abnormal.

$$\text{Total number of } A \geq 7 \text{ (abnormal toe strike)} \quad (4.38)$$

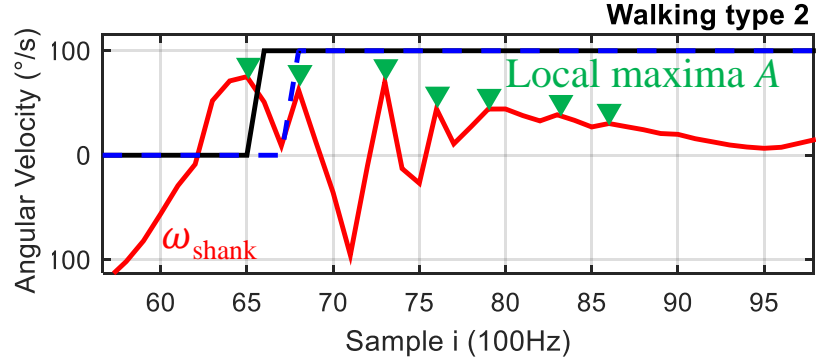


Fig. 4.28: Abnormal toe strike (Pattern 1).

Additionally, ω_{shank} of normal toe strikes does not have A_1 and A_2 being the lowest and highest amplitudes, respectively, and A_2 is still greater than A_3 even if A_3 is increased to 130%. In other words, abnormal toe strikes can be detected based on the conditions stated in (4.39). An example of abnormal toe strike that fulfill (4.39) is shown in Fig. 4.29.

$$\begin{aligned} A_1 < A_2 \text{ AND } A_1 < A_3, \text{ AND} \\ A_2 > A_1 \text{ AND } A_2 > A_3, \text{ AND} \\ A_2 > 1.3A_3 \end{aligned} \quad (4.39)$$

(abnormal toe strike)

Where A_1 , A_2 , and A_3 are the 1st, 2nd, and 3rd local maxima of ω_{shank} , respectively.

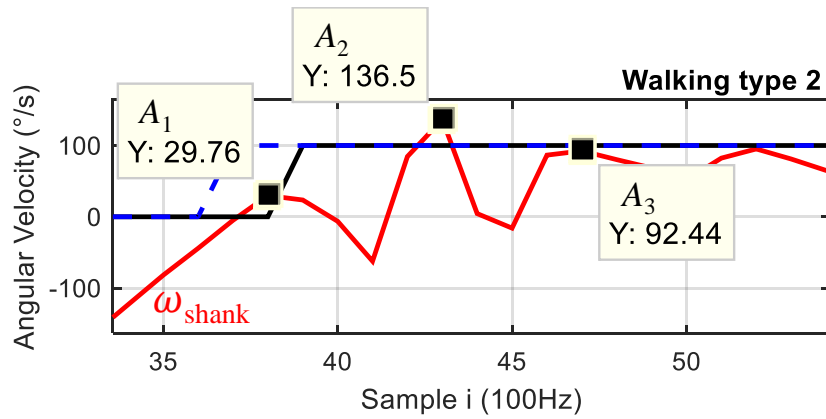


Fig. 4.29: Abnormal toe strike (Pattern 2).

It is noticed that the lowest local minima M_{min} for normal toe strikes must be the

1st, 2nd or 3rd local minima M of ω_{shank} . Abnormal toe strikes can be detected when M_{min} is not among the first three local minima M_1, M_2 and M_3 , as stated in (4.40). Fig. 4.30 shows that the lowest local minima $M_{\text{min}} = M_4$, which fulfills (4.40), signifying the toe strike is abnormal.

$$M_{\text{min}} \neq M_j \text{ for } j = 1, 2, 3 \text{ (abnormal toe strike)} \quad (4.40)$$

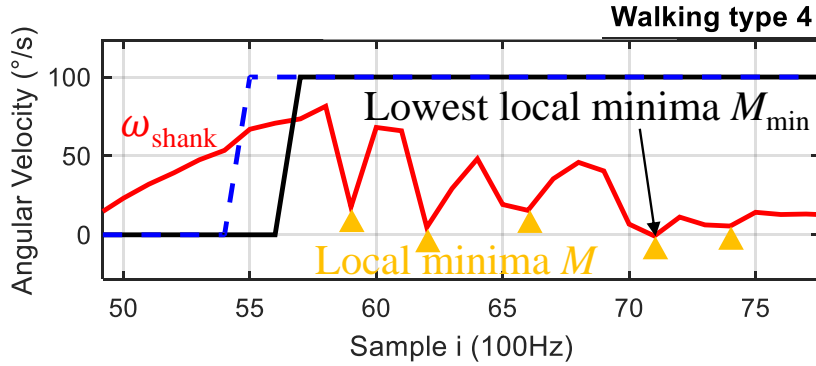


Fig. 4.30: Abnormal toe strike (Pattern 3).

For normal toe strikes, the highest local maxima A_{max} is higher than the absolute value of the lowest local minima A_{min} . Abnormal toe strikes can be detected when (4.41) is fulfilled. Fig. 4.31 shows an abnormal toe strike with $|A_{\text{min}}| = 149.8 > |A_{\text{max}}| = 140$.

$$|A_{\text{min}}| > |A_{\text{max}}| \text{ (abnormal toe strike)} \quad (4.41)$$

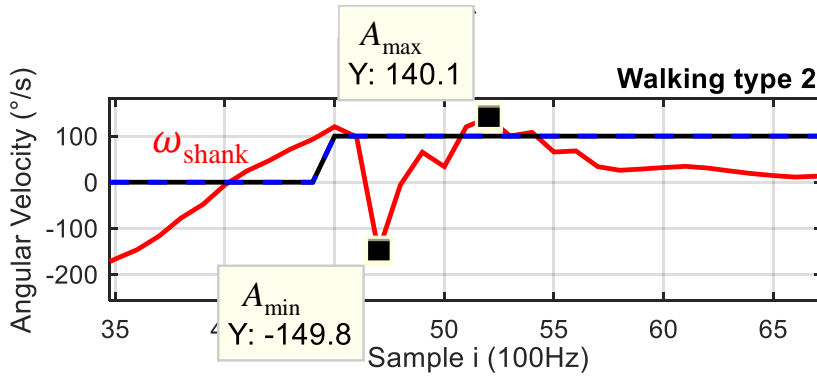


Fig. 4.31: Abnormal toe strike (Pattern 4).

For normal toe strikes, the highest local maxima A_{max} is higher than the second highest local maxima $A_{\text{max}2}$ by less than 2 times. In other words, $A_{\text{max}2}$ is lower than half of A_{max} for abnormal toe strikes, as stated in (4.42). Abnormal toe strikes can be detected when (4.42) is fulfilled. Fig. 4.32 shows that $0.5A_{\text{max}}$ is higher than $A_{\text{max}2}$,

which signifies abnormal toe strike.

$$0.5A_{\max} > A_{\max2} \text{ (abnormal toe strike)} \quad (4.42)$$

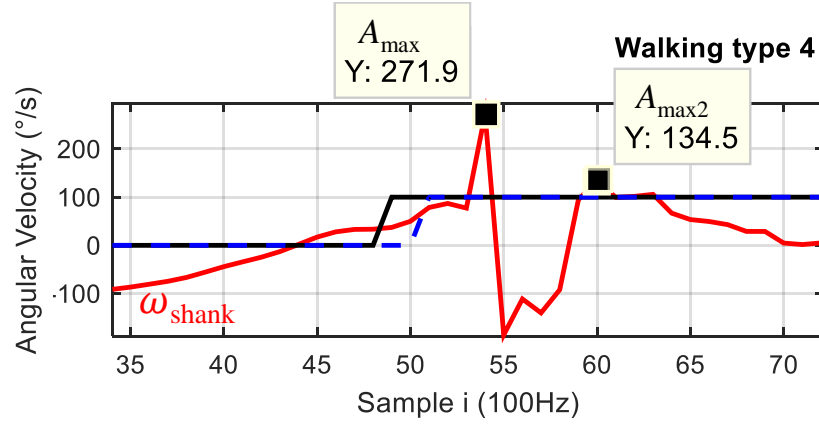


Fig. 4.32: Abnormal toe strike (Pattern 5).

For normal toe strikes, the highest local maxima \bar{A}_{\max} of $\bar{\omega}_{\text{shank}}$ is higher than 40% of the highest local maxima A_{\max} of ω_{shank} . Therefore, abnormal toe strikes can be detected if the ratio of \bar{A}_{\max} to A_{\max} is less than 0.4 (4.43). Fig. 4.33 shows the ratio is $0.33 < 0.4$, signifying an abnormal toe strike.

$$\frac{\bar{A}_{\max}}{A_{\max}} < 0.4 \text{ (abnormal toe strike)} \quad (4.43)$$

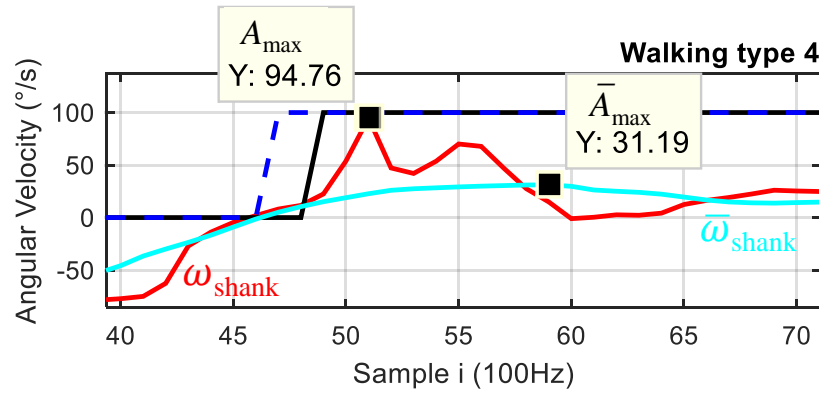


Fig. 4.33: Abnormal toe strike (Pattern 6).

The maximum angle P_{\max} of the shank angle $-\theta_{\text{shank}}$ should be the first local maximum P_1 for normal gaits. However, for some abnormal toe strikes as shown in Fig. 4.34, P_1 is not P_{\max} (4.44).

$$P_1 \neq P_{\max} \text{ (abnormal toe strike)} \quad (4.44)$$

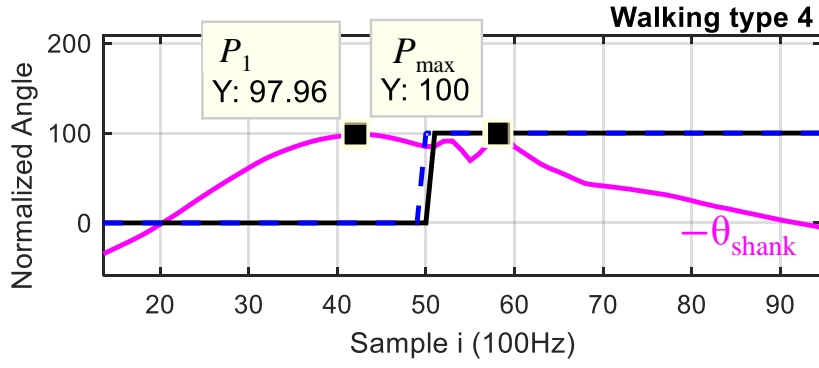


Fig. 4.34: Abnormal toe strike (Pattern 7).

As shown in the first gait cycle in Fig. 4.35, the gradient V of the measured vertical acceleration and gradient H of the measured horizontal acceleration of normal gaits are mostly of the same sign (see pink lines) within the first zero crossing of ω_{shank} to half of the gait cycle. However, for some abnormal toe strikes, as shown in the second gait cycle in Fig. 4.35, the gradient signs of the accelerations are mostly opposite to each other. Therefore, abnormal toe strikes can be identified when (4.45) is fulfilled.

$$\sum_{j=i_{z1}}^{i_{50\%}} [\text{sign}(V_j) \times \text{sign}(H_j)] < 0 \text{ (abnormal toe strike)} \quad (4.45)$$

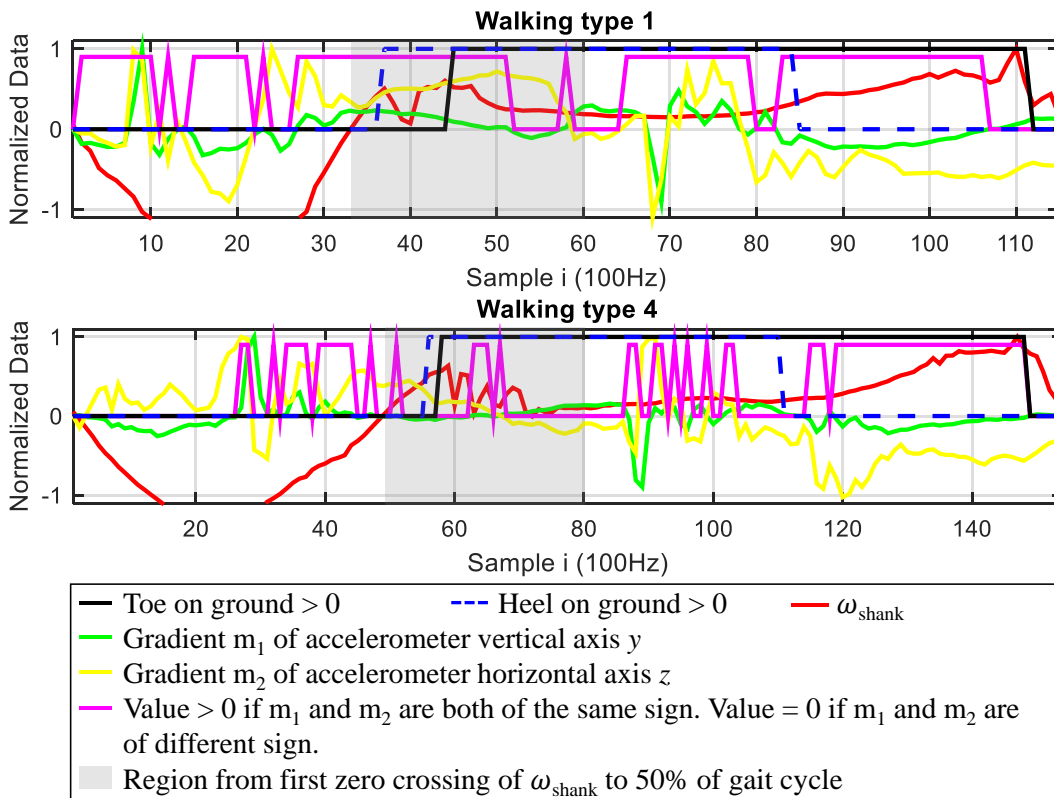


Fig. 4.35: Abnormal toe strike (Pattern 8).

In cases where none of the conditions in (4.38) – (4.45) is fulfilled, a counter \mathcal{E} is incremented by 1. After processing all gait cycles, if counter \mathcal{E} is greater than 0.7 times the total number of collected gait cycles, the toe strikes that are yet to be decided are now estimated as normal. The toe strikes are estimated as abnormal when \mathcal{E} is lower than 0.7 times the total number of collected gait cycles. Fig. 4.36 summarizes the observations for toe strike detection and diagnosis discussed in this section.

Run this first for all gait cycles collected from a subject:	
If any one of the equations in (eq. 4.38 – 4.45) is fulfilled,	
➤	Abnormal toe strike
➤	$i_{TS} = i_{A1}$
Else	
➤	Normal/Abnormal estimates later.
➤	i_{TS} estimates later.
➤	counter $\mathcal{E} = \mathcal{E} + 1$
After processing all gait cycles using the method above, run this for the gait cycles that have not been estimated yet:	
If $\mathcal{E} > (\text{total number of gait cycles}) \times 0.7$	
➤	Normal toe strike
➤	$i_{TS} = i_{\bar{A}1}$
Else	
➤	Abnormal toe strike
➤	$i_{TS} = i_{A1}$
i denotes i^{th} sample.	
TS denotes toe strike.	
A_1 denotes the first local maximum of ω_{shank} .	
\bar{A}_1 denotes the first local maximum of filtered ω_{shank} (eq. 4.37).	

Fig. 4.36: Proposed method to detect and diagnose toe strikes.

4.4.3.6 Toe Off

As shown in Fig. 4.37, normal toe off can be detected using the last local maximum A_{last} of ω_{shank} in a gait cycle. To improve the toe off detection (an improvement of average 0.2 to 0.5 sample difference), the toe off is estimated by adding 2 samples if the separation between A_{last} and the second last local maximum $A_{\text{last}2}$ is more than 10 samples, as stated in (4.46).

$$\begin{aligned}
 &\text{if } (i_{A_{\text{last}}} - i_{A_{\text{last}2}} > 10) && i_{TO} = i_{A_{\text{last}}} + 2 \\
 &\text{else} && i_{TO} = i_{A_{\text{last}}}
 \end{aligned} \tag{4.46}$$

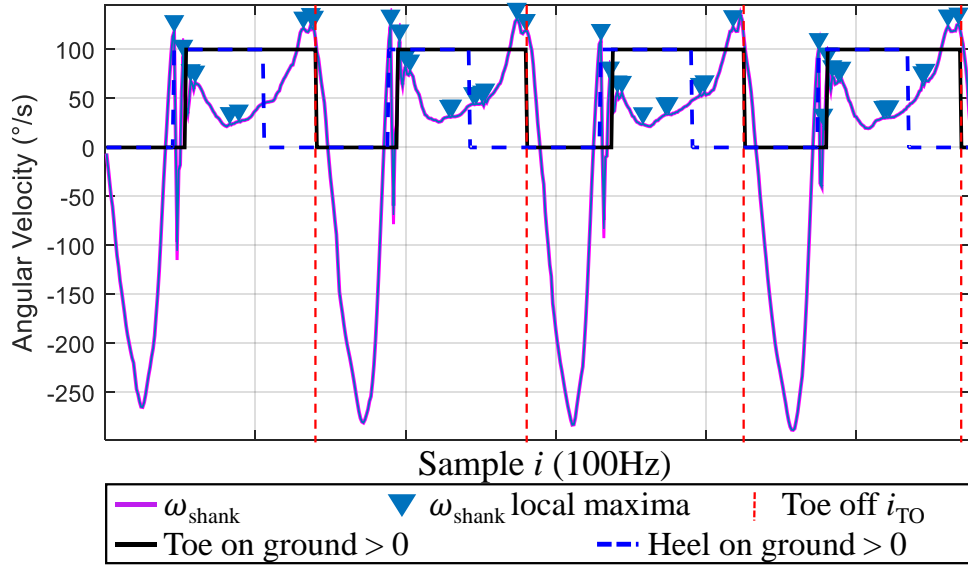


Fig. 4.37: Proposed method to detect toe off using last local maximum of ω_{shank} .

4.4.4 Results and Discussion

Some unique waveform patterns of shank's angular velocity and acceleration for normal/abnormal gaits are identified to distinguish them from one another. In contrast to other researchers [45] [106] who classified the whole gait pattern as normal or abnormal, the proposed method classifies normal or abnormal heel strike and toe strike. As stated in Table 4.19, the mean accuracy of classifying heel strike and toe strike as normal/abnormal is 94.4%.

Table 4.19: Mean Accuracy (%) of Gait Diagnosis using Proposed Method.

Type of Walking	Heel Strike	Toe Strike
1	90.35 (Normal)	93.30 (Normal)
2	95.97 (Normal)	92.93 (Abnormal)
3	93.75 (Abnormal)	93.75 (Abnormal)
4	97.12 (Normal)	100.00 (Abnormal)
Overall	94.43	94.47

Fig. 4.38 illustrates the sample difference between proposed method and Senanayake *et al.* [9]. Comparing the proposed method with [9], the detected gait sub-phases (heel strike, toe strike and toe off) have low mean absolute difference of about 2 sample difference, as stated in Table 4.20. As the sampling time of all sensors is

synchronized at 100Hz, 2 sample difference is equivalent to 20ms. This means the proposed method is reliable in gait phase detection.

The difference between the proposed method and [9] is that [9] used 4 FSRs (kinetic parameters) to detect the gait phases, while the proposed method used a single shank's IMU (kinematic parameters).

As the proposed method and Maqbool *et al.* [50] both detect the gait phases using local maxima/minima of shank's angular velocity, the method in [50] is also evaluated. As shown in Tables 4.20 and 4.21, the heel strike and toe off detected using [50] have higher errors for abnormal gait patterns. This is because [50] considered only normal gait patterns. The proposed method, on the other hand, can be said as an improvement of the method in [50] as abnormal gait patterns are considered in the gait phase detection.

Fig. 4.39 shows the gait sub-phases for the 4 types of walking analyzed in this research. As abnormal gait is subjected to missing phases of a gait cycle [107], LR and MSt in walking types 2 and 4 are not distinguishable.

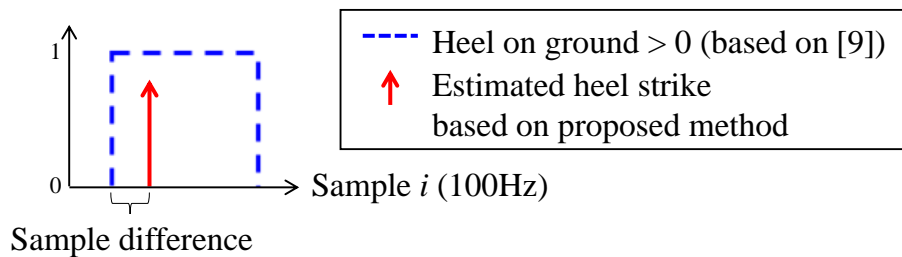


Fig. 4.38: Illustration of sample difference between proposed method and FSRs [9].

Table 4.20: Gait Phase Detection Error (in Sample Difference) when compared with FSRs [9].

Type of Walking	Detection Error (sample difference)				
	Heel Strike		Toe Strike	Toe Off	
	Proposed	Maqbool <i>et al.</i> [50]	Proposed	Proposed	Maqbool <i>et al.</i> [50]
1	1.26 (Normal)	1.17 (Normal)	2.63 (Normal)	1.63 (Normal)	2.15 (Normal)
2	1.06 (Normal)	1.67 (Normal)	2.33 (Abnormal)	1.82 (Normal)	5.17 (Normal)
3	4.92 (Abnormal)	11.41 (Abnormal)	2.34 (Abnormal)	1.92 (Normal)	6.42 (Abnormal)
4	1.48 (Normal)	1.65 (Normal)	1.77 (Abnormal)	2.13 (Normal)	4.56 (Abnormal)
Average	2.11	3.75	2.00	1.92	4.74

Table 4.21: Gait Phase Detection Error (ms) when compared with FSRs [9].

Type of Walking	Detection Error (ms)				
	Heel Strike		Toe Strike	Toe Off	
	Proposed	Maqbool <i>et al.</i> [50]	Proposed	Proposed	Maqbool <i>et al.</i> [50]
1	12.6 (Normal)	11.7 (Normal)	26.3 (Normal)	16.3 (Normal)	21.5 (Normal)
2	10.6 (Normal)	16.7 (Normal)	23.3 (Abnormal)	18.2 (Normal)	51.7 (Normal)
3	49.2 (Abnormal)	114.1 (Abnormal)	23.4 (Abnormal)	19.2 (Normal)	64.2 (Abnormal)
4	14.8 (Normal)	16.5 (Normal)	17.7 (Abnormal)	21.3 (Normal)	45.6 (Abnormal)
Average	21.1	37.5	20.0	19.2	47.4

Type of Walking	Gait Sub-Phases			
1	← LR → Heel strike	← MSt → Toe strike	← TSt → Heel off	Swing → Toe off
2	← LR → Heel strike Toe strike		← TSt → Heel off	Swing → Toe off
3	← LR → Toe strike	← MSt → Heel strike Toe strike	← TSt → Heel off	Swing → Toe off
4	← LR → Heel strike Toe strike		← TSt → Heel off	Swing → Toe off

Fig. 4.39: Gait sub-phases for different types for walking.

As shown in Fig. 4.40, the proposed method is accurate in identifying the gait sub-phases. For example, the proposed method has successfully detected the toe strike occurs earlier than heel strike in walking type 3 (abnormal). Referring to the walking types 2 and 4 in Fig. 4.40, the heel and toe strikes are considered occurring at the same time if the heel and toe strikes are detected within ± 2 samples.

As the proposed method is not able to detect heel off using the shank's angular velocity, MSt and TSt cannot be differentiated. Additionally, MSw has been well researched by identifying the maximum angle of the shank [8], therefore MSw is not covered in this chapter. MSw has actually been detected in Fig. 4.20.

Other than that, abnormal gaits such as 'walk with toe', do not have heel strike and heel off. 'Walk with heel', on the other hand, do not have toe strike and toe off. The proposed method can only identify the 4 types of gait patterns as stated in Table 4.15, but not able to identify 'walk with toe' and 'walk with heel'. Despite having these limitations, the proposed method which uses only a single shank's IMU has been validated against the existing method which uses 4 FSRs [9], and is an improvement of [50].

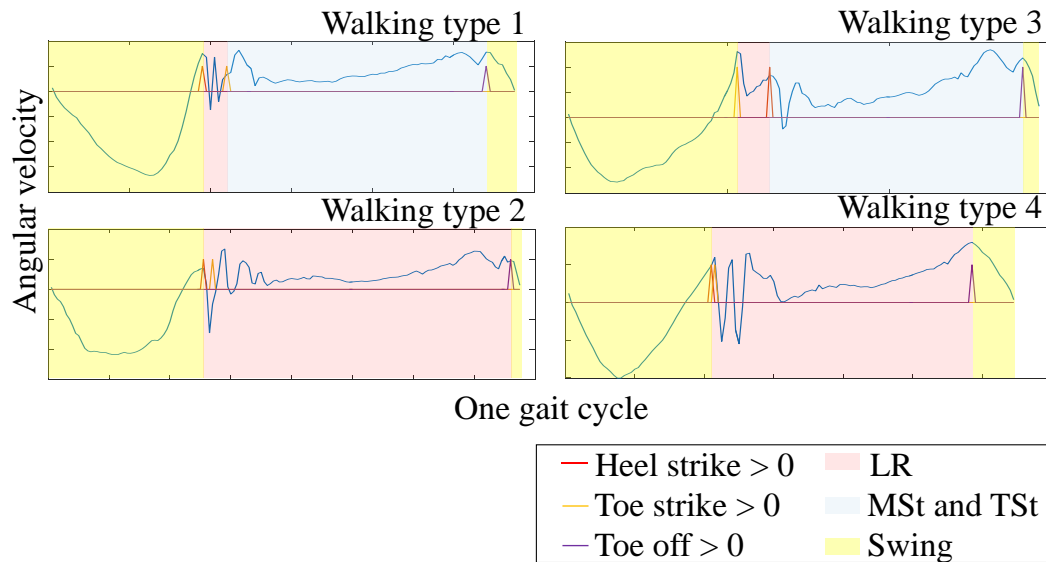


Fig. 4.40: Detected gait sub-phases based on proposed method.

It is also worthwhile to compare the performance of the proposed method with other relevant papers. As listed in Table 4.22, several efforts have been conducted for gait phase detection using sensors such as IMUs [7] [8] [12] [13], FSRs [9] [12], optical systems [10] [11], and electromyography [108] [109]. The mean accuracy of the proposed method is 94.4% while other methods [7] [11] [12] [108] [109] reported higher mean accuracy of over 97%. The proposed method has lower mean classification accuracy, but lower mean error of 20ms than [12] and [109].

The proposed method utilizes simple comparators which does not involve complex calculations. Although some heel and toe strikes can be detected in almost real-time (<40ms) using the proposed method, there are cases where some heel and toe strikes can only be detected after processing all gait cycles (See Fig. 4.26 and 4.36). The proposed method is more suitable for applications that does not require real-time detection, such as gait assessment.

Table 4.22: Comparison of Gait Phase Detection Methods among Literatures.

Reference	Method	Sensor	Mean accuracy (%)	Mean error (ms)	Consider abnormal gait?
[7]	Bayesian formulation	3 IMUs	99	-	Yes
[8]	Local maxima and minima	2 IMUs	-	20	No
[9]	Fuzzy logic	4 FSRs	-	13	Yes
[10]	Fuzzy logic	Optical	-	-	No
[11]	Machine learning	Optical	97	-	No
[12]	Rule-based	3 FSRs, 1 IMU	99	< 90	Yes
[13]	Dynamic threshold	1 IMU	-	-	No
[108]	Support vector machine	EMG, GRF	97	-	Yes
[109]	Adaptive neuro-fuzzy inference system	EMG	97	30	Yes
Proposed method	Rule-based local maxima and minima	1 IMU	94	20	Yes

The dash ‘-’ means not reported. EMG stands for electromyography. GRF stand for ground reaction force.

4.4.5 Summary

A method to detect normal and abnormal heel strike, toe strike, and toe off using a single IMU attached to the shank was proposed and validated against an existing method that placed FSRs under the foot. The MAE of the heel strike, toe strike and toe off detections was low at around 2 sample difference, equivalent to 20ms difference. Instead of classifying the whole stride, some unique waveform patterns of the normal/abnormal shank’s angular velocity were identified to classify the heel strike and toe strike as normal/abnormal. This may provide insights into the shank’s angular velocity waveform patterns that are human-understandable to assist clinicians to evaluate the gaits. The accuracy of the proposed method was high at about 94.4%.

4.5 Accurate Gait Modelling based on Waveform Scaling before DFT

4.5.1 Introduction

Gait modelling is essential for many applications including animation, activity recognition, medical diagnosis, and robotics. Many researchers have worked on mathematically express the movement of human bodies. At current stage, the reconstructed waveforms from the mathematical expressions either represent smoothed waveforms, fluctuate (noisy) along the original waveforms, or require high number of computations. In this chapter, a method to mathematically express normal and abnormal shank and thigh angle waveforms without smoothing and fluctuations is proposed. The angle waveforms are time and amplitude scaled before performing DFT. By doing so, the CORR between the original and reconstructed waveforms can be improved without increasing the number of harmonics. The shank's angular velocity is also recalculated from the reconstructed shank's angle waveform for gait phase detection, and shows accurate results in heel and toe strikes estimation when compared to the original shank's angular velocity. Additionally, the harmonic components of the waveforms are used for gait recognition, and shows the potential of proposed method in improving the classification accuracy.

The contents in Chapter 4.5 has been submitted for review for possible publication. Once published, the publication can be searched as:

Y. C. Han, K. I. Wong and I. Murray, "Gait Phase Detection for Normal and Abnormal Gaits Using IMU".

4.5.2 Experimental Setup

The placement of IMUs is the same as Fig. 4.9(a), where the IMUs were strapped in front of the right thigh and shank using Velcro straps. In this chapter, the direction of the angle is represented in Fig. 4.41, which is opposite to Fig. 4.9.

20 healthy adults (male: 13; female: 7; age: 21-35; height: 151-182cm) were participated in the data collection. Each person was asked to walk at their own pace on a flat surface 3 times for 4-5 steps each trial (walking pattern 1). A total of 263 walking steps was collected.

Additionally, 3 types of simulated abnormal walking patterns in Chapter 4.3 is used to evaluate how well the proposed method generalizes to movement variability. In this Chapter 4.5, the abnormal walking pattern when the volunteers swung their right leg

outwards while walking to simulate foot drop is labelled as walking pattern 2. Walking pattern 3 is when the volunteers walked with bandaged knee to simulate knee problem. Walking pattern 4 is when the volunteers wore a left slipper to simulate leg length discrepancy.

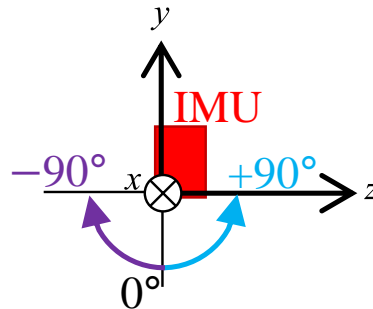


Fig. 4.41: Angle direction.

4.5.3 Proposed Method

4.5.3.1 Gait Cycle Extraction

Fig. 4.42 shows a shank angle waveform estimated using the method proposed in Chapter 4.2 which had been validated against gold standard Vicon optical motion capture system. The same sensors, microcontrollers, and sampling period (100Hz) were used. As shown in Fig. 4.42, the gait cycles were extracted using the maximum backward swings of the shank. The gait cycles were extracted in such a way that it starts with a maximum backward swing of the shank, and ends with a subsequent maximum backward swing of the same shank.

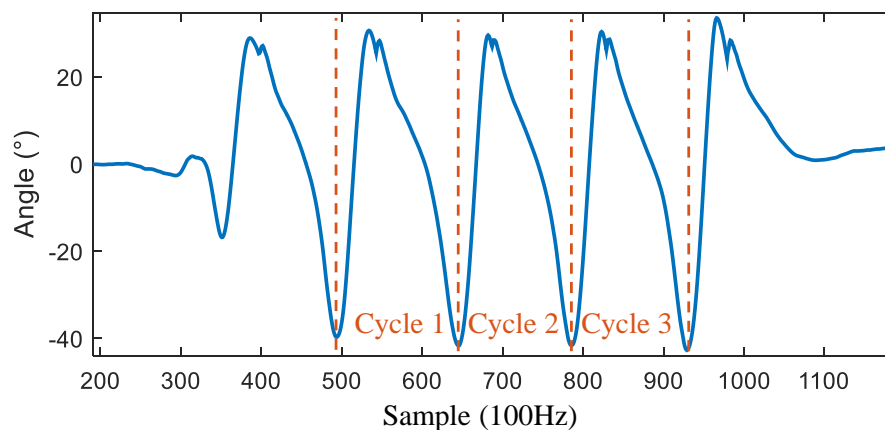


Fig. 4.42: Gait cycle extraction using maximum backward swings of shank.

4.5.3.2 Waveform Transformation before DFT

Fig. 4.43 shows the flowchart to time and amplitude scale the original waveforms before performing DFT, so that the required number of harmonics can be reduced while maintaining the accuracy.

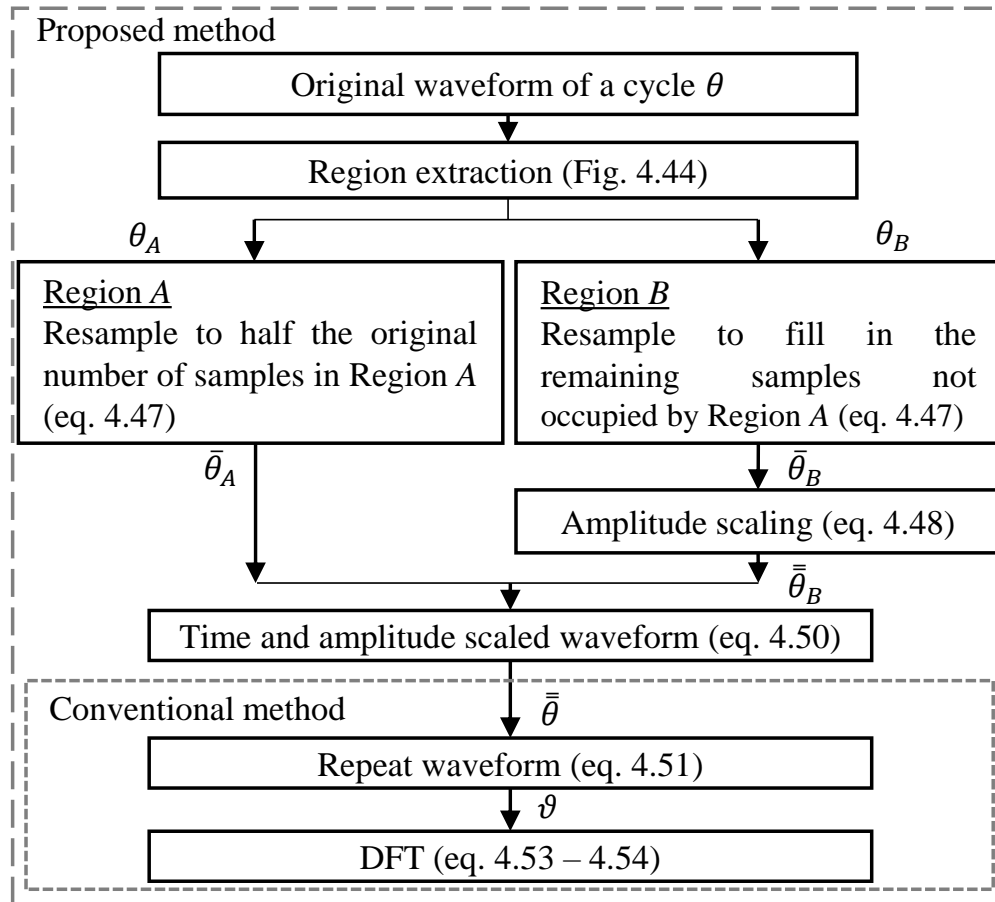


Fig. 4.43: Flowchart for waveform transformation before performing DFT.

As shown in Fig. 4.44, the angle waveform can be divided into 2 regions: smooth and less-smooth regions. The smooth region (Region *A*) is defined as the region where the angles are below a threshold $\lambda\%$ of the peak-to-peak angle. The less-smooth region (Region *B*) consists of more fluctuations and is defined as the region of the waveform above $\lambda\%$ of the peak-to-peak angle. Region *B* can also be called as the region-of-interest for some applications such as gait phase detection as it is where maximum swing, heel strike, and toe strike occur [8] [50] [66].

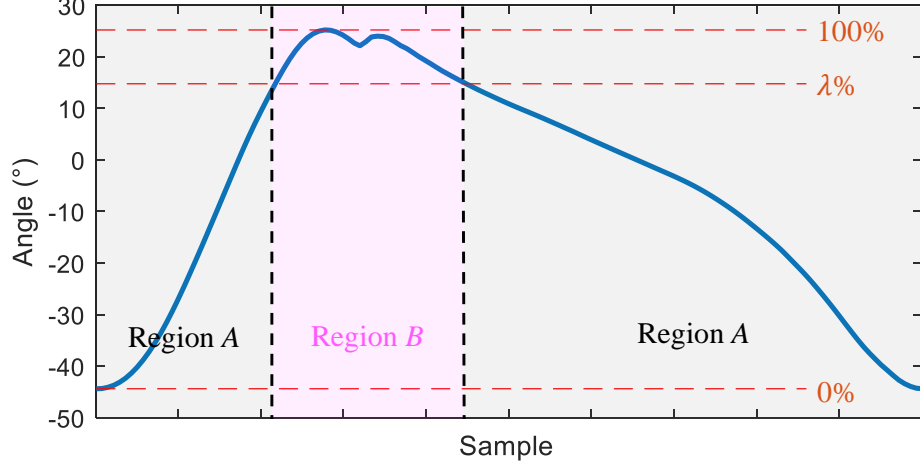


Fig. 4.44: Region extraction for one cycle of an angle waveform.

After the regions are extracted, Region *A* is resampled to half of its original number of samples because Region *A* consists of a smoother curve compared to Region *B*, therefore down-sampling Region *A* will not reduce much of the CORR. Then, Region *B* is resampled (time stretched) to fill in the remaining samples not occupied by Region *A*, as shown in Fig. 4.45. By doing so, the total number of samples of the resampled waveforms remain the same as the original waveform, and the non-smooth region can be “zoomed in” before performing DFT.

As a side note, Region *A* could also be resampled to 1/3 or 1/4 of its original number of samples so that Region *B* could be further enlarged, but in this research Region *A* is just resampled to half of its original number of samples to demonstrate the practicality of the proposed method. The resampling method in (4.47) can be used to resample the waveforms such that the original waveform with I number of samples is resampled to \bar{I} number of samples.

$$\bar{\theta}_j = \theta_{\lceil i \rceil} (i - \lceil i \rceil + 1) - \theta_{\lfloor i \rfloor} (i - \lfloor i \rfloor) \quad (4.47)$$

$$\text{for } \begin{cases} i = 1, 1 + \frac{I-1}{\bar{I}-1}, 1 + 2\frac{I-1}{\bar{I}-1}, \dots, I \\ j = 1, 2, 3, \dots, \bar{I} \end{cases}$$

Where θ is the original waveform. $\bar{\theta}$ is the resampled waveform. $\lceil \cdot \rceil$ and $\lfloor \cdot \rfloor$ denote the ceiling and flooring functions, respectively.

However, the resampled/time-scaled waveform $\bar{\theta}$ (blue line in Fig. 4.45) has abrupt change of gradient at the connection point between Regions *A* and *B*. This can reduce the CORR between the original and reconstructed waveforms. To connect both regions smoothly, the amplitudes of resampled Region *B* $\bar{\theta}_B$ are multiplied with the

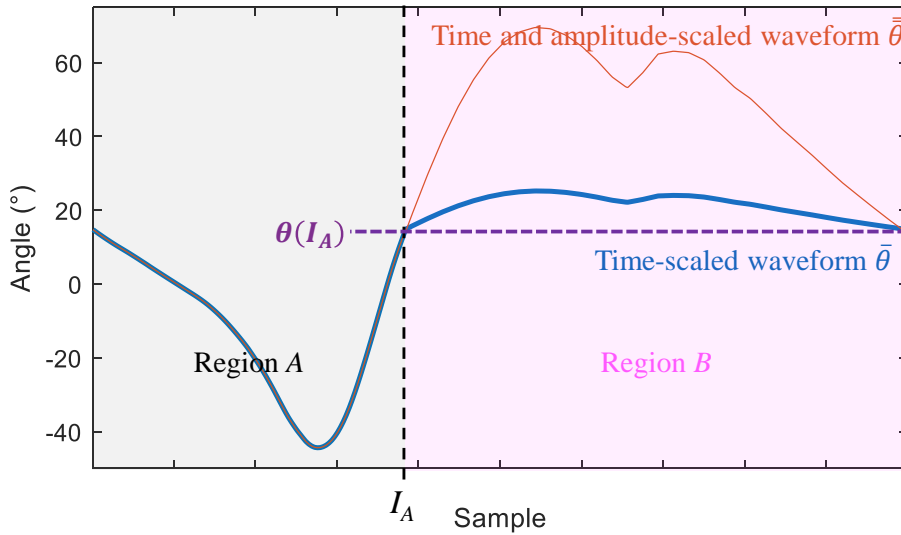
ratio m of the final gradient of resampled Region A $\bar{\theta}_A$ to the initial gradient of $\bar{\theta}_B$, as stated in (4.48) and (4.49). $\bar{\theta}_A$ remains unchanged. The time and amplitude-scaled waveform $\bar{\theta}$ (4.50) is shown with the red line in Fig. 4.45.

$$\bar{\theta}_B(i) = \bar{\theta}_B(i) \times m - \bar{\theta}_B(1) + \theta(I_A) \quad (4.48)$$

$$m = \left| \frac{\bar{\theta}(I_A) - \bar{\theta}(I_A - 1)}{\bar{\theta}(I_A + 2) - \bar{\theta}(I_A + 1)} \right| \quad (4.49)$$

$$\bar{\theta} = [\bar{\theta}_A \quad \bar{\theta}_B] \quad (4.50)$$

Where $\bar{\theta}_B$ denotes the time and amplitude-scaled waveform of Region B, $\bar{\theta}_B(1)$ denotes the first sample of $\bar{\theta}_B$, I_A denotes the last sample of the resampled angle in Region A. $\theta(I_A)$ denotes the amplitude of the last angle of Region A.



Remark: I_A and $\theta(I_A)$ are stored for waveform reconstruction.

- Region extraction of the time and amplitude-scaled waveform is achieved by finding the angle which is the closest to $\theta(I_A)$.
- The original length of Region A is $I_A/2$, while the original length of Region B is $1 - I_A/2$.

Fig. 4.45: Time and amplitude-scaled waveforms.

The time and amplitude-scaled waveform $\bar{\theta}$ is then then repeated X times as shown in Fig. 4.46. In this research, X is selected to be 15 for the repeated waveform ϑ (4.51). The harmonics are more distinctive to be identified as X increases.

$$\vartheta = [\bar{\theta} \quad \bar{\theta} \quad \bar{\theta} \quad \dots \quad \bar{\theta}] \quad (4.51)$$

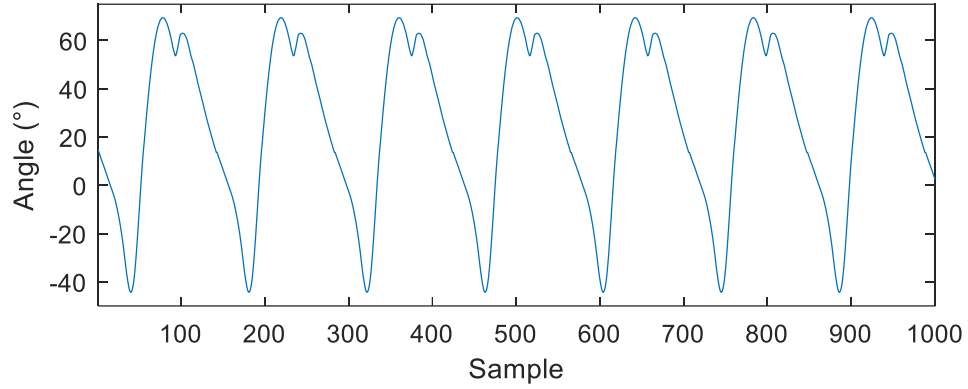


Fig. 4.46: Time and amplitude-scaled waveform repeated X times.

DFT in (4.52) is performed for the repeated waveform ϑ and resulted in Fig. 4.47. The DFT of the scaled waveform at h^{th} harmonic can be expressed as (4.53).

$$DFT_j = \frac{2}{L} \sum_{i=1}^L \vartheta_i e^{-j2\pi(i-1)\frac{n-1}{L}} \quad \text{for } j = 1, 2, \dots, \frac{L}{2} \quad (4.52)$$

$$DFT_h = \frac{2}{L} \sum_{i=1}^L \vartheta_i e^{-j2\pi(i-1)\frac{h}{T}} \quad \text{for } h = 1, 2, \dots, H \quad (4.53)$$

Where the transform length is selected to be the same as the length $L \approx 1500$ of ϑ . e denotes the exponential function, and j is the imaginary number. H denotes the total number of harmonics. T is the number of samples of $\bar{\vartheta}$.

The instantaneous amplitude α_h and the phase φ_h of the h^{th} harmonic can be obtained by writing the DFT in polar form (4.54).

$$DFT_h = \alpha_h \angle \varphi_h \quad (4.54)$$

The DC component b of the time and amplitude-scaled waveform can be obtained by calculating the average value of the waveform within one period.

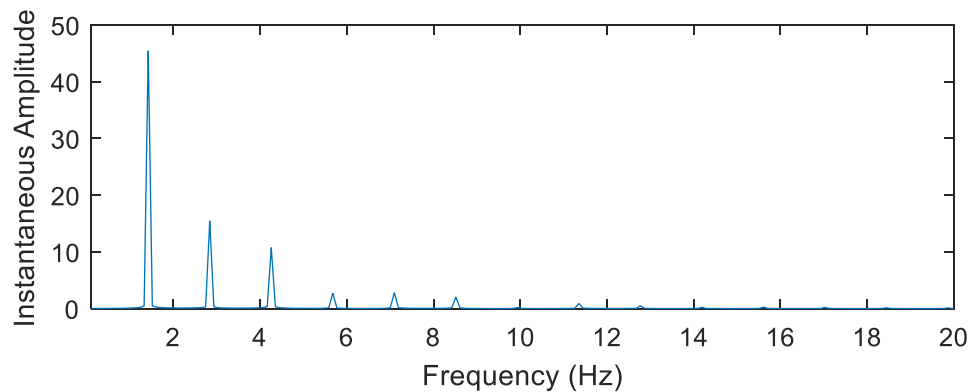


Fig. 4.47: Single-sided amplitude spectrums of a full cycle of scaled waveform.

4.5.3.3 Waveform Reconstruction

Fig. 4.48 shows the flowchart to reconstruct the angle waveform θ . The scaled waveform $\bar{\theta}$ can be reconstructed by inputting the instantaneous amplitudes α_h and phase φ_h of the h^{th} harmonics to Fourier series in (4.55).

$$\bar{\theta}(i) = b + \sum_{h=1}^H \alpha_h \cos(2\pi hi + \varphi_h) \quad (4.55)$$

Where b denotes the average value of the scaled waveform within one period.

Regions A and B are then extracted by finding the closest scaled angle $\bar{\theta}$ to $\theta(I_A)$. See the remark in Fig. 4.45.

The scaled angles of Region B $\bar{\theta}_B$ can be inverse-transformed back to its original amplitudes according to (4.56).

$$\bar{\theta}_B(i) = \frac{\bar{\theta}_B(i) - \bar{\theta}_B(1)}{m} + \theta(I_A) \quad (4.56)$$

Where m is stored from (4.49) for waveform reconstruction.

After that, both regions are resampled back to its original length. The original length of Region A is I_A , while the original length of Region B is $100 - I_A$.

The reconstructed waveform θ can be obtained by appending θ_B to θ_A (4.57).

$$\theta = [\theta_A \ \theta_B] \quad (4.57)$$

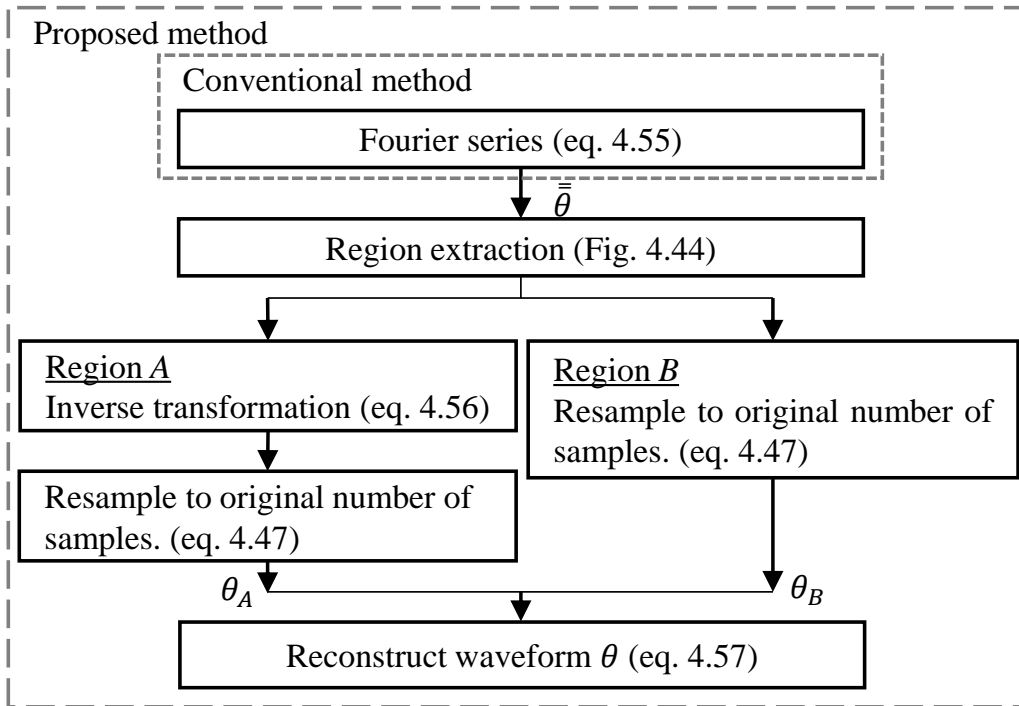


Fig. 4.48: Flowchart to reconstruct a waveform.

4.5.3.4 Possible Application 1: Gait Phase Detection

In Chapter 4.4, it was shown that the heel strike, toe strike and toe off can be estimated using the shank's angular velocity ω . As shown in Fig. 4.49, the normal heel strike can be estimated using the first local maximum of ω . The normal toe strike can be estimated using the first local maximum filtered angular velocity $\bar{\omega}$. The toe off can be estimated using the last local maximum of ω .

As angle θ can be estimated by integrating ω , ω can be re-obtained from θ according to (4.58), where T is the sampling period. The filtered angular velocity $\bar{\omega}$ can be obtained from (4.59), where k is set as 10 similar to Chapter 4.4.

$$\omega_i = \frac{\theta_i - \theta_{i-1}}{T} \quad (4.58)$$

$$\bar{\omega}_i = \frac{1}{2k} \sum_{i=i-k}^{i+k} \omega_i \quad (4.59)$$

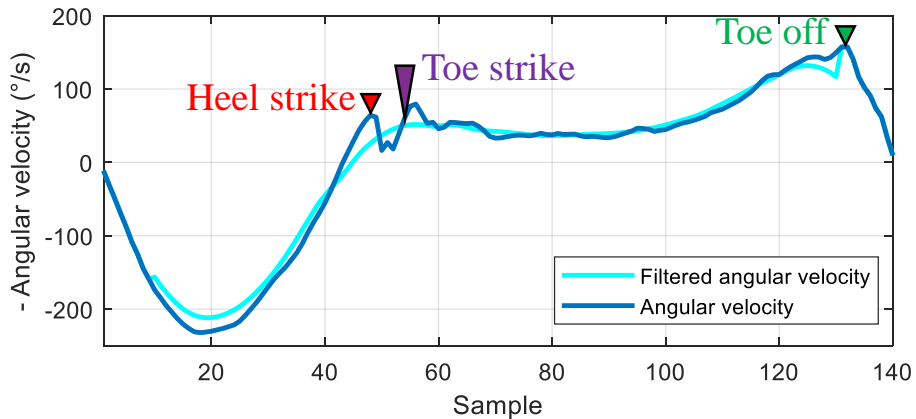


Fig. 4.49: Shank's angular velocity to detect gait phases.

4.5.3.4 Possible Application 2: Gait Classification

In [53], harmonic components of the ankle-knee, knee-hip and hip-ankle angle waveforms were used to classify normal/abnormal gaits. To investigate if the proposed method can be used to improve the multi-class classification accuracy, a simple fully connected neural network, as shown in Fig. 4.50, is utilized. 4 different types of gait patterns (1 normal, 3 abnormal) collected in Chapter 4.3.2 are to be classified. The input features are the instantaneous amplitudes α_h , phase φ_h and average value b of the shank and thigh angle waveforms when $H=10$. The initial weights and biases are random, and updated with backpropagation. The neural network is set to have 1 to 3 hidden layers with different numbers of neurons. The activation function used is a

hyperbolic tangent function. For balanced training dataset, 50 gait cycles from each pattern are used for training while the remaining gait cycles are used for testing. The training to validation ratio is 80:20%. For the proposed method, a pre-set threshold $\lambda = 0.55$ is used to extract distinct regions of the 4 different types of walking patterns.

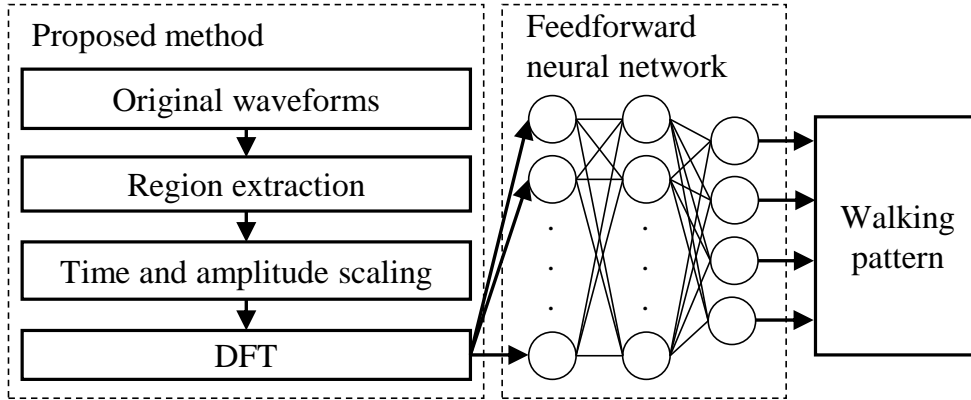


Fig. 4.50: Applying proposed method for gait classification.

4.5.4 Results and Discussion

The proposed method pre-scales the original waveforms before applying DFT. Conventional method in this paper means applying DFT without pre-scaling the waveforms. In [62] and [64], 6 harmonic components were used to predict the angle waveforms. In [66], 5 harmonic components were used. When checked with the experimental results, the overall (full cycle) CORR based on conventional method is indeed high above 99.9% when the number of harmonics $H=6$. However, as shown in Fig. 4.51, when checked specific regions (Region B) of the reconstructed waveforms, the CORR of the conventional method at Region B is low ($\ll 99.9\%$) when $H=6$. This indicates that 6 harmonics are insufficient to represent the angle waveforms accurately based on conventional method.

A good choice of threshold λ is crucial in maintaining a highly accurate mathematical representation of an angle waveform based on proposed method. The ideal value of λ should successfully extract the waveform in such a way that Region B consists of mainly the less-smooth region. As shown in Fig. 4.52, a low value of λ (< 0.5) will not help much in increasing the CORR because the extracted Region B consists of a big portion of smooth waveform. λ cannot be set too high as this will reduce the CORR because most of the less-smooth region is failed to be captured.

Referring to Fig. 4.52, λ for the proposed method are set as 0.85, 0.70, 0.55, and

0.75 for normal shank, normal thigh, abnormal shank, and abnormal thigh angle waveforms, respectively. This is because these λ values result in a high CORR and great improvement in CORR compared to conventional method, which means Region *B* averagely consists most of the less-smooth region of the waveforms at these thresholds.

Fig. 4.53 shows a plot of mean CORR against H . Considering the full cycle, the mean CORR of the proposed method (blue cross line) is lower than the conventional method (red cross line) when $H < 10$. However, when $H \geq 10$, the mean CORR of the full cycle for both conventional and proposed methods are about the same ($\geq 99.9\%$). Considering only the Region *B*, the proposed method (blue circled line) has higher mean CORR than conventional method (red circled line) when $H > 6$.

As listed in Table 4.23, the conventional method when $H \leq 6$ has low mean CORR at Region *B* $< 99.0\%$ and $< 99.4\%$ for normal and abnormal angle waveforms, respectively. The mean CORR at Region *B* improved to around 99.5% and 99.8% when $H = 10$. As a comparison, the proposed method when $H = 10$ has achieved a high mean CORR around 99.9% at Region *B*. It is only when $H > 15$, the conventional method achieves a high mean CORR above 99.9% at Region *B*, but the idea is to represent the waveforms accurately using lesser H .

As shown in Fig. 4.54, the reconstructed waveforms based on conventional method when $H \leq 10$ and proposed method when $H \leq 6$ represent smoothed original waveforms. The reconstructed waveforms based on proposed method when $H = 10$ represent the original waveforms more accurately than conventional method when $H = 15$ at Region *B*.

Comparing with existing methods, it can be seen from the figures provided in the existing literatures that the reconstructed waveforms based on the existing methods either represent smoothed waveforms [61] [62] [63] [64], or fluctuate along the original waveforms [59] [65].

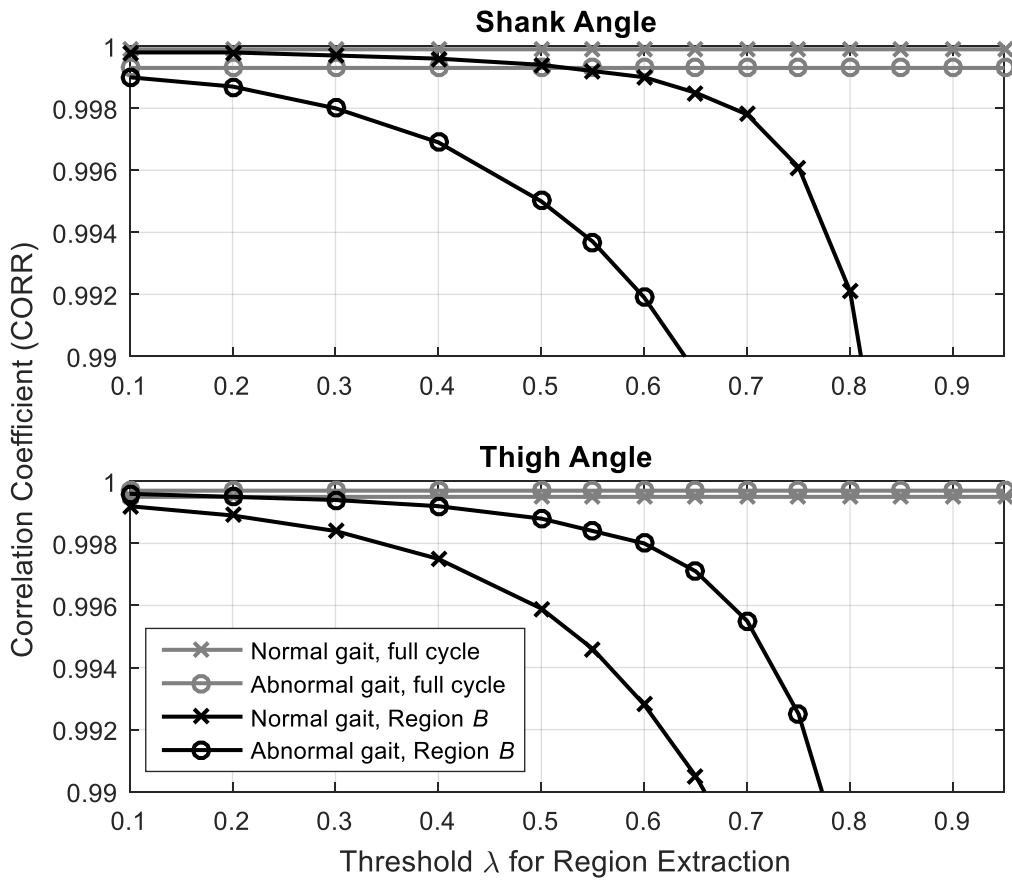


Fig. 4.51: Plot of mean CORR against thresholds λ for conventional method when $H=6$.

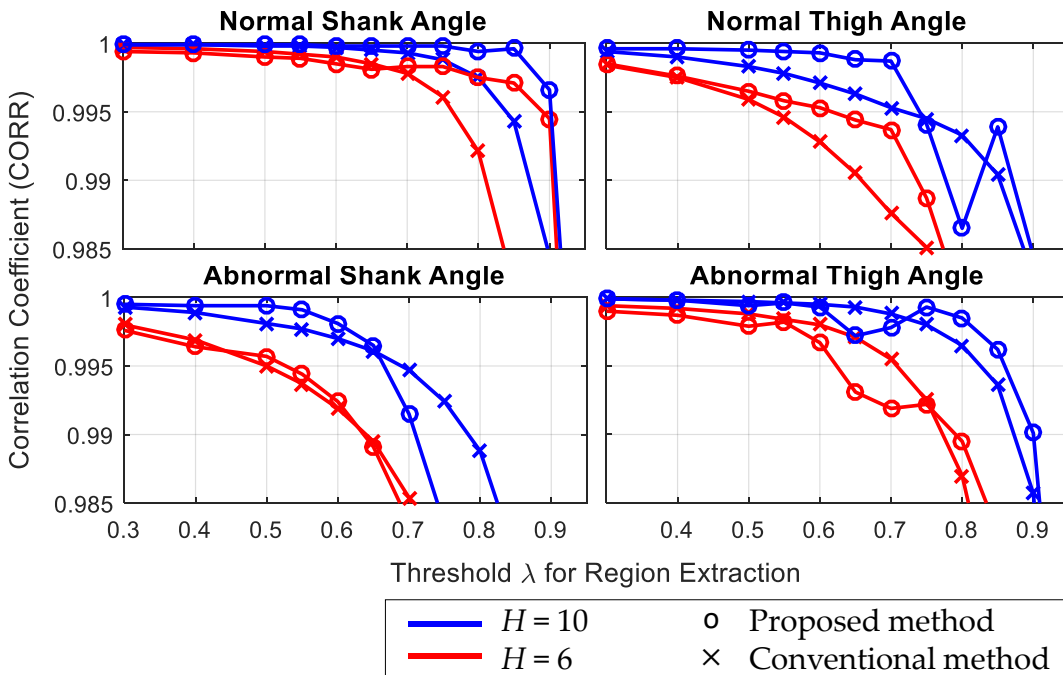


Fig. 4.52: Plot of mean CORR at Region B against thresholds λ when $H=6$ and 10.

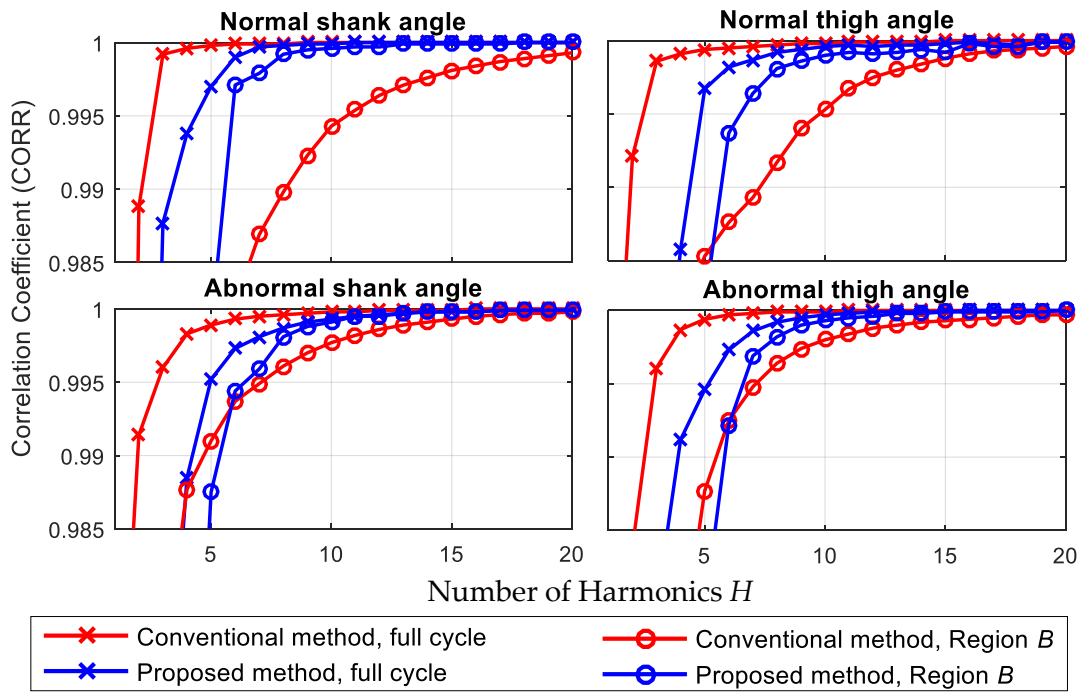


Fig. 4.53: Plot of mean CORR against H .

Table 4.23: Mean CORR (%) between Original and Reconstructed Angle Waveforms.

Angle	Number of Harmonics H	Conventional Method		Proposed Method	
		Full Cycle	Region B	Full Cycle	Region B
Normal shank	3	99.92	92.84	98.77	87.72
	6	99.99	98.22	99.90	99.71
	10	100.00	99.43	99.99	99.96
	15	100.00	99.81	100.00	99.99
	20	100.00	99.93	100.00	100.00
	25	100.00	99.97	100.00	100.00
Normal thigh	3	99.86	97.67	97.08	74.80
	6	99.95	98.76	99.82	99.37
	10	99.98	99.53	99.96	99.90
	15	100.00	99.88	99.98	99.92
	20	100.00	99.96	99.99	99.99
	25	100.00	99.98	100.00	100.00
Abnormal shank	3	99.60	97.52	96.64	87.37
	6	99.93	99.37	99.73	99.44
	10	99.98	99.77	99.93	99.91
	15	99.99	99.93	99.95	99.80
	20	100.00	99.98	99.99	99.99
	25	100.00	99.99	100.00	100.00
Abnormal thigh	3	99.61	95.57	97.99	94.22
	6	99.97	99.25	99.73	88.76
	10	99.99	99.80	99.97	99.93
	15	100.00	99.93	99.99	99.99
	20	100.00	99.97	99.83	100.00
	25	100.00	99.99	100.00	100.00

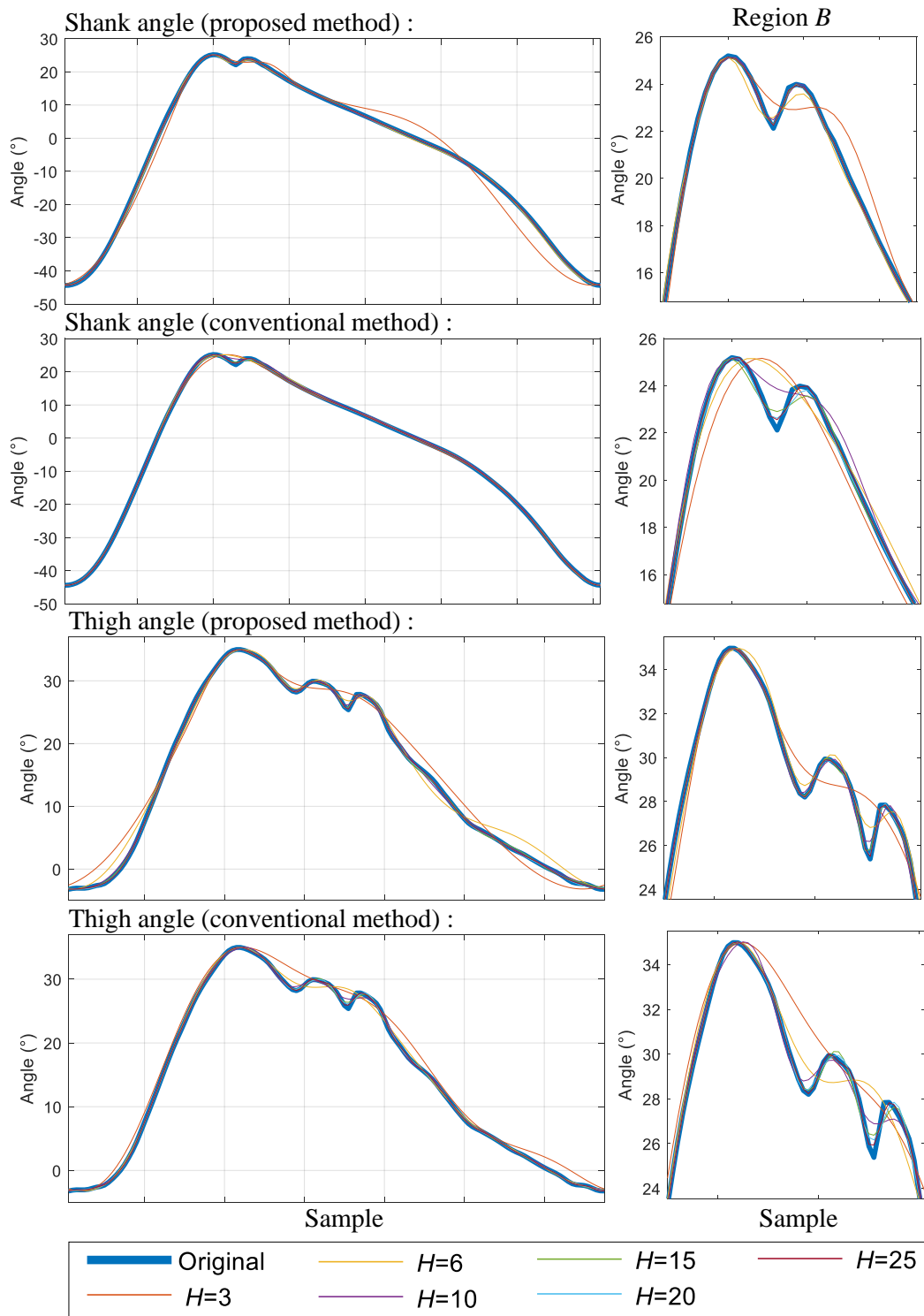


Fig. 4.54: Original and reconstructed angle waveforms.

The proposed method when $H=10$ averagely achieves the same CORR as conventional method when $H = 24, 17, 14,$ and 15 for normal shank, normal thigh, abnormal shank, and abnormal thigh angle waveforms, respectively. This means a reduction of 14, 7, 4, and 5 DFT calculations in (4.53) to achieve the same CORR.

Fig. 4.55 counts the number of computations required to run (4.53) per harmonic. As stated in Table 4.24, the total number of computations saved for 14, 7, 4, and 5 harmonics is $112L, 56L, 32L,$ and $40L,$ respectively. The proposed waveform scaling method in (4.48) – (4.49) uses around 202 additions and 101 multiplications. Adding with the computations required to extract the regions (Fig. 4.44) and scaling the waveform (Fig. 4.45), the computations required are far lesser than an $L \approx 1500$.

$$\begin{aligned}
 & \begin{array}{l} L \text{ cosine function} \\ L \text{ sine function} \end{array} \\
 & \begin{array}{l} e^{ix} = \cos(x) + j \sin(x) \\ \underbrace{\hspace{10em}}_{2L \text{ multiplications}} \end{array} \\
 DFT_h = & \sum_{i=1}^L \underbrace{k_1 \vartheta_i}_{L \text{ complex multiplications}} e^{j(k_2 h)(i-1)} \\
 & \begin{array}{l} \uparrow \\ L \text{ complex additions} \end{array} \\
 & L \approx 1500 \text{ is the length of the repeated waveform } \vartheta. \\
 & \begin{array}{l} k_1 = \frac{2}{L} \\ k_2 = -0.02\pi \end{array}
 \end{aligned}$$

Fig. 4.55: Number of computations required per harmonic.

Table 4.24: Approximate Number of Computations Required per Harmonic.

Number of Harmonics	Additions	Multiplications	Cosine / Sine function
1	$2L$	$4L$	$2L$
4	$8L$	$16L$	$8L$
5	$10L$	$20L$	$10L$
7	$14L$	$28L$	$14L$
10	$20L$	$40L$	$40L$
14	$28L$	$56L$	$28L$

1 complex addition = 2 additions. 1 complex multiplication = 2 multiplications. $L \approx 1500$ is the length of repeated waveform

Fig. 4.56 shows the shank's angular velocity estimated by differentiating the shank's angle (4.58). Fig. 4.56 is for the readers to visualize how the results in Table 4.25 are being obtained. The heel and toe strikes can be detected very accurately using the shank's angular velocity estimated from the angles based on proposed method. The shank's angular velocity estimated from the conventional method gives higher error in heel and toe strikes detections. This indicates the proposed method has successfully retained the heel and toe strikes information. As listed in Table 4.25, the proposed method when $H=10$ has lower MAE than conventional method when $H=25$ and $H=20$ for heel and toe strikes detections, respectively.

However, the proposed method gives higher MAE of about +1 sample difference more than conventional method in estimating the toe off. This is because the toe off is in Region A, while the proposed method is focusing on improving the CORR in Region B which consists of heel and toe strikes. To solve this, future work can consider extracting more than two regions and focusing on improving the CORR in multiple regions rather than just Region B.

The underlying questions are what is the advantage to represent the waveform mathematically and why not use the original measured waveforms instead? It is demonstrated in Table 4.26 that waveform scaling before DFT can increase the true positive rate of the gait multi-class classification by 5-7% when compared to the conventional method. The original waveforms with no waveform scaling give lower accuracy than the proposed method with waveform scaling in classification task. This shows that it is useful to time and amplitude-scale the angle waveforms to "enlarge" the distinctive regions of the angle waveforms for better classification accuracy.

It is also demonstrated in Table 4.25 that the proposed mathematical model has detected the gait phase more accurately than the conventional method. However, using the original waveforms would have been more accurate than proposed method. In application such as robotics that uses mathematical equation to generate gait patterns, original waveforms may be unavailable. An advantage of mathematical equation includes but not limited to lower memory storage. For example, saving an original waveform may require more than 150 float numbers, while mathematical equation requires 13 float numbers (when $H=6$) or 21 float numbers (when $H=10$) to regenerate that 150 data points per waveform. The proposed method may also be useful in data compression and encoding.

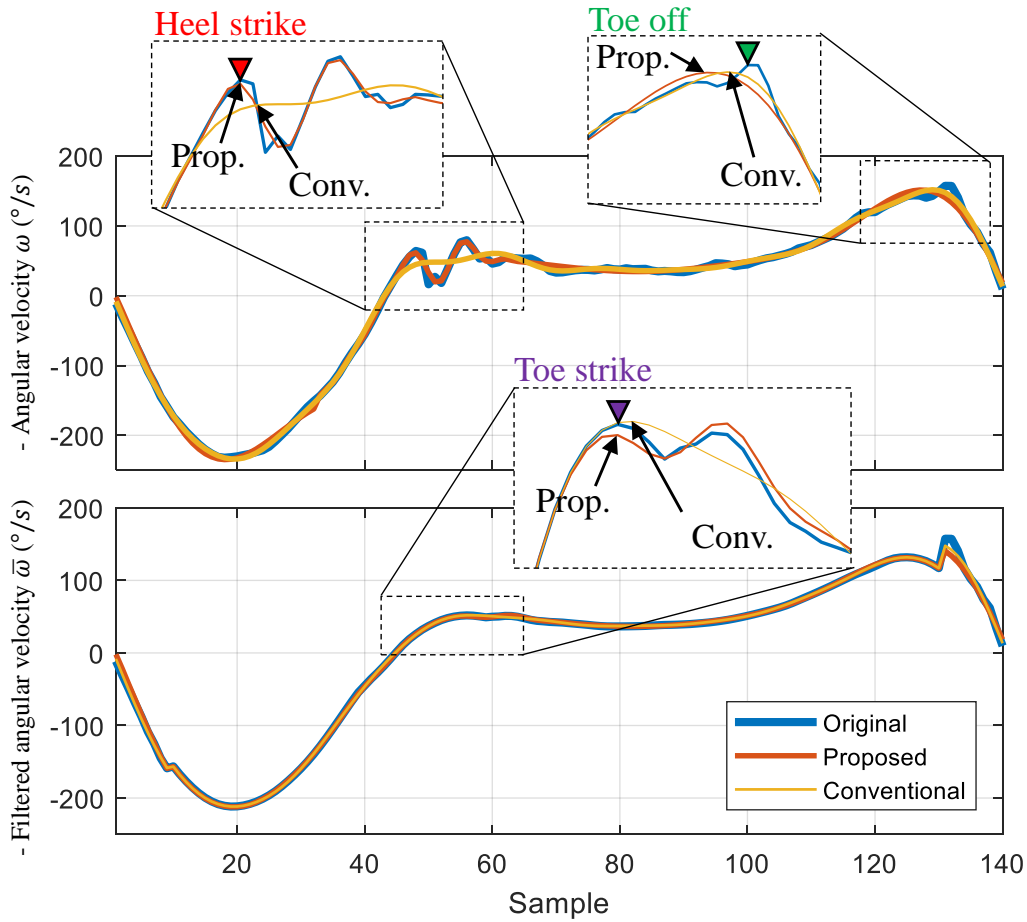


Fig. 4.56: Estimated shank's angular velocity to detect gait phases.

Table 4.25: Gait Phase Detection Error using Reconstructed Waveforms.

Error	Number of Harmonics H	Heel strike		Toe strike		Toe off	
		Conv.	Prop.	Conv.	Prop.	Conv.	Prop.
Sample	6	5.82	1.33	2.99	0.87	3.19	7.73
	10	4.29	0.73	2.06	0.47	2.67	3.74
	15	2.33	0.35	1.21	0.32	2.03	3.00
	20	1.33	0.36	0.48	0.22	1.70	2.75
	25	1.13	0.29	0.36	0.16	1.52	2.36
ms	6	58.20	13.30	29.90	8.70	31.90	77.30
	10	42.90	7.30	20.60	4.70	26.70	37.40
	15	23.30	3.50	12.10	3.20	20.30	30.00
	20	13.30	3.60	4.80	2.20	17.00	27.50
	25	11.30	2.90	3.60	1.60	15.20	23.60

Table 4.26: Multi-Class Classification Testing Accuracy.

Neurons N	Pattern	True Positive (%)		True Negative (%)		Accuracy (%)	
		Conv.	Prop.	Conv.	Prop.	Conv.	Prop.
15	1	100	100	97.04	98.60	97.78	98.95
	2	92.16	82.35	91.50	88.89	91.67	87.25
	3	62.50	92.86	86.90	95.83	80.80	95.09
	4	80.95	80.95	93.12	92.59	90.08	89.68
	Mean	83.90	89.04	92.14	93.98	90.08	92.74
15,8	1	99.07	100	99.22	98.60	99.18	98.95
	2	80.39	88.24	90.20	92.81	87.75	91.67
	3	82.14	91.07	92.86	97.02	90.18	95.54
	4	76.19	79.37	92.59	89.95	88.49	87.30
	Mean	84.45	89.67	93.72	94.59	91.40	93.36
20,15,8	1	100	100	99.84	100	99.88	100
	2	78.43	80.39	91.50	90.85	88.24	88.24
	3	78.57	94.64	92.86	95.24	89.29	95.09
	4	76.19	87.30	92.59	93.65	88.49	92.06
	Mean	83.30	90.58	94.20	94.93	91.47	93.85

- $N = [20,15,8]$ means there are three hidden layers in the neural network with 20, 15 and 8 neurons in the first, second and third layer, respectively.
- The reported testing accuracies are the best accuracies out of 100 trials.

4.5.5 Summary

A method to mathematically represent the shank and thigh angle waveforms accurately without smoothing and fluctuations is proposed. The proposed method has also been tested with simulated abnormal gait patterns. The CORR between the original and reconstructed waveforms is increased without increasing the number of harmonics. By reducing the number of harmonics without reducing the accuracy, the calculations for DFT can be reduced. It is shown that the proposed method when $H=10$ averagely achieves the same CORR as conventional method when $H = 24, 17, 14,$ and 15 for normal shank, normal thigh, abnormal shank, and abnormal thigh angle waveforms, respectively. This means a reduction of 4 to 14 DFT computations to achieve the same CORR. As the reconstructed waveforms based on proposed method represent the original waveforms accurately, the reconstructed waveforms are suitable for gait analysis such as gait phase detection. It is also demonstrated that the harmonic components of the scaled waveforms can increase the gait classification accuracy when distinctive regions of the waveforms are extracted.

4.6 Temporal Synchronization of Markerless Video and IMU Data

4.6.1 Introduction

It is beneficial to have joint angle information available to the clinicians while performing visual inspection. A video camera can be used together with IMUs so that both video and IMU data are available. To reduce cost, a smartphone camera is used in this research. Other applications that involve IMUs and video cameras include motion tracking [110], localization [111], and video stabilization [112].

As the recordings of video and IMU data are hard to be initialized at the same time due to human and software delay [113], there is a need to perform temporal synchronization for the video and IMU data. In this research, the video and IMU data of a person walking on a flat surface are temporally synchronized by detecting and matching the maximum backward swing of the reference leg detected from video and IMU. The proposed method is validated by blinking LED and sending LED flag to a computer (PC) at the same time.

Chapter 4.6 is covered by the following publication with minor amendment:

Y. C. Han, K. I. Wong and I. Murray, "Automatic Synchronization of Markerless Video and Wearable Sensors for Walking Assessment," in *IEEE Sensors Journal*, vol. 19, no. 17, pp. 7583-7590, Sept.1, 2019.

doi: 10.1109/JSEN.2019.2916163

© 2019 IEEE

4.6.2 Experimental Setup

Fig. 4.57 shows that the IMUs were strapped in front of the right shank using Velcro straps, and on top of the right foot using double-sided tape. A static front camera of the iPhone 6 Plus was used to capture video of the person walking. The red LED was placed at the bottom left of the video.

10 healthy adults (male: 7; female: 3; age: 21-49; height: 151-182cm) participated in the data collection. Each person was asked to walk self-pace on a flat surface for about 3 meters. In the first 5 trials, the participants were asked to start walking with their right legs. In the next 5 trials, the participants were asked to start walking with their left legs. A total of 100 walking trials was collected.

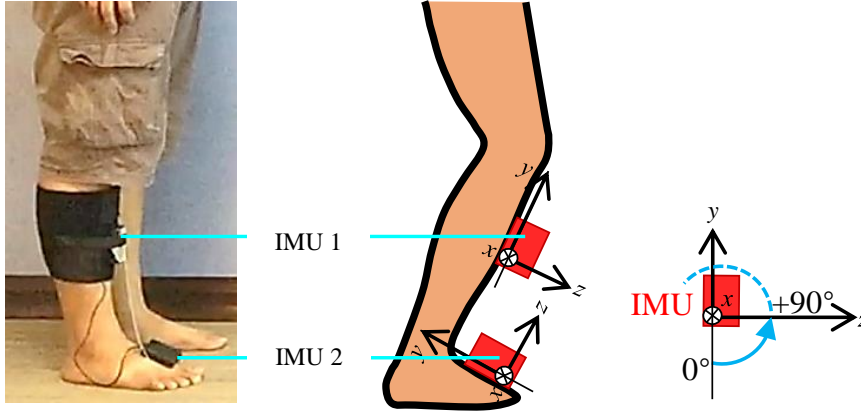


Fig. 4.57: IMU placement.

4.6.3 Proposed Method

4.6.3.1 IMU Data Processing

Fig. 4.58 shows the flowchart to detect maximum backward swing of the leg using IMU.

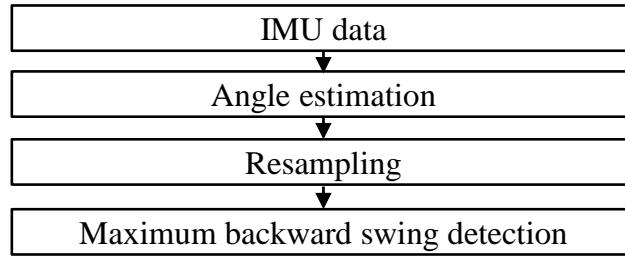


Fig. 4.58: IMU data processing.

Fig. 4.59 shows the shank and foot angle estimated using IMU data. The angle estimation algorithm used is based on Chapter 4.2.

As the IMU is sampled at 100Hz while the video is captured at 30Hz, the estimated angle needs to be resampled to 30Hz so that the IMU and video can be temporally synchronized. The total number of resampled angles can be calculated according to (4.60). The angle can be resampled according to (4.61).

$$\bar{N}_{IMU} = N_{IMU} \times \frac{f_v}{f_{IMU}} = N_{IMU} \times \frac{30}{100} \quad (4.60)$$

$$\bar{\theta}_j = \theta_{[i]}(i - [i] + 1) - \theta_{[i]}(i - [i]) \quad (4.61)$$

$$\text{for } \begin{cases} i = 1, 1 + \frac{N_{IMU}-1}{\bar{N}_{IMU}-1}, 1 + 2 \frac{N_{IMU}-1}{\bar{N}_{IMU}-1}, \dots, N_{IMU} \\ j = 1, 2, 3, \dots, \bar{N}_{IMU} \end{cases}$$

Where \bar{N}_{IMU} denotes the total number of resampled angles, and N_{IMU} denotes the total number of samples collected by IMU. f_{IMU} and f_v denote the sampling frequency of

the IMU and video camera, respectively. $\bar{\theta}$ denotes the resampled angle. $\lceil \cdot \rceil$ and $\lfloor \cdot \rfloor$ are the ceiling and flooring functions, respectively.

The first maximum backward swing of the shank and foot can be detected by finding the first minimum of the shank and foot angles, respectively. Fig. 4.60 illustrates that the first maximum backward swing can be detected by finding the minimum angle between x_1 and x_2 , where x_1 and x_2 are the first and second angles that cross the threshold $\lambda_1 = \min(\bar{\theta})/2$.

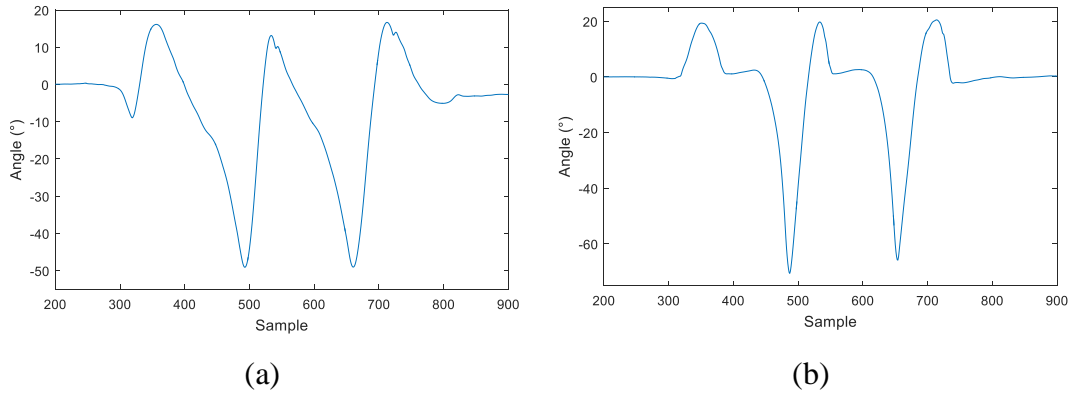


Fig. 4.59: Estimated angle. (a) Shank angle. (b) Foot angle.

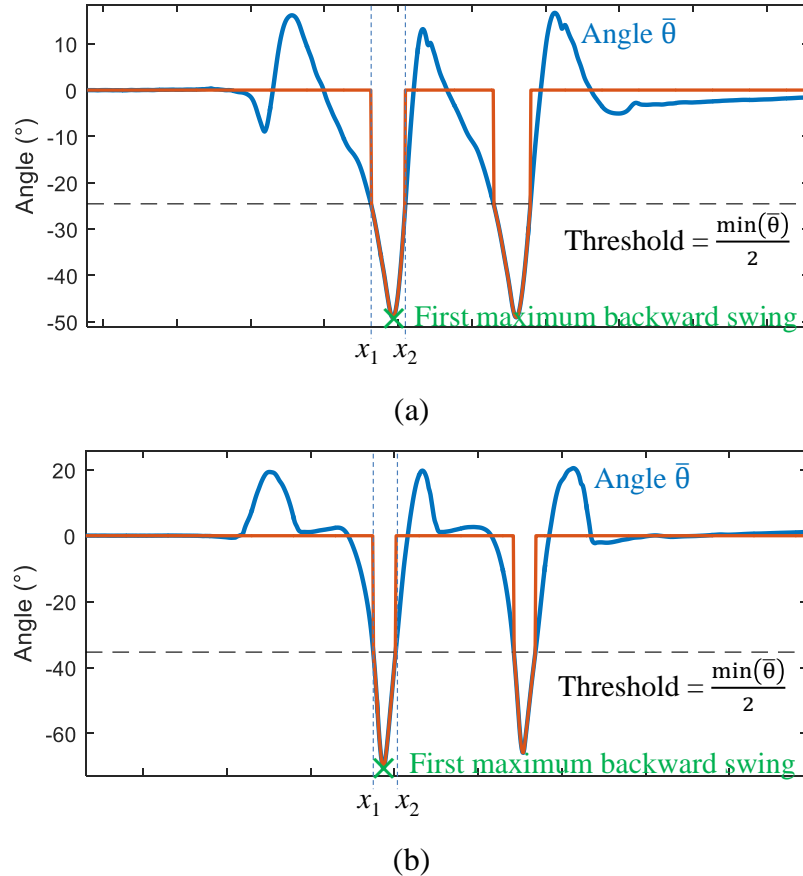


Fig. 4.60: First maximum backward swing detection. (a) Shank angle. (b) Foot angle.

4.6.3.2 Video Processing

Fig. 4.61 shows a flowchart to detect maximum backward swing of leg from video. The video captured from the smartphone is in RGB, as shown in Fig. 4.62(a). In order to detect the human motion, the video is first gray-scaled, as shown in Fig. 4.62(b), using MATLAB function ‘rgb2gray’ (4.62).

$$g_f = \text{rgb2gray}(v_f) \quad (4.62)$$

Where g denotes the gray-scaled video, v denotes the RGB video, and f denotes the f -th frame of the video.

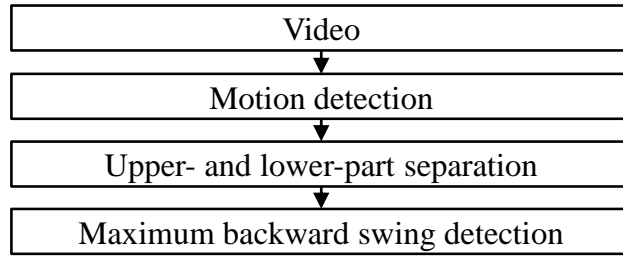


Fig. 4.61: Video processing flowchart.

The human motion can be detected by calculating the difference between the current and previous frames, and then convert it to black and white using MATLAB function ‘im2bw’ (4.63). Fig. 4.62(c) shows the detected motion.

$$M_f = \text{im2bw}\left(\left(g_f - g_{f-1}\right)^2, \lambda_2\right) \quad (4.63)$$

Where M denotes the detected motion in black and white, and λ_2 denotes the threshold. In this research, λ_2 is set to be 0.95 through trials and errors.

As shown in Fig. 4.63, the captured video is split into upper- and lower-parts equally (4.64) (4.65) to detect the maximum backward swing of the leg. The first 100 columns of the video are ignored because the first 100 columns are reserved for validation of proposed method using LED. In MATLAB, the first pixel was at the upper leftmost.

$$U = v_{\left(1 \text{ to } \frac{R}{2}, 100 \text{ to } c\right)} \quad (4.64)$$

$$L = v_{\left(\frac{R}{2} \text{ to } R, 100 \text{ to } c\right)} \quad (4.65)$$

Where U denotes the upper part of the video, and L denotes the lower part of the video v . $R = 720$ and $C = 1280$ denote the number of rows and columns of a video frame, respectively.



(a)

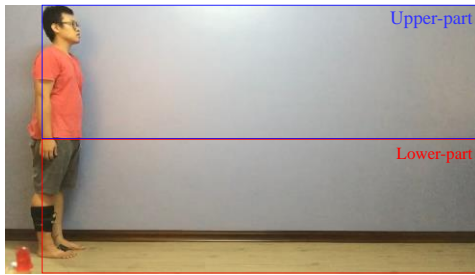


(b)

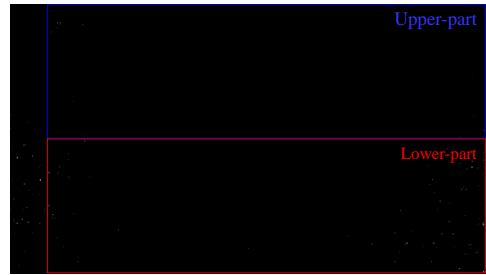


(c)

Fig. 4.62: Video paused at a frame. (a) RGB video v . (b) Gray-scaled video g . (c) Detected motion M in black and white.



(a)



(b)

Fig. 4.63: Upper- and lower-part separation. (a) RGB. (b) Detected motion M .

Fig. 4.64 shows the proposed method to approximate the extension of leg in horizontal axis. The number of white pixels at each column of the detected motion M is counted by summing up M column by column (4.66) (4.67).

$$W_{U,c} = \sum M_{U,c} \quad (4.66)$$

$$W_{L,c} = \sum M_{L,c} \quad (4.67)$$

Where M_U and M_L are the detected motion M at upper U and lower L parts, respectively. $W_{U,c}$ and $W_{L,c}$ denote the total number of white pixels at each column c of M_U and M_L , respectively.

The leftmost column of the detected human can be approximated by finding the first value of W that is greater than a threshold λ_3 (4.68) (4.69). As shown in Fig. 4.64, λ_3 can be safely set as 10 in this research, so that background reflections are ignored.

```
for ( $c = 100$  to  $1279$ ) do (4.68)
```

```
    if  $W_{U,c} > \lambda_3$  and  $W_{U,c+1} > \lambda_3$  then
```

```
         $c_U = c$ 
```

```
        break
```

```
    end if
```

```
end for
```

```
for ( $c = 100$  to  $1279$ ) do (4.69)
```

```
    if  $W_{L,c} > \lambda_3$  and  $W_{L,c+1} > \lambda_3$  then
```

```
         $c_L = c$ 
```

```
        break
```

```
    end if
```

```
end for
```

Where c_U and c_L denote leftmost column of detected human at upper U and lower L parts, respectively.

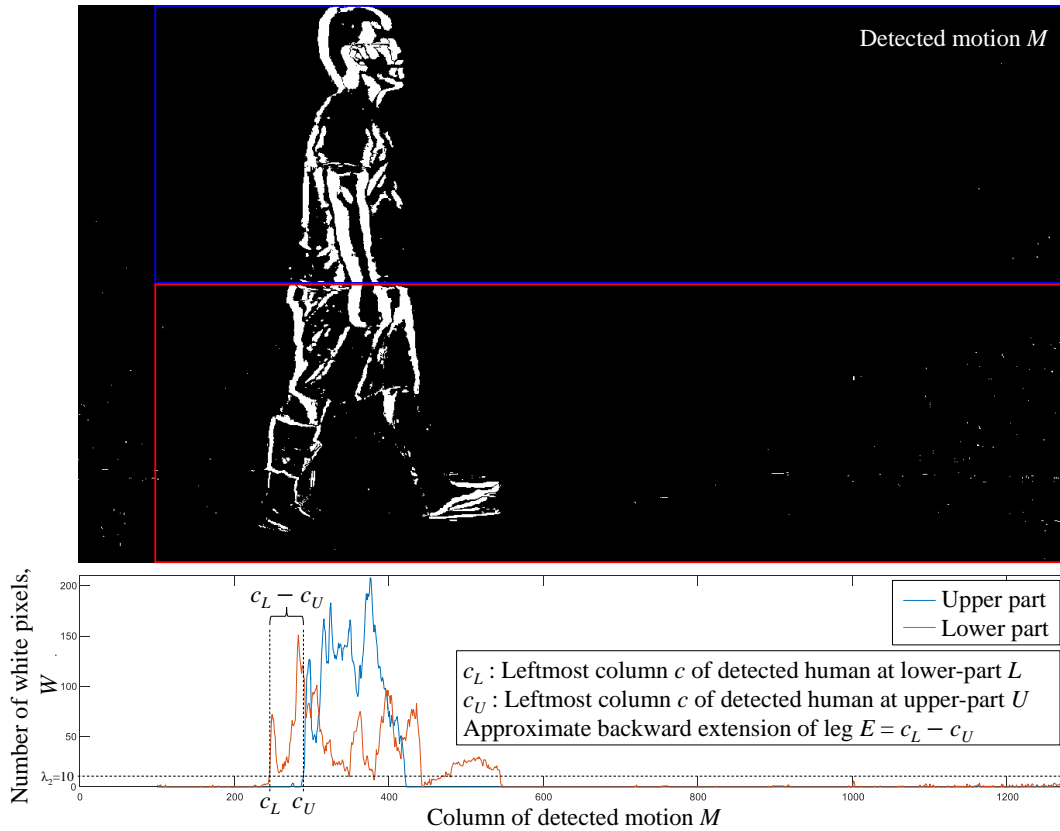


Fig. 4.64: Approximate extension of leg.

In cases where the motion is very low, such as the person is standing still at frame f in Fig. 4.63, c_U and c_L follow the previous values at frame $f - 1$ (4.70) (4.71). The initial c_U and c_L at the first frame are both set as 0. As shown in Fig. 4.65, the motion can be considered low when the total number of white pixels is lower than a threshold $\lambda_4 = 1000$.

$$\text{if } \sum W_{U,f} < \lambda_4 \text{ then} \quad (4.70)$$

$$c_{U,f} = c_{U,f-1}$$

end if

$$\text{if } \sum W_{L,f} < \lambda_4 \text{ then} \quad (4.71)$$

$$c_{L,f} = c_{L,f-1}$$

end if

Where $\sum W_{U,f}$ and $\sum W_{L,f}$ are the total number of white pixels in M_U and M_L at frame f , respectively.

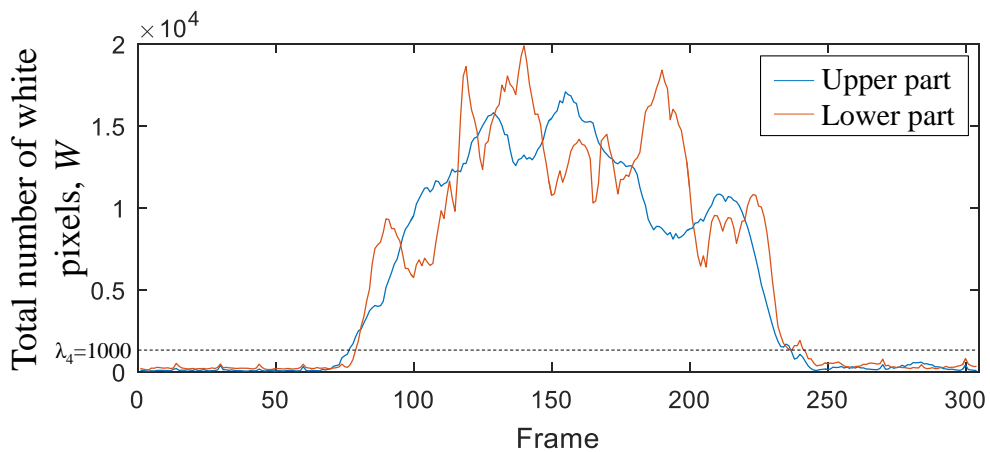


Fig. 4.65: Total number of white pixels in M .

The backward extension E of the leg is estimated by finding the difference between c_U and c_L (4.72).

$$E = c_L - c_U \quad (4.72)$$

Fig. 4.66 shows the approximated extension of leg at all frames based on proposed method. The first minimum of E can be detected by finding the minimum value between x_1 and x_2 , while the second minimum of E can be detected by finding the minimum value between x_3 and x_4 , where x_1 to x_4 denote the first to the fourth crossings of the threshold $\lambda_5 = \min(E)/2$.

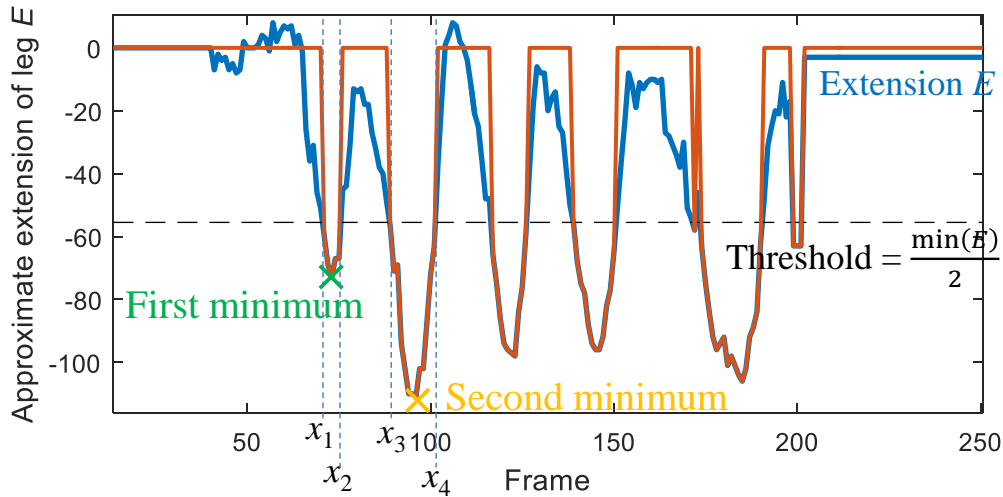


Fig. 4.66: Estimated maximum backward swings of leg.

4.6.3.3 Synchronization of Video and IMU Data

Fig. 4.67 shows the flowchart to synchronize video and IMU data. As the approximated leg extension E includes both the extension of right and left legs, it is needed to identify whether the person starts to walk with right or left leg before synchronization.

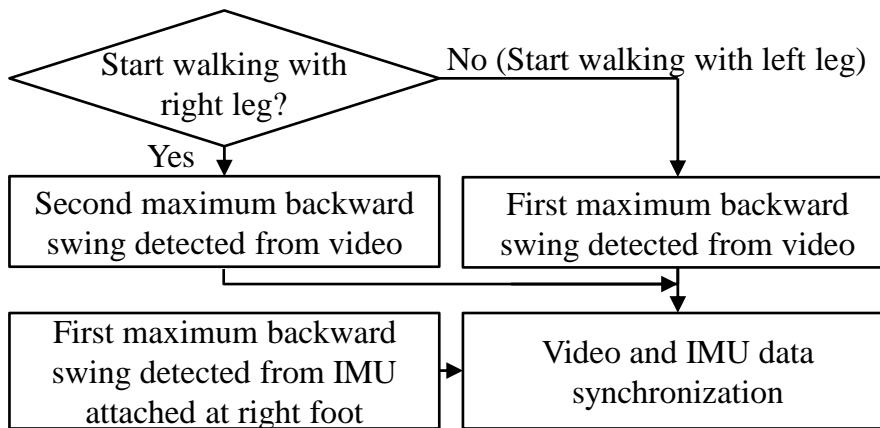


Fig. 4.67: Flowchart to synchronize video and IMU data.

When the IMU is attached to the right leg, and the person starts to walk with right leg, there is a forward swing before the first maximum backward swing, as shown in the shank and foot angle waveforms in Fig. 4.68. However, as shown in Fig. 4.69, when the person starts to walk with left leg, there is no forward swing before the first maximum backward swing. Therefore, the maximum angle between the first sample

and the maximum backward swing B needs to be found. When there is no forward swing before the first maximum backward swing, the maximum angle between the first sample and B approaches zero (4.73).

$$\mathbf{if} \max(\bar{\theta}_{1 \text{ to } B}) \rightarrow 0 \mathbf{ then} \quad (4.73)$$

The person starts to walk with left leg.

else

The person starts to walk with right leg.

end if

The video v and IMU resampled angle $\bar{\theta}$ can be synchronized such that the video at frame A is synchronized with the IMU sample B minus a constant k (4.74). The constant k is to reduce the error. It is discovered using the validation method in next section (Chapter 4.6.3.4), $k = 3$ for shank angle, while $k = 2$ for foot angle. Fig. 4.68 and Fig. 4.69 show the synchronized video and IMU data.

$$v_{A+i} \equiv \bar{\theta}_{B-k+i} \quad \text{for } i = 0, 1, 2, \dots \quad (4.74)$$

If the person starts to walk with right leg, $A =$ second minimum of E . If the person starts to walk with left leg, $A =$ first minimum of E . The symbol ‘ \equiv ’ denotes synchronization.

In (4.61), the IMU signal is down-sampled to 30Hz. This sampling rate is considered fast enough for human’s visual inspection. However, in case some applications such as automatic activity recognition that may require higher sampling rate, the original angle θ can be synchronized with the video starting from sample C (4.75).

$$C = (B - k) \times \frac{f_{IMU}}{f_v} = (B - k) \times \frac{100}{30} \quad (4.75)$$

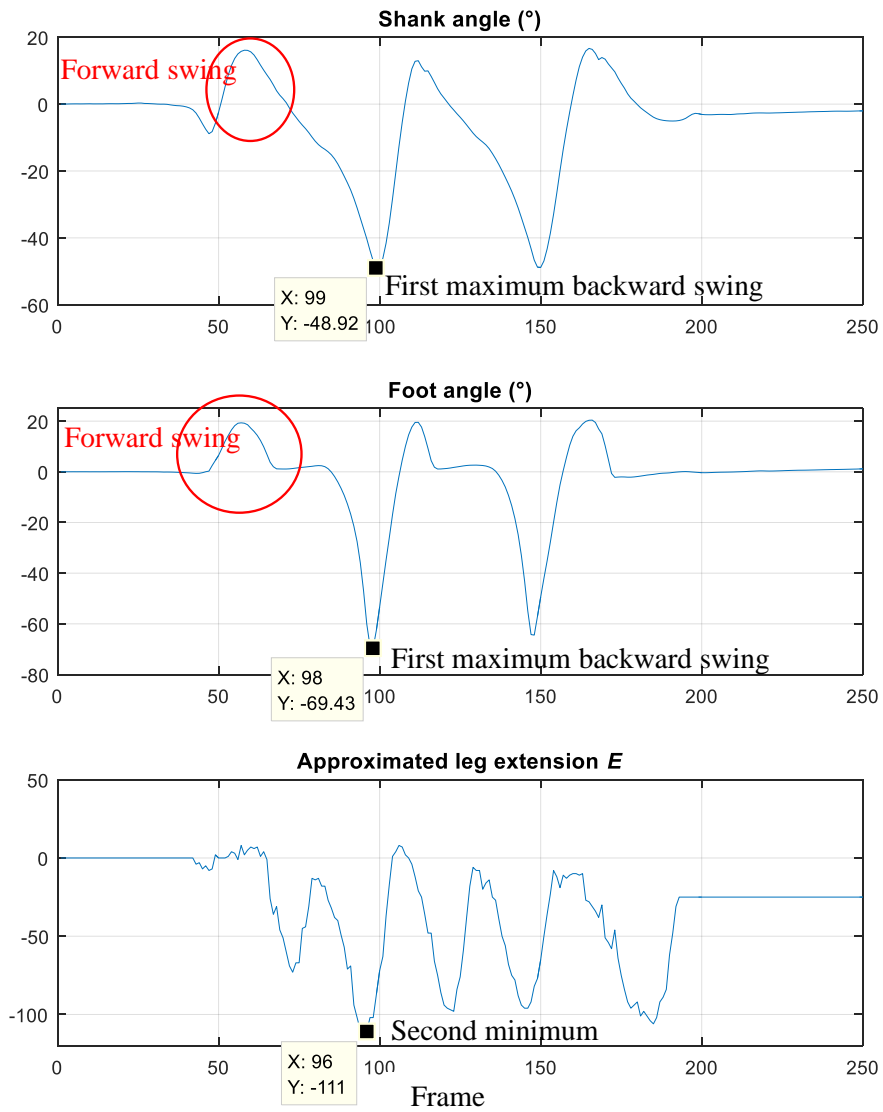


Fig. 4.68: Synchronize video and IMU data using the second minimum of E when the person starts to walk with right leg.

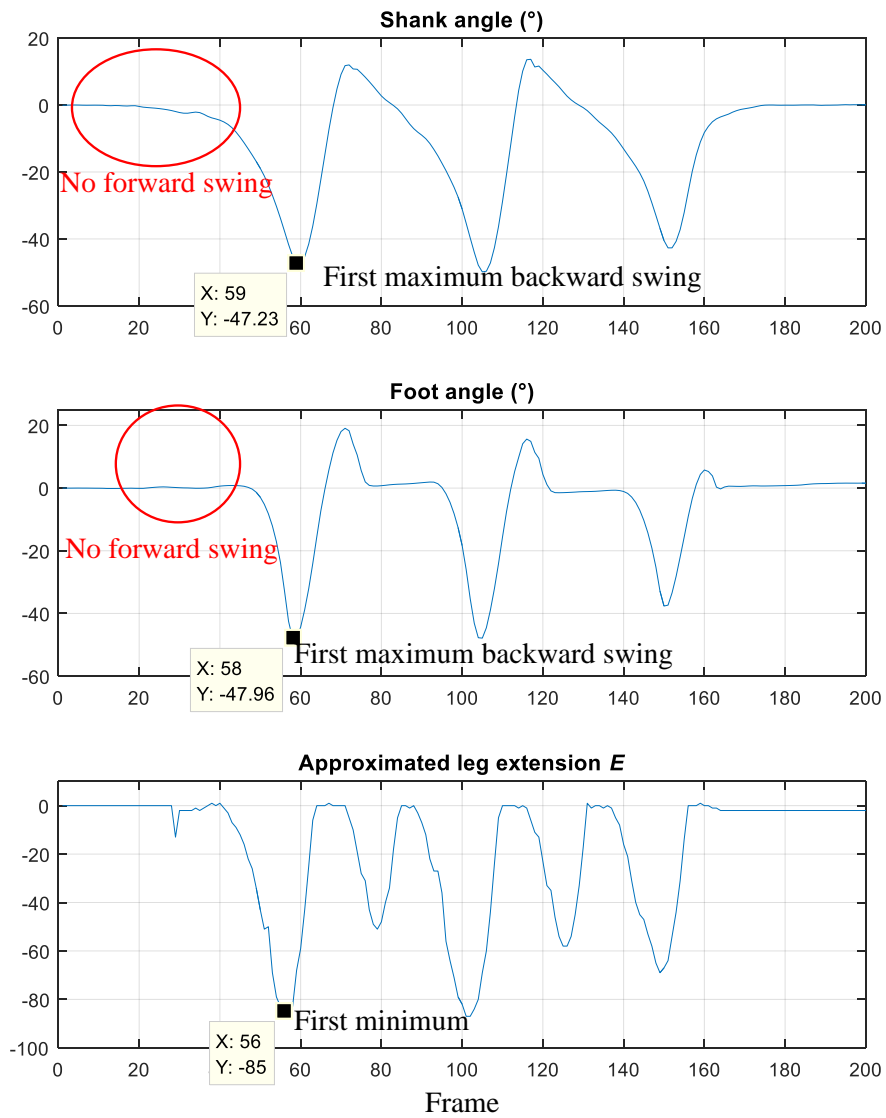


Fig. 4.69: Synchronize video and IMU data using the first minimum of E when the person starts to walk with left leg.

4.6.3.4 Validation of Proposed Method using Blinking LED

Inspired from the method in [73] which used blinking LEDs and RF transmitters to synchronize video and markers, a blinking LED and a RF transmitter are utilized to synchronize video and IMU data, for validation of the proposed method.

As stated in Fig. 4.70, the IMU blinks LED and at the same time encodes LED flag = 1 in its data transmission to the PC. The video and IMU data can then be synchronized using the first blink of the LED and the first LED flag = 1.

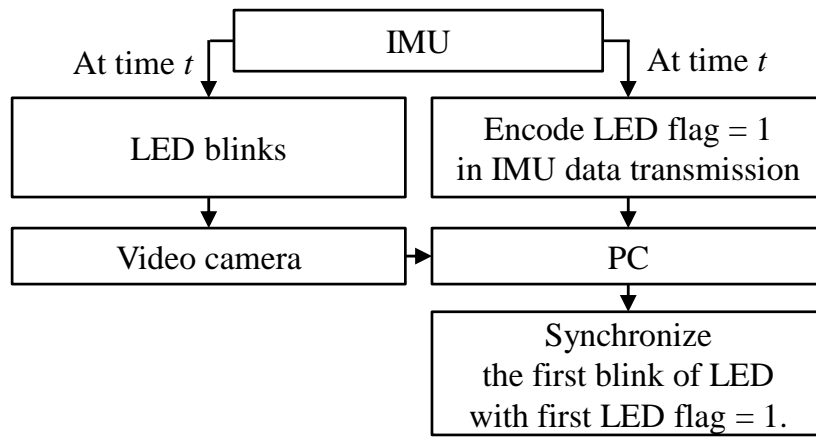


Fig. 4.70: Blinking LED to evaluate proposed method.

The motion detection method in (4.63) is used to detect the blinking of LED. As shown in Fig. 4.71, when the LED is off, the number of white pixels in the detected motion is very low. When the LED blinks, the number of white pixels is very high. Therefore, the blinking of LED can be detected when the number of white pixels is more than a threshold $\lambda_5 = 500$.

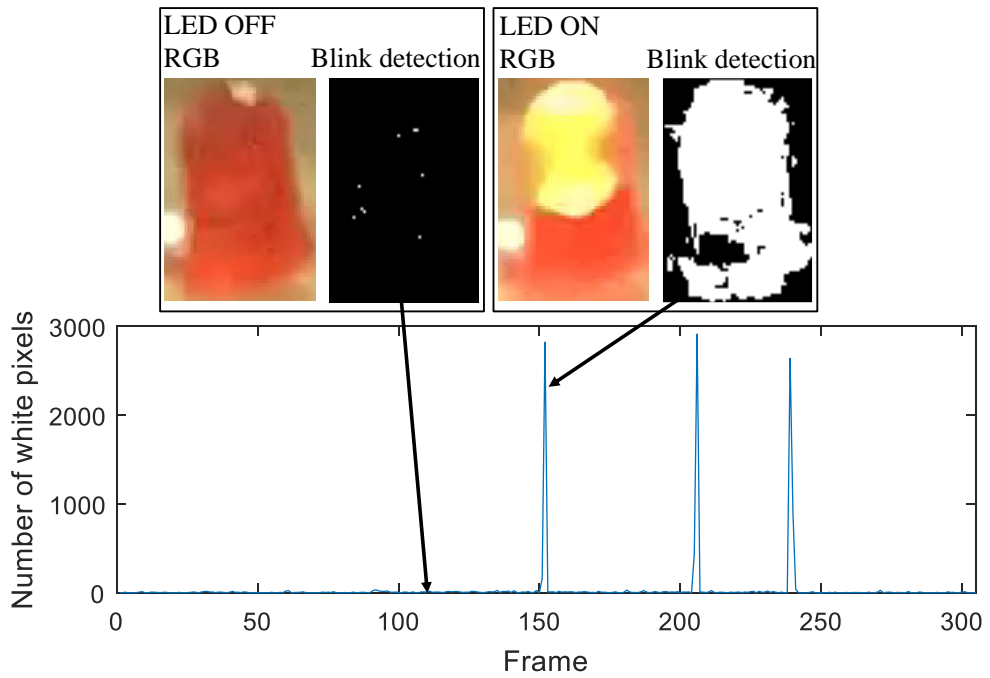


Fig. 4.71: LED blink detection.

The video and IMU data can then be synchronized such that the first LED flag is matched with the first blink of LED, as shown in Fig. 4.72.

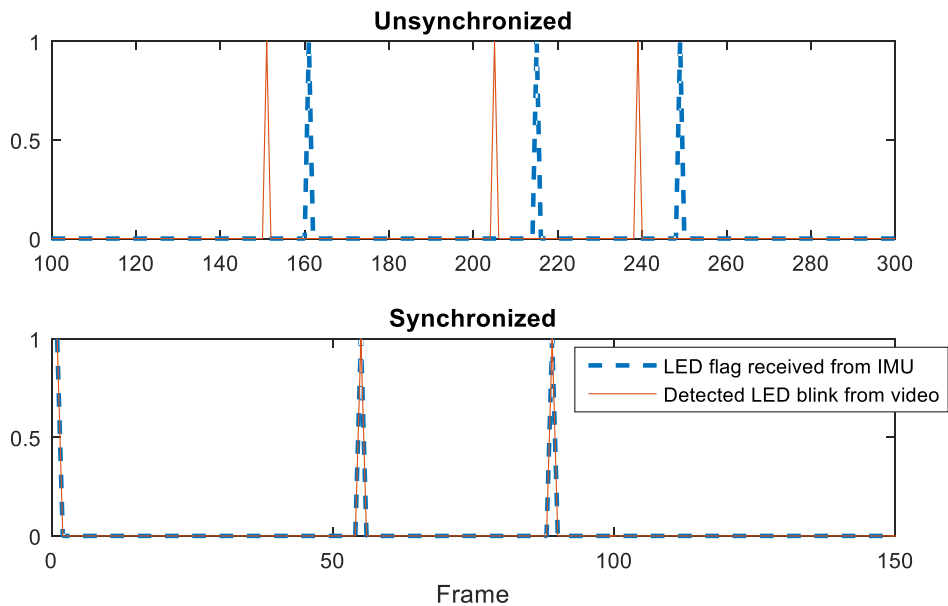


Fig. 4.72: Synchronize video and IMU data using first LED flag and first LED blink.

4.6.4 Results and Discussion

Table 4.27 shows the synchronization error of the proposed method based on the maximum backward swings of leg detected using shank and foot angles. The synchronization error is the difference between the video frame with the first blink of LED and the synchronized time generated by the proposed algorithm. The synchronization of video and IMU data using either shank or foot angles is very reliable with low MAE of less than 1 frame. The maximum error is also low at about 2 frames.

As shown in the third plots of Fig. 4.68 and Fig. 4.69, the extension of leg E approximated in this research is noisy, but it can be used to detect the maximum backward swings of legs accurately.

Table 4.27: Synchronization Error of Proposed Method.

Subject	Based on Shank Angle				Based on Foot Angle			
	Error (Frame)		Error (ms)		Error (Frame)		Error (ms)	
	MAE	Max	MAE	Max	MAE	Max	MAE	Max
1	0.8	1.0	27	33	0.5	2.0	17	67
2	0.9	2.0	30	67	1.0	2.0	33	67
3	1.0	2.0	33	67	1.0	2.0	33	67
4	0.6	2.0	20	67	0.3	2.0	10	67
5	0.7	2.0	23	67	1.4	3.0	47	100
6	1.1	2.0	37	67	1.3	2.0	43	67
7	0.3	1.0	10	33	0.5	2.0	17	67
8	0.9	1.0	30	33	0.8	2.0	27	67
9	0.7	2.0	23	67	1.3	2.0	43	67
10	1.0	1.0	33	33	1.0	2.0	33	67
Average	0.8	1.6	27	53	0.9	2.1	30	70

Table 4.28 shows several existing methods to synchronize video and inertial sensors. Bae *et al.* [70] used a synchronization hardware module to synchronize video camera and gyroscope signal. The main limitation is that the video camera and gyroscope signal must be connected through the hardware. However, the smartphone and the IMU are two separate systems and not connected together. The method by

Plotz *et al.* [71] had achieved very low error, but it also requires an external hardware, i.e. an Arduino board connected to personal computer (PC) to control seven LEDs for transmission time delay estimation.

Compared to the existing methods above, an advantage of the proposed method is that it does not require external device or LED for synchronization. Validated against the LED-blinking method, the proposed method achieves very low synchronization error at an average of 0.9 frames. There are also existing synchronization methods which do not require external hardware. Cippitelli *et al.* [72] used cross-correlation method to synchronize video and accelerometer data. Although horizontal hand gesture had very low synchronization error, the circular hand gesture had very high error. Liu *et al.* [40] recorded the inertial sensor data right after the Kinect SDK software received signal from the Kinect camera. Although [40] did not report the synchronization error, the method most likely consists of synchronization error due to the transmission time delay as stated in [71].

Table 4.28: Comparison of Video-Inertial Sensor Synchronization Methods among Literatures.

Reference	Method	MAE (in frames)
Bae <i>et al.</i> [70]	Hardware	Not reported
Plotz <i>et al.</i> [71]	Estimate camera-PC and sensor-PC transmission delay	<1
Cippitelli <i>et al.</i> [72]	Cross-correlation	0.5 (horizontal gesture)
		>10 (circular gesture)
Liu <i>et al.</i> [40]	Record sensor data right after Kinect SDK software receives Kinect signal	Not reported
Proposed Method	Maximum backward swing detection	0.8 – 0.9

As shown in Table 4.29, the average execution time to synchronize the video and inertial sensor data is 1.12 and 2.05 seconds for 15 frame/s and 30 frame/s videos, respectively, while the synchronization errors are almost the same. The computation time is considered long, and it is mainly because the proposed method requires all

video frames to be processed to obtain the threshold = $\min(E)/2$ as shown in Fig. 4.66. The frame-by-frame reading of the video in MATLAB consumes most of the computation time, compared to the processing of the algorithms.

There are several methods to reduce the computation time drastically, such as by calculating the threshold = $\min(E_{1 \rightarrow N/2})/2$ instead of threshold = $\min(E_{1 \rightarrow N})/2$ where N is the total number of frames. However, the 2-second computation time is not a problem as the proposed method is designed to assist clinicians in walking assessment, which does not require real-time processing.

Table 4.29: Average Execution Time and Synchronization Error of Proposed Method at Different Frame Rates.

Frame rate (frame/s)		15	30
Average execution time (s)		1.12	2.05
Mean absolute synchronization error (ms)	Shank	32	27
	Foot	25	30

The original video (30 frame/s) is down-sampled to 15 frame/s for comparison.

Fig. 4.73 shows a paused video of a person walking with the synchronized shank and foot angle shown at the right side. This allows the clinicians to know the shank and foot angles for possibly better visual inspection of the gait. The full video of Fig. 4.73 is attached with the published journal and can be downloaded at [114].

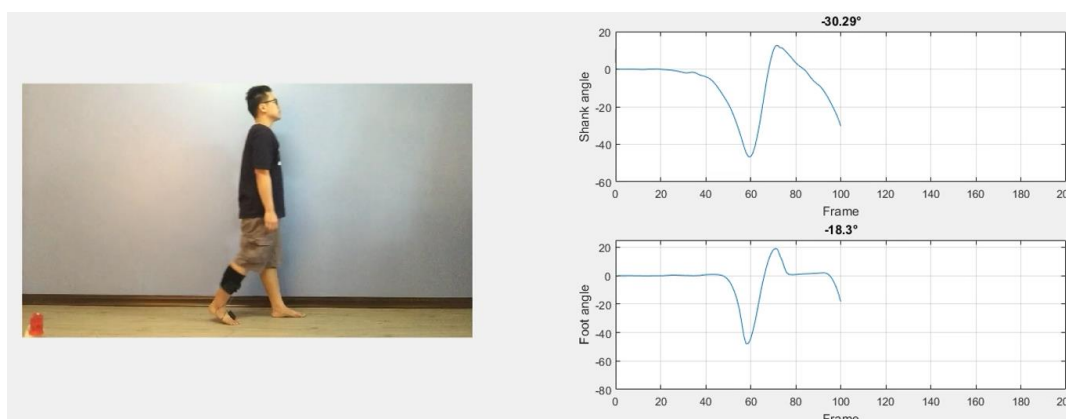


Fig. 4.73: Synchronized output for visual inspection paused at 100th frame.

In this research, two IMUs were used, but more inertial sensors can be added for full body tracking as long as they are temporally synchronized. Additionally,

synchronized force sensitive resistors (FSRs) used in Section 4.4 can be added for gait phase detection. With 3-D angle estimation algorithm such as [34], [80], and the proposed method in Chapter 4.2, the 3-D joint angle information could also be provided to the clinicians for visual inspection. Other than providing the joint angle information, gait phase information can be added to the video.

A limitation of the proposed method is that the video must be captured from the side of the user for maximum backward swing detection. The proposed method cannot be used to detect maximum backward swing of the subject if the video is captured from the front. Additionally, the proposed method can only support one user. If there are two people moving in the video, the proposed method cannot differentiate which user is wearing the IMUs.

4.6.5 Summary

A method to temporally synchronize video and IMU data was proposed. The proposed method is based on motion detection, and it had achieved very low errors without having access to the camera and inertial sensor's internal system clocks. The main idea of the proposed method is to detect and match the maximum backward swing of the leg for synchronization. The mean absolute synchronization error of the proposed method was low at ± 1 frames. The synchronized joint angle information obtained from the IMUs was placed side-by-side to the video for clinicians to perform visual inspection. The main limitation is that the video must be captured from the side of human for maximum backward swing detection. The proposed method cannot be used to detect maximum backward swing of the subject if the video is captured from the front.

4.7 Stride Length Estimation based on a single Shank's Gyroscope

4.7.1 Introduction

Stride length is one of the important measurements in gait analysis. Several IMU-based stride length estimation algorithms are available in literature. Some algorithms are dependent on personalized parameters such as the height, leg length, and/or weight, which vary among different users [8] [9]. This requires each user to key in their personalized parameters manually for stride length estimation. There are also several algorithms that describe the relations between the acceleration and/or step frequency for stride length estimation, without requiring the user to input any data manually [10]-[14]. Additionally, some researchers employ machine learning methods such as deep convolutional neural network [15] and long short-term memory [16] for stride length estimation, but machine learning methods require high computations.

In this chapter, an algorithm to estimate the stride length based on a single shank's gyroscope is proposed and validated against Vicon optical motion capture system. 3 new important features for stride length estimation are proposed based on a linear kinematics equation.

Chapter 4.7 is covered by the following publication with minor amendment:

Y. C. Han, K. I. Wong and I. Murray, "Stride Length Estimation Based on a Single Shank's Gyroscope," in *IEEE Sensors Letters*, vol. 3, no. 10, pp. 1-4, Oct. 2019.

doi: 10.1109/LSSENS.2019.2942177

© 2019 IEEE

4.7.2 Experimental Setup

The same dataset with IMUs and Vicon in Chapter 4.2 is used. The angle direction is as shown in Fig. 4.41. As shown in Fig. 4.1, two IMUs, each consisting of a tri-axial accelerometer and a tri-axial gyroscope (MPU6150) sampling at 100Hz, were strapped at the outer side of the thigh and shank using Velcro straps. For validation, the markers of the Vicon system were placed on the IMUs. The 3-D movement of the thigh and shank were tracked simultaneously using IMUs and Vicon system. Each subject was requested to stand still for 3 to 5 seconds, then walk straight on a flat surface for 3 to 5 steps, and finally stood still for another 3 to 5 seconds. A total of 30 normal walking trials (132 strides) from 10 healthy adults (male: 8; female: 2; age: 22-35; height: 160-177cm; weight: 55-94kg) is used in this chapter.

4.7.3 Proposed Method

Each gait cycle is extracted from one maximum shank angle to another, as shown in Fig. 4.74. The ideal distance travelled is measured with Vicon based on the position of markers placed on the shank.

The kinematic equation states that $s = 0.5(u + v)t$, where s is the displacement, u is the initial speed, v is the final speed, and t is the time elapsed. It must be noted that this is a linear kinematic equation. A linear kinematic equation is attempted because the distance travelled during the shank's extension is almost linear, as shown in Fig. 4.74. Therefore, there are 3 variables (u , v , and t) that are needed to be identified to estimate the displacement, i.e. the stride length.

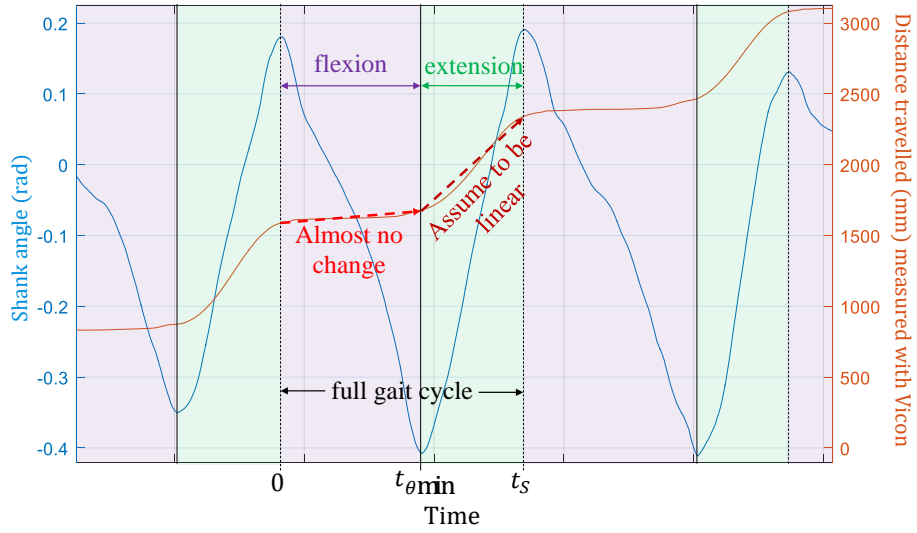


Fig. 4.74: Gait cycle extraction based on shank angle, and the distance travelled measured with Vicon.

During the shank's flexion, the distance travelled changes slightly as shown in Fig. 4.74. Therefore, the model in Fig. 4.75 can be drawn such that the central position of shank's IMU remains during the shank's flexion, while the gyroscope z-axis would measure the angular velocity ω_z . According to Fig. 4.75, the initial speed u can be estimated as (4.76).

$$u = r\bar{\omega}_{z,\text{flexion}} \quad (4.76)$$

$$\bar{\omega}_{z,\text{flexion}} = \frac{1}{n_{\theta\min}} \sum_{n=0}^{n_{\theta\min}} \omega_{z,n}$$

Where r is the radius as shown in Fig. 4.75. Since the IMU is strapped on the shank, and the foot is mostly on the ground during shank's flexion, r can be defined as the

distance between the IMU and the joint of ankle. $\bar{\omega}_{z,\text{flexion}}$ is the average angular velocity of the leg during shank's flexion. $n_{\theta_{\min}}$ is the n^{th} sample when the shank angle is minimum.

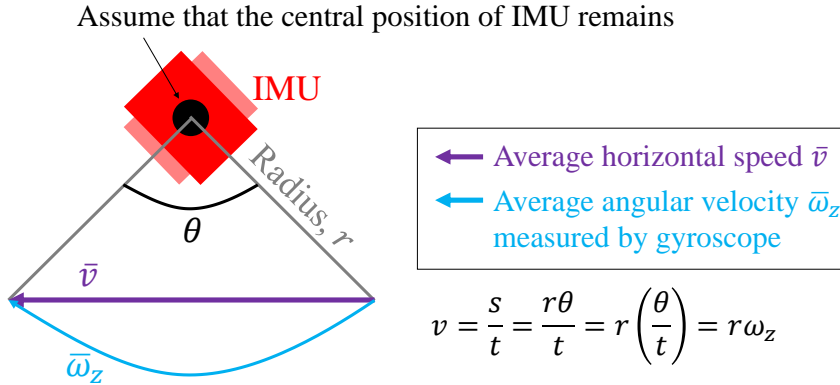


Fig. 4.75: Model to convert angular velocity to horizontal speed.

When the shank extends, the position of IMU changes, which means the model in Fig. 4.75 is not valid during shank's extension. However, when looking at a shorter time scale, i.e. sampling time Δt , it can still be assumed that the central position of IMU remains from one sample to the next because the change in IMU position is small. Therefore, the final velocity v can be estimated as (4.77). The derivation of (4.77) is based on Fig. 4.76.

$$\begin{aligned}
 v_1 &= v_0 + a_0 \Delta t \\
 v_2 &= v_1 + a_1 \Delta t \\
 v_3 &= v_2 + a_2 \Delta t \\
 v &= v_3 + a_3 \Delta t \\
 &= (\sum_{n=0}^{N-1} v_n) + \Delta t (\sum_{n=0}^{N-1} a_n) \\
 &\approx (\sum_{n=0}^{N-1} r_n \omega_{z,n}) + \Delta t (\sum_{n=0}^{N-1} a_n) + \varepsilon
 \end{aligned} \tag{4.77}$$

Where N is the total number of samples collected within a stride. The radius r_n changes from time to time and is not equal to the distance between IMU and ankle joint because the leg is swinging above the ground. a is the horizontal acceleration. ε is the error mainly resulted from the assumption.

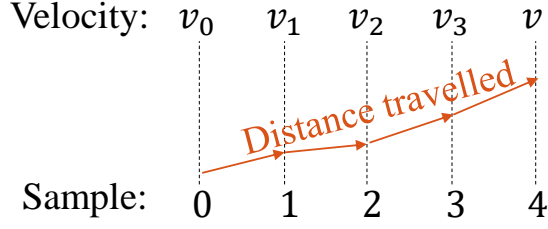


Fig. 4.76: Estimation of final velocity.

Substituting the estimated initial and final velocity into the kinematic equation, it is obtained that:

$$\begin{aligned}
 L &= 0.5(u + v)t \\
 &= 0.5 \left(r\bar{\omega}_{z,\text{flexion}} + \left(\sum_{n=0}^{N-1} r_n \omega_{z,n} \right) + \Delta t \left(\sum_{n=0}^{N-1} a_n \right) + \varepsilon \right) t_{\text{extension}} \quad (4.78)
 \end{aligned}$$

Where $t_{\text{extension}} = (N - n_{\theta_{\min}})\Delta t$, is the duration of the shank's extension. $t_{\text{extension}}$, rather than the total duration of the stride, is used because the horizontal distance increases almost linearly during the shank's extension, while remains during the shank's flexion.

As the IMU is not able to measure the horizontal acceleration a_n directly due to the change in IMU axes direction during shank's movement, it is replaced with an unknown value which would be estimated automatically using an optimization algorithm. As r_n , i.e. the distance between the IMU and ground with shank angle at n^{th} sample, keeps changing from time to time, it is also replaced with an unknown value to be estimated using the optimization algorithm. The value of r , i.e. the distance between IMU and ankle joint, is also estimated using the optimization algorithm although it can be measured but varies among different participants. Therefore, the proposed stride length estimation equation is derived as (4.79), where b is the bias to reduce error.

$$L_{\text{proposed},1} = (w_1 \bar{\omega}_{z,\text{flexion}} + w_2 \sum_{n=0}^{N-1} \omega_{z,n} + b_1) t_{\text{extension}} + b_2 \quad (4.79)$$

As this had become an optimization problem, the stride length is estimated by weighing each feature (4.80).

$$L_{\text{proposed},2} = w_1 \bar{\omega}_{z,\text{flexion}} + w_2 \sum_{n=0}^{N-1} \omega_{z,n} + w_3 t_{\text{extension}} + b \quad (4.80)$$

The optimization algorithm used in this research is the genetic algorithm in MATLAB. The optimization is run for 100 trials to choose the weights and bias that give the minimum error. The loss function is a RMSE. Other than the maximum number of generations is increased to 2000, other parameters are set as default values

such as population size = 50, elite count = $0.05 \times$ population size, and crossover fraction = 0.8. The optimization is terminated when the average change in the fitness value is less than 10^{-6} .

4.7.4 Results and Discussion

Fig. 4.77 shows the best fitness value versus generation for one of the optimization trials. The proposed methods took about 300 generations to converge to the best results, while $L_{Abhayasinghe}$ and L_{Diaz} took around 150 generations. However, the proposed methods obviously have lower errors than existing methods.

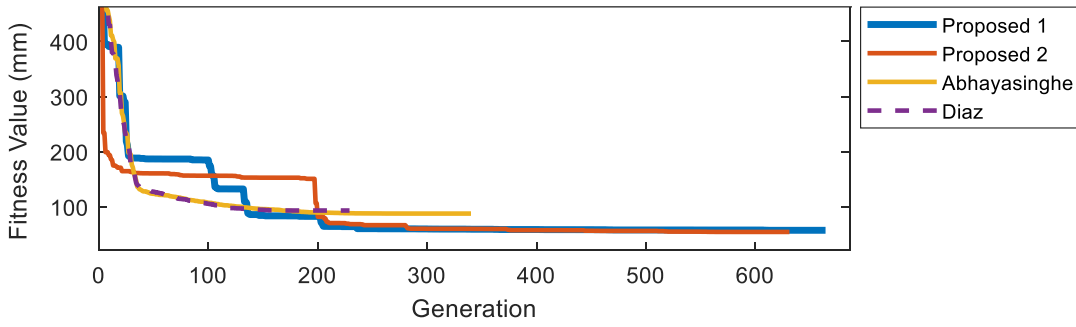


Fig. 4.77: Best fitness value versus generation.

Fig. 4.78 shows some of the estimated stride lengths with the ground truth from gold standard Vicon. The mean absolute error (MAE) is counted as (4.81), while the standard deviation (STD) of the error is counted as (4.82). S denotes total number of stride lengths. AE is the absolute error (4.83).

$$MAE = \frac{1}{S} \sum_{s=1}^S AE_s \quad (4.81)$$

$$STD = \sqrt{\frac{1}{S} \sum_{s=1}^S |AE_s - MAE|} \quad (4.82)$$

$$AE_s = |L_{estimated,s} - L_{Vicon,s}| \quad (4.83)$$

Referring to Table 4.30, $L_{proposed,2}$ (4.80) has an average of 0.5cm lower accuracy compared to $L_{proposed,1}$ (4.79). Ideally, $L_{proposed,1}$ should have higher accuracy than $L_{proposed,2}$ as $L_{proposed,1}$ follows the kinematic equation. However, mainly due to the lack of direct horizontal acceleration information from the shank's IMU, $L_{proposed,1}$ is not the exact kinematic equation. Although this horizontal acceleration information is missing, stride length can still be estimated accurately with a low absolute mean error of 4.2cm by weighing each important feature in $L_{proposed,2}$.

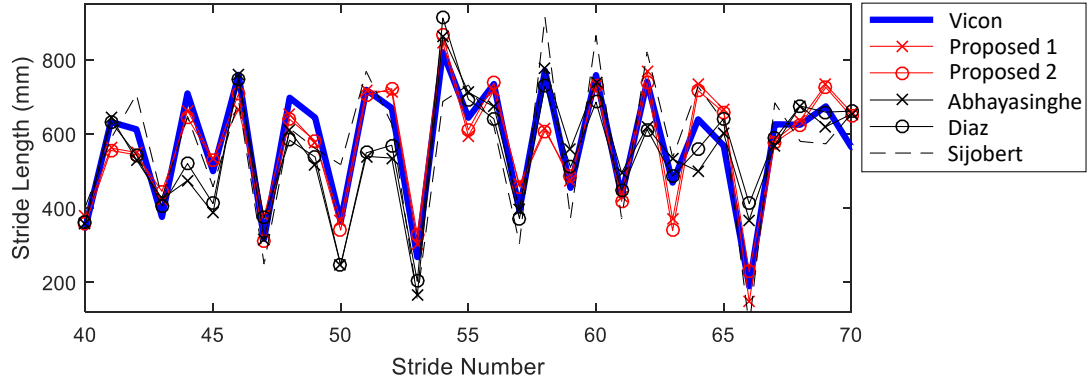


Fig. 4.78: Estimated stride lengths.

Table 4.30: Comparison among different methods.

Estimation Error	$L_{\text{proposed},1}$	$L_{\text{proposed},2}$	$L_{\text{Abhayasinghe}}$	L_{Diaz}	L_{Sijobert}
MAE (mm)	46.93	41.94	69.71	76.24	80.20
STD (mm)	57.67	54.51	88.19	93.79	49.20

The IMU data collected in this research is also used to compare the proposed method with the existing algorithms listed in Chapter 2.4.6, which are based on the thigh or shank's IMU data. However, IMU data for upper part of body was not collected meaning that it is unable to replicate the existing methods which are based on the IMU data collected at the upper part of body.

Referring to Table 4.31, the proposed method also has the lowest MAE compared to $L_{\text{Abhayasinghe}}$, L_{Diaz} , and L_{Sijobert} . It must be noted that the results for the proposed method, $L_{\text{Abhayasinghe}}$ and L_{Diaz} are obtained and compared by finding the generalized parameters w and b for all participants through optimization algorithm instead of using personalized parameters. For example, in $L_{\text{Abhayasinghe}}$ (2.13), if personalized parameters $w_1 = 2 \times \text{length of left leg}$, and $w_2 = 2 \times \text{length of right leg}$ are used, a lower mean error of 5.4cm was reported [51].

Table 4.31 shows different features used for different methods. An advantage of the proposed method is that it does not require an accurate estimation of angle. The only needs of angle in the proposed method is for gait cycle extraction, which can also be accomplished with non-accurate drifted angle or zero crossings of angular velocity. Instead of using angle as a feature which is required in existing methods $L_{\text{Abhayasinghe}}$, L_{Diaz} and L_{Sijobert} , the mean and summation of raw angular velocity collected from the

IMU are used. This means that the proposed method is computationally efficient because no data filtration is required while angle estimation would have required more complex computations.

Table 4.31: Different types of features used in different methods.

Method	Features			
$L_{\text{proposed},1}$	$\bar{\omega}_{z,\text{flexion}}$	$\sum \omega_z$	$t_{\text{extension}}$	
$L_{\text{proposed},2}$				
$L_{\text{Abhayasinghe}}$	φ_{max}	φ_{min}		
L_{Diaz}				
L_{Sijobert}	θ	a_x	a_y	ω_z

ω_z denotes shank's angular velocity, φ denotes thigh angle, θ denotes shank angle, and a denotes acceleration measured by the IMU.

4.7.5 Summary

A new method to estimate the stride length based on a single shank's gyroscope was proposed. In this research, it was identified that the average shank's angular velocity during the shank's flexion and the summation of shank's angular velocity during the whole gait cycle are two important features for stride length estimation. The duration of the shank's extension, rather than the whole duration of the gait cycle, was used as the third feature because the horizontal distance of the shank increased mostly during the shank's extension. The proposed method had a low MAE of 4.2cm with a standard deviation of 5.5cm.

CHAPTER 5 – CONCLUSIONS AND FUTURE WORK

5.1 Conclusions

The main purpose of this thesis is to develop gait analysis methods using IMUs. Currently, gait diagnosis is done based on visual inspection which is subjective and dependent on the experience of clinicians, while other existing technologies such as optical motion capture system are expensive. Therefore, in this research, low-cost IMUs were designed and constructed to perform gait analysis autonomously. The gyroscopes and accelerometers in the IMUs were synchronized and sampled at 100Hz. The wireless data transmission loss of the IMUs was almost 0% when the IMUs and dongle were 5 meters apart. When the IMU-dongle separation was 19 meters, the data loss was also low at 1 to 2%.

After the IMUs were built, a 3-D thigh and shank angles estimation algorithm, called 2-point error estimation algorithm, was proposed. This algorithm estimated the gyroscope drifting error based on pre- and post-calibration, and assumed that the drifting error was linear. Validated against the gold standard Vicon optical motion capture system in Curtin Australia's Motion Analysis Lab, the proposed algorithm resulted in low average RMSE of 2.9°, 3.6°, and 4.2° for flexion/extension, adduction/abduction, and internal/external rotation angles of the thigh and shank, respectively. The estimated angle waveforms patterns were also very similar to that from Vicon system without smoothing because the proposed algorithm did not require the gyroscope data to be filtered. In term of computational efficiency, only two "atan2()" functions were need to be computed throughout the whole walking motion, and 7 additions and 4 multiplications to estimate each angle.

The estimated 3-D thigh and shank angles were then used as features of machine learning algorithms (random forest, k-nearest neighbor, support vector machine, and perceptron) to design a standalone gait diagnosis device. The standalone device was built using low-end microcontrollers to reduce the cost (total cost of device ≈US\$8). It lit up green and red LEDs when the gait was normal and abnormal, respectively. Perceptron was chosen for the device as it resulted in the top two highest accuracy, and required the least amount of memory and computations among the machine learning algorithms compared. It was discovered that the adduction/abduction angle was able to improve the classification accuracy, but internal/external rotation angles of the thigh and shank did not help to improve the accuracy in this research. The combination of the thigh and shank's flexion/extension angles, and shank's

adduction/abduction angle were selected as the input features of the perceptron as this combination resulted in the highest mean classification accuracy at 96.5%. This standalone device has great potential in real-time identification of abnormal gaits without the presence of medical practitioners.

Additionally, a novel gait phase detection method for normal and abnormal gaits was proposed. The local maxima, minima and zero crossings of the shank's angular velocity and acceleration were used to detect heel strike, toe strike, and toe off. Instead of classifying the whole stride, some unique waveform patterns of the normal/abnormal shank's angular velocity were identified to classify the heel strike and toe strike as normal/abnormal. This may provide insights into the shank's angular velocity waveform patterns that are human-understandable to assist clinicians in walking evaluation. Comparing with an existing method that placed force sensitive resistors under the foot to detect gait phases, the mean absolute sample difference between the proposed and existing methods was low at around 2 sample difference, i.e. 20ms difference. The classification accuracy of the proposed method was also high at about 94.4%. The main advantage of the proposed method was both normal and abnormal gaits were considered, while many existing IMU-based gait phase detection methods considered normal gaits only.

Moreover, a method to mathematically express the normal and abnormal thigh and shank angle waveforms was proposed. The angle waveforms were time and amplitude scaled before performing DFT. By doing so, the reconstructed waveforms were able to represent the original waveforms more accurately than conventional method without increasing the number of harmonics. As a comparison, when the number of harmonics was 10, the CORR of the reconstructed waveforms based on proposed method was above 99.9% for normal and abnormal thigh and shank angles, while the conventional method achieved lower CORR about 99.5% for normal angles and below 99.8% for abnormal angles. The proposed method used 4 to 14 less DFT computations than conventional method to achieve the same CORR. The reconstructed waveforms based on proposed method were also able to detect normal and abnormal gait phases more accurately than the conventional method. The true positive rate of the gait multi-class classification was also increased by 5 to 7% when distinctive regions of the angle waveforms were enlarged.

Furthermore, a method to temporally synchronize video and IMU data was proposed. The synchronization was achieved by matching the maximum backward

swing of the leg detected from video and IMU. The detection of the maximum backward swings of leg from videos was achieved by comparing the motion between the upper and lower body of the person. The backward swings detection from IMUs was done by finding the local minima of the shank or foot angle. This proposed method was validated by blinking an LED connected to the IMUs and encoding an LED flag in the IMU wireless data transmission at the same time. The absolute synchronization error of the proposed method was low at 0 ± 2 frames. The synchronized joint angle information obtained from the IMUs was placed side-by-side to the video for the clinicians to perform visual inspection.

Finally, a new stride length estimation algorithm based on a single gyroscope attached to the shank was proposed. It was noticed from the Vicon optical motion capture system that the absolute horizontal position of reflective markers placed on the shank's IMU remained during the shank's extension, then increased almost linearly during the shank's flexion. By applying a linear kinematics equation, 3 new features that could be extracted from a single shank's gyroscope were identified for stride length estimation. The new features are the average angular velocity during shank's flexion, the summation of angular velocity during one whole stride, and the duration of the shank's extension. Validated against the Vicon system, this proposed method had resulted in a low MAE of 4.2cm with a standard deviation of 5.5cm.

It can be concluded that the accuracies of the IMUs in gait analysis are comparable to gold standard such as Vicon optical motion capture system when proper algorithms are used. Other than having high accuracies, the proposed methods have lower computational requirements, and thus can be applied on low end embedded devices to reduce the costs. Both applied and fundamental researches have been presented in this thesis, and the main contribution is an IMU-based system that detects and classifies a selection of gait anomalies to assist the medical practitioners in early diagnosis of walking disorders.

5.2 Future Work

The proposed 3-D angle estimation algorithm was designed and only tested to estimate 3-D angles of a person conducting one activity, i.e. walking in a straight line. The gyroscope drifting error was compensated by assuming the error drifting direction was linear. Although this assumption was suitable to estimate the 3-D angles of a person walking, it might not be the case if the person performed a series of motions

such as sit, stand, jump, walk, then run. The error drifting direction is expected to be linear as long as the user is performing the same activity, then changes gradient when the user performs a different activity. The future direction is to extend the proposed method to estimate 3-D angles when the user performs multiple activities. A possible solution is that the angles could be updated using accelerometer data when certain conditions are fulfilled, instead of just during the person is standing.

The standalone gait diagnosis device could only diagnose certain types of walking patterns because the perceptron was only trained with 4 patterns. It was shown that the accuracy of the device improved when more types of walking pattern were involved in the training. However, at the time of writing, there are still very little public gait dataset for training. The collaboration with hospitals is essential in collecting different types of abnormal walking patterns, not only for the improvement of the standalone device, but to make the dataset available to the public.

This thesis presented heel strike, toe strike and toe off detections using a single shank's IMU. However, heel off detection using IMUs has yet to be discovered. As of today, the detection of heel off using IMUs is still not well-researched. In future, the IMU can be placed on the foot in an attempt to detect heel off, as well as other gait phases. It is recommended to place the IMU on the foot rather than the shank for future gait phase detection because the toe and heel are parts of the foot, and the IMU can be built inside the shoes for long term monitoring.

It was demonstrated that the harmonic components of the scaled waveforms based on proposed method can be used to increase the gait classification accuracy when distinctive regions of the waveforms were extracted. Future works include but not limited to extracting multiple regions of the waveforms, improving how the regions are being extracted, and resampling the regions with different ratios. These suggested future works are expected to further improve the accuracy of gait phase detection and gait classification.

The front view of the user is essential for visual inspection, but the proposed synchronization method can only synchronize IMU data and video that is captured from the side view of the users for maximum backward swing detection. In future, it is planned to temporally synchronize the video and IMU data when the video is captured from the front. It is expected that the motion of the users as seen from the front view camera will be increased horizontally and vertically for each walking step increment. The horizontal or vertical change in motion may be used for

synchronization.

The proposed stride length estimation was based on an assumption that the gyroscope axis direction is always pointing horizontally sideways to measure the flexion/extension angular velocity. Although this assumption was proven accurate for normal stride length estimation, abnormal gaits may cause the gyroscope axis direction to change. In future, pre-processing of the gyroscope data is needed to calculate the resultant flexion/extension angular velocity in the global axis, i.e. pointing horizontally sideways. The calculations of the resultant angular velocity may require tri-axial gyroscope and accelerometer measurements.

REFERENCES

- [1] E. E. Reber, R. L. Michell, and C. J. Carter, "World Report on Disability," World Health Organization, and World Bank Group, 2011. Available: http://www.who.int/disabilities/world_report/2011/report/en/
- [2] Hashimoto, K., Higuchi, K., Nakayama, Y., & Abo, M. (2007). Ability for basic movement as an early predictor of functioning related to activities of daily living in stroke patients. *Neurorehabilitation and Neural Repair*, 21(4), 353-357.
- [3] A. Muro-de-la-Herran, B. Garcia-Zapirain and A. Mendez-Zorrilla. Gait analysis methods: An overview of wearable and non-wearable systems, highlighting clinical applications. *Sensors* 14(2), pp. 3362-3394. 2014. doi: 10.3390/s140203362.
- [4] T. Krosshaug *et al*, "Estimating 3D joint kinematics from video sequences of running and cutting maneuvers--assessing the accuracy of simple visual inspection," *Gait Posture*, vol. 26, (3), pp. 378-385, 2007.
- [5] D. Knudson, "Fundamentals of Biomechanics". Springer Science & Business Media, 2013, pp. 10.
- [6] J. Perry and J. M. Burnfield, *Gait Analysis: Normal and Pathological Function*, 2nd ed. Thorofare, New Jersey: SLACK Incorporated, 2010.
- [7] U. Martinez-Hernandez, I. Mahmood and A. A. Dehghani-Sanij, "Simultaneous Bayesian Recognition of Locomotion and Gait Phases With Wearable Sensors," in *IEEE Sensors Journal*, vol. 18, no. 3, pp. 1282-1290, Feb.1, 1 2018. doi: 10.1109/JSEN.2017.2782181
- [8] A. Behboodi, H. Wright, N. Zahradka and S. C. K. Lee, "Seven phases of gait detected in real-time using shank attached gyroscopes," *2015 37th Annual International Conference of the IEEE Engineering in Medicine and Biology Society (EMBC)*, Milan, 2015, pp. 5529-5532. doi: 10.1109/EMBC.2015.7319644
- [9] C. Senanayake and S. M. N. A. Senanayake, "A computational method for reliable gait event detection and abnormality detection for feedback in rehabilitation," *Comput. Methods Biomech. Biomed. Engin.*, vol. 14, (19), pp. 863-874, 2011. doi: 10.1080/10255842.2010.499866
- [10] C. MacDonald, D. Smith, R. Brower, M. Ceberio and T. Sarkodie-Gyan, "Determination of Human Gait Phase Using Fuzzy Inference," *2007 IEEE 10th*

International Conference on Rehabilitation Robotics, Noordwijk, 2007, pp. 661-665.

doi: 10.1109/ICORR.2007.4428495

- [11] J. D. Farah, N. Baddour and E. D. Lemaire, "Gait phase detection from thigh kinematics using machine learning techniques," *2017 IEEE International Symposium on Medical Measurements and Applications (MeMeA)*, Rochester, MN, 2017, pp. 263-268.
doi: 10.1109/MeMeA.2017.7985886
- [12] I. P. I. Pappas, M. R. Popovic, T. Keller, V. Dietz and M. Morari, "A reliable gait phase detection system," in *IEEE Transactions on Neural Systems and Rehabilitation Engineering*, vol. 9, no. 2, pp. 113-125, June 2001.
doi: 10.1109/7333.928571
- [13] J. S. Wang, C. W. Lin, Y. T. C. Yang and Y. J. Ho, "Walking Pattern Classification and Walking Distance Estimation Algorithms Using Gait Phase Information," in *IEEE Transactions on Biomedical Engineering*, vol. 59, no. 10, pp. 2884-2892, Oct. 2012.
doi: 10.1109/TBME.2012.2212245
- [14] Y. Qi, C. B. Soh, E. Gunawan, K. S. Low and R. Thomas, "Assessment of Foot Trajectory for Human Gait Phase Detection Using Wireless Ultrasonic Sensor Network," in *IEEE Transactions on Neural Systems and Rehabilitation Engineering*, vol. 24, no. 1, pp. 88-97, Jan. 2016.
doi: 10.1109/TNSRE.2015.2409123
- [15] M. Nordin and V. H. Frankel, *Basic Biomechanics of the Musculoskeletal System*. Lippincott Williams & Wilkins, 2001, pp. 439.
- [16] M. Jagodzinski *et al*, "Experimental and clinical assessment of the accuracy of knee extension measurement techniques," *Knee Surgery, Sports Traumatology, Arthroscopy*, vol. 8, (6), pp. 329-36, 2000.
doi: 10.1007/s001670000150
- [17] J. Z. Edwards *et al*, "Measuring flexion in knee arthroplasty patients," *J. Arthroplasty*, vol. 19, (3), pp. 369-372, 2004.
- [18] S. Boukhenous, M. Attari and Y. Remram, "Force platform for postural balance analysis," *2012 11th International Conference on Information Science, Signal Processing and their Applications (ISSPA)*, Montreal, QC, 2012, pp. 854-858.
doi: 10.1109/ISSPA.2012.6310673

- [19] N. Mijailovic, R. Radakovic, A. Peulic, I. Milankovic and N. Filipovic, "Using force plate, computer simulation and image alignment in jumping analysis," *2015 IEEE 15th International Conference on Bioinformatics and Bioengineering (BIBE)*, Belgrade, 2015, pp. 1-4. doi: 10.1109/BIBE.2015.7367672
- [20] "Motion Capture Systems", *VICON*, 2018. [Online]. Available: <https://www.vicon.com/>. [Accessed: 16 Oct. 2018].
- [21] "PhaseSpace", *Meta Motion*, 2018. [Online]. Available: <http://metamotion.com/>. [Accessed: 16 Oct. 2018].
- [22] "OptiTrack", *OptiTrack*, 2018. [Online]. Available: <https://optitrack.com/>. [Accessed: 16 Oct. 2018].
- [23] J. Cockcroft, J. H. Muller and C. Scheffer, "A Novel Complimentary Filter for Tracking Hip Angles During Cycling Using Wireless Inertial Sensors and Dynamic Acceleration Estimation," in *IEEE Sensors Journal*, vol. 14, no. 8, pp. 2864-2871, Aug. 2014. doi: 10.1109/JSEN.2014.2318897
- [24] Z. Huo *et al.*, "Examining the feasibility of a Microsoft Kinect™ based game intervention for individuals with anterior cruciate ligament injury risk," *2015 37th Annual International Conference of the IEEE Engineering in Medicine and Biology Society (EMBC)*, Milan, 2015, pp. 7059-7062. doi: 10.1109/EMBC.2015.7320018
- [25] D. Roetenberg, H. J. Luinge, C. T. M. Baten and P. H. Veltink, "Compensation of magnetic disturbances improves inertial and magnetic sensing of human body segment orientation," in *IEEE Transactions on Neural Systems and Rehabilitation Engineering*, vol. 13, no. 3, pp. 395-405, Sept. 2005. doi: 10.1109/TNSRE.2005.847353
- [26] "Compass Heading using Magnetometers", *Honeywell*, 2018. [Online]. Available: https://cdn-shop.adafruit.com/datasheets/AN203_Compass_Heading_Using_Magnetometers.pdf. [Accessed: 16 Oct. 2018].
- [27] E. R. Bachmann, Xiaoping Yun and C. W. Peterson, "An investigation of the effects of magnetic variations on inertial/magnetic orientation sensors," *Robotics and Automation, 2004. Proceedings. ICRA '04. 2004 IEEE International Conference on*, 2004, pp. 1115-1122 Vol.2.

doi: 10.1109/ROBOT.2004.1307974

- [28] W. Geiger *et al.*, "MEMS IMU for AHRS applications," *2008 IEEE/ION Position, Location and Navigation Symposium*, Monterey, CA, 2008, pp. 225-231.
doi: 10.1109/PLANS.2008.4569973
- [29] R. E. Mayagoitia, A. V. Nene and P. H. Veltink, "Accelerometer and rate gyroscope measurement of kinematics: an inexpensive alternative to optical motion analysis systems," *J. Biomech.*, vol. 35, (4), pp. 537-542, 2002.
Available:
<http://www.sciencedirect.com/science/article/pii/S0021929001002317S>.
- [30] M. De Marsico, D. De Pasquale and A. Mecca, "Embedded Accelerometer Signal Normalization for Cross-Device Gait Recognition," *2016 International Conference of the Biometrics Special Interest Group (BIOSIG)*, Darmstadt, 2016, pp. 1-5.
doi: 10.1109/BIOSIG.2016.7736920
- [31] N. Abhayasinghe and I. Murray, "Human gait phase recognition based on thigh movement computed using IMUs," *2014 IEEE Ninth International Conference on Intelligent Sensors, Sensor Networks and Information Processing (ISSNIP)*, Singapore, 2014, pp. 1-4.
doi: 10.1109/ISSNIP.2014.6827604
- [32] H. J. Luinge and P. H. Veltink, "Measuring orientation of human body segments using miniature gyroscopes and accelerometers," *Medical and Biological Engineering and Computing*, vol. 43, (2), pp. 273-82, 2005.
doi: <http://dx.doi.org/dbgw.lis.curtin.edu.au/10.1007/BF02345966>.
- [33] K. P. Hopkins, "Low Cost AHRS and GPS/IMU Integration using Kalman Filtering for Autonomous Vehicle Navigation." Order No. 1508359, University of Rhode Island, Ann Arbor, 2012.
- [34] S. O. H. Madgwick, A. J. L. Harrison and R. Vaidyanathan, "Estimation of IMU and MARG orientation using a gradient descent algorithm," *2011 IEEE International Conference on Rehabilitation Robotics*, Zurich, 2011, pp. 1-7.
doi: 10.1109/ICORR.2011.5975346
- [35] K. Tong and M. H. Granat, "A practical gait analysis system using gyroscopes," *Med. Eng. Phys.*, vol. 21, (2), pp. 87-94, 1999.
- [36] Wu, Z. Sun, W. Zhang, and Q. Chen, "Attitude and gyro bias estimation by the

- rotation of an inertial measurement unit, " *Measurement Science and Technology*, Oct.27, 2015.
doi: 10.1088/0957-0233/26/12/125102
- [37] V. Bonnet, J. McCamley, C. Mazza and A. Cappozzo, "Trunk orientation estimate during walking using gyroscope sensors," *2012 4th IEEE RAS & EMBS International Conference on Biomedical Robotics and Biomechatronics (BioRob)*, Rome, 2012, pp. 367-372.
doi: 10.1109/BioRob.2012.6290821
- [38] R. S. McGinnis *et al.*, "Accuracy of Femur Angles Estimated by IMUs During Clinical Procedures Used to Diagnose Femoroacetabular Impingement," in *IEEE Transactions on Biomedical Engineering*, vol. 62, no. 6, pp. 1503-1513, June 2015.
doi: 10.1109/TBME.2015.2392758
- [39] Okita, Nori, and H. Sommer. "Angular acceleration of the foot during gait using an IMU." *Annual Meeting of American Society of Biomechanics (ASB)*. 2013.
- [40] T. N. Do, R. Liu, C. Yuen, M. Zhang and U. X. Tan, "Personal Dead Reckoning Using IMU Mounted on Upper Torso and Inverted Pendulum Model," in *IEEE Sensors Journal*, vol. 16, no. 21, pp. 7600-7608, Nov.1, 2016.
doi: 10.1109/JSEN.2016.2601937
- [41] P. K. Yoon, S. Zihajehzadeh, B. S. Kang and E. J. Park, "Robust Biomechanical Model-Based 3-D Indoor Localization and Tracking Method Using UWB and IMU," in *IEEE Sensors Journal*, vol. 17, no. 4, pp. 1084-1096, Feb.15, 15 2017.
doi: 10.1109/JSEN.2016.2639530
- [42] Z. Chen, G. Li, F. Fioranelli and H. Griffiths, "Personnel Recognition and Gait Classification Based on Multistatic Micro-Doppler Signatures Using Deep Convolutional Neural Networks," in *IEEE Geoscience and Remote Sensing Letters*, vol. 15, no. 5, pp. 669-673, May 2018.
doi: 10.1109/LGRS.2018.2806940
- [43] V. Mikos *et al.*, "Real-Time Patient Adaptivity for Freezing of Gait Classification Through Semi-Supervised Neural Networks," *2017 16th IEEE International Conference on Machine Learning and Applications (ICMLA)*, Cancun, 2017, pp. 871-876.
doi: 10.1109/ICMLA.2017.00-46
- [44] O. Costilla-Reyes, P. Scully and K. B. Ozanyan, "Deep Neural Networks for

- Learning Spatio-Temporal Features From Tomography Sensors," in *IEEE Transactions on Industrial Electronics*, vol. 65, no. 1, pp. 645-653, Jan. 2018. doi: 10.1109/TIE.2017.2716907
- [45] E. Dolatabadi, B. Taati and A. Mihailidis, "An Automated Classification of Pathological Gait Using Unobtrusive Sensing Technology," in *IEEE Transactions on Neural Systems and Rehabilitation Engineering*, vol. 25, no. 12, pp. 2336-2346, Dec. 2017. doi: 10.1109/TNSRE.2017.2736939
- [46] D. Slijepcevic *et al.*, "Automatic Classification of Functional Gait Disorders," in *IEEE Journal of Biomedical and Health Informatics*, Dec 2017. doi: 10.1109/JBHI.2017.2785682
- [47] N. Poschadel, S. Moghaddamnia, J. C. Alcaraz, M. Steinbach and J. Peissig, "A dictionary learning based approach for gait classification," *2017 22nd International Conference on Digital Signal Processing (DSP)*, London, 2017, pp. 1-4. doi: 10.1109/ICDSP.2017.8096121
- [48] M. C. Mazzaro, M. Sznaier and O. Camps, "A model (in)validation approach to gait classification," in *IEEE Transactions on Pattern Analysis and Machine Intelligence*, vol. 27, no. 11, pp. 1820-1825, Nov. 2005. doi: 10.1109/TPAMI.2005.210
- [49] S. C. Mukhopadhyay, "Wearable Sensors for Human Activity Monitoring: A Review," in *IEEE Sensors Journal*, vol. 15, no. 3, pp. 1321-1330, March 2015. doi: 10.1109/JSEN.2014.2370945
- [50] H. F. Maqbool, M. A. B. Husman, M. I. Awad, A. Abouhossein, N. Iqbal and A. A. Dehghani-Sanij, "A Real-Time Gait Event Detection for Lower Limb Prosthesis Control and Evaluation," in *IEEE Transactions on Neural Systems and Rehabilitation Engineering*, vol. 25, no. 9, pp. 1500-1509, Sept. 2017. doi: 10.1109/TNSRE.2016.2636367
- [51] N. Abhayasinghe, "Human Gait Modelling with Step Estimation and Phase Classification Utilising a Single Thigh Mounted IMU for Vision Impaired Indoor Navigation," Ph.D. dissertation, Dept. Elect. Eng., Curtin Univ., Australia, 2016.
- [52] R. K. Ibrahim, E. Ambikairajah, B. Celler, N. H. Lovell and L. Kilmartin, "Gait patterns classification using spectral features," *IET Irish Signals and Systems*

- Conference (ISSC 2008)*, Galway, 2008, pp. 98-102.
doi: 10.1049/cp:20080645
- [53] A. Mostayed, M. Mynuddin, G. Mazumder, Sikyung Kim and Se Jin Park, "Abnormal Gait Detection Using Discrete Fourier Transform," *2008 International Conference on Multimedia and Ubiquitous Engineering (mue 2008)*, Busan, 2008, pp. 36-40.
doi: 10.1109/MUE.2008.59
- [54] M. D. Latt *et al*, "Acceleration Patterns of the Head and Pelvis During Gait in Older People With Parkinson's Disease: A Comparison of Fallers and Nonfallers," *The Journals of Gerontology*, vol. 64A, (6), pp. 700-6, 2009.
doi: 10.1093/gerona/ glp009
- [55] H. B. Lim, K. H. Hoon, Y. C. Soh, A. Tow and K. H. Low, "Gait planning for effective rehabilitation - From gait study to application in clinical rehabilitation," *2009 IEEE International Conference on Rehabilitation Robotics*, Kyoto, 2009, pp. 271-276.
doi: 10.1109/ICORR.2009.5209599
- [56] H. Vallery, E. H. F. van Asseldonk, M. Buss and H. van der Kooij, "Reference Trajectory Generation for Rehabilitation Robots: Complementary Limb Motion Estimation," in *IEEE Transactions on Neural Systems and Rehabilitation Engineering*, vol. 17, no. 1, pp. 23-30, Feb. 2009.
doi: 10.1109/TNSRE.2008.2008278
- [57] H. Wang and Y. Li, "Gait planning and control of a biped robot walking up and down stairs," *Shandong Daxue Xuebao (GongxueBan) / Journal of Shandong University (Engineering Science)*, vol. 44, (2), pp. 57-62, 2014.
doi: 10.6040/j.issn.1672-3961.0.2013.147
- [58] Shih-Kai Chung and J. K. Hahn, "Animation of human walking in virtual environments," *Proceedings Computer Animation 1999*, Geneva, Switzerland, 1999, pp. 4-15.
doi: 10.1109/CA.1999.781194
- [59] L. Ren, R. K. Jones and D. Howard, "Predictive modelling of human walking over a complete gait cycle," *J. Biomech.*, vol. 40, (8), pp. 1567-1574, 2007.
- [60] D. Chew, D. Gouwanda and A. A. Gopalai, "Investigating running gait using a shoe-integrated wireless inertial sensor," *TENCON 2015 - 2015 IEEE Region*

- 10 Conference, Macao, 2015, pp. 1-6.
doi: 10.1109/TENCON.2015.7373054
- [61] H. Qiuyang and Y. Zaiyue, "Frequency-Estimation-Based Thigh Angle Prediction in Level-Ground Walking Using IMUs," *2013 International Conference on Cyber-Enabled Distributed Computing and Knowledge Discovery*, Beijing, 2013, pp. 277-282.
doi: 10.1109/CyberC.2013.54
- [62] T. Wark, M. Karunanithi and W. Chan, "A Framework for Linking Gait Characteristics of Patients with Accelerations of the Waist," *2005 IEEE Engineering in Medicine and Biology 27th Annual Conference*, Shanghai, 2005, pp. 7695-7698.
doi: 10.1109/IEMBS.2005.1616295
- [63] T. P. Luu, H. B. Lim, X. Qu, K. H. Hoon and K. H. Low, "Subject-specific lower limb waveforms planning via artificial neural network," *2011 IEEE International Conference on Rehabilitation Robotics*, Zurich, 2011, pp. 1-6.
doi: 10.1109/ICORR.2011.5975491
- [64] M. Sekine, T. Tamura, M. Akay, T. Fujimoto, T. Togawa and Y. Fukui, "Discrimination of walking patterns using wavelet-based fractal analysis," in *IEEE Transactions on Neural Systems and Rehabilitation Engineering*, vol. 10, no. 3, pp. 188-196, Sept. 2002.
doi: 10.1109/TNSRE.2002.802879
- [65] J. A. Hughes, J. A. Brown and A. M. Khan, "Smartphone gait fingerprinting models via genetic programming," *2016 IEEE Congress on Evolutionary Computation (CEC)*, Vancouver, BC, 2016, pp. 408-415.
doi: 10.1109/CEC.2016.7743823
- [66] A. Salarian *et al.*, "Gait assessment in Parkinson's disease: toward an ambulatory system for long-term monitoring," in *IEEE Transactions on Biomedical Engineering*, vol. 51, no. 8, pp. 1434-1443, Aug. 2004.
doi: 10.1109/TBME.2004.827933
- [67] C. Chen, R. Jafari and N. Kehtarnavaz, "UTD-MHAD: A multimodal dataset for human action recognition utilizing a depth camera and a wearable inertial sensor," *2015 IEEE International Conference on Image Processing (ICIP)*, Quebec City, QC, 2015, pp. 168-172.
doi: 10.1109/ICIP.2015.7350781

- [68] A. Farnoosh, M. Nabian, P. Closas and S. Ostadabbas, "First-person indoor navigation via vision-inertial data fusion," *2018 IEEE/ION Position, Location and Navigation Symposium (PLANS)*, Monterey, CA, 2018, pp. 1213-1222. doi: 10.1109/PLANS.2018.8373507
- [69] P. Jatesiktat, D. Anopas and W. T. Ang, "Personalized Markerless Upper-Body Tracking with a Depth Camera and Wrist-Worn Inertial Measurement Units," *2018 40th Annual International Conference of the IEEE Engineering in Medicine and Biology Society (EMBC)*, Honolulu, HI, 2018, pp. 1-6. doi: 10.1109/EMBC.2018.8513068
- [70] Jum-Han Bae and Jong-Tae Kim, "Design and implementation of high accurate synchronization between gyroscope and image sensor," *2015 Seventh International Conference on Ubiquitous and Future Networks*, Sapporo, 2015, pp. 956-958. doi: 10.1109/ICUFN.2015.7182687
- [71] T. Plotz, C. Chen, N. Y. Hammerla and G. D. Abowd, "Automatic Synchronization of Wearable Sensors and Video-Cameras for Ground Truth Annotation -- A Practical Approach," *2012 16th International Symposium on Wearable Computers*, Newcastle, 2012, pp. 100-103. doi: 10.1109/ISWC.2012.15
- [72] E. Cippitelli *et al.*, "Time synchronization and data fusion for RGB-Depth cameras and inertial sensors in AAL applications," *2015 IEEE International Conference on Communication Workshop (ICCW)*, London, 2015, pp. 265-270. doi: 10.1109/ICCW.2015.7247189
- [73] Y. K. Ryu and C. Oh, "RF Signal Synchronized Low Cost Motion Capture Device," *2007 Asia-Pacific Microwave Conference*, Bangkok, 2007, pp. 1-4. doi: 10.1109/APMC.2007.4554680
- [74] F. Ofli, R. Chaudhry, G. Kurillo, R. Vidal and R. Bajcsy, "Berkeley MHAD: A comprehensive Multimodal Human Action Database," *2013 IEEE Workshop on Applications of Computer Vision (WACV)*, Tampa, FL, 2013, pp. 53-60. doi: 10.1109/WACV.2013.6474999
- [75] X. Lin, V. Kitanovski, Q. Zhang and E. Izquierdo, "Enhanced multi-view dancing videos synchronisation," *2012 13th International Workshop on Image Analysis for Multimedia Interactive Services*, Dublin, 2012, pp. 1-4. doi: 10.1109/WIAMIS.2012.6226773

- [76] N. Q. K. Duong and F. Thudor, "Movie synchronization by audio landmark matching," *2013 IEEE International Conference on Acoustics, Speech and Signal Processing*, Vancouver, BC, 2013, pp. 3632-3636. doi: 10.1109/ICASSP.2013.6638335
- [77] M. Meribout, M. Nakanishi and T. Ogura, "A parallel algorithm for real-time object recognition," *Pattern Recognition Journal*, vol. 35, (18), pp. 1917-1931, 2002.
- [78] S. Hu and H. Zhang, "Image Edge Detection Based on FCM and Improved Canny Operator in NSST Domain," *2018 14th IEEE International Conference on Signal Processing (ICSP)*, Beijing, China, 2018, pp. 363-368. doi: 10.1109/ICSP.2018.8652426
- [79] X. Zhang, M. Ding and G. Fan, "Video-Based Human Walking Estimation Using Joint Gait and Pose Manifolds," in *IEEE Transactions on Circuits and Systems for Video Technology*, vol. 27, no. 7, pp. 1540-1554, July 2017. doi: 10.1109/TCSVT.2016.2527218
- [80] Y. Zhang, K. Chen, J. Yi, T. Liu and Q. Pan, "Whole-Body Pose Estimation in Human Bicycle Riding Using a Small Set of Wearable Sensors," in *IEEE/ASME Transactions on Mechatronics*, vol. 21, no. 1, pp. 163-174, Feb. 2016. doi: 10.1109/TMECH.2015.2490118
- [81] Taylor, M. E., Ketels, M. M., Delbaere, K., Lord, S. R., Mikolaizak, A. S., & Close, J. C. T. (2012). Gait impairment and falls in cognitively impaired older adults: an explanatory model of sensorimotor and neuropsychological mediators. *Age and Ageing*, 41(5), 665–669. doi:10.1093/ageing/afs057
- [82] A. R. Jimenez Ruiz, F. Seco Granja, J. C. Prieto Honorato and J. I. Guevara Rosas, "Accurate Pedestrian Indoor Navigation by Tightly Coupling Foot-Mounted IMU and RFID Measurements," in *IEEE Transactions on Instrumentation and Measurement*, vol. 61, no. 1, pp. 178-189, Jan. 2012. doi: 10.1109/TIM.2011.2159317
- [83] L. Hung-Huan and C. Liu, "Implementation of Wi-Fi Signal Sampling on an Android Smartphone for Indoor Positioning Systems," *Sensors*, vol. 18, (1), pp. 3, 2018. doi: 10.3390/s18010003.
- [84] M. Ji, J. Kim, J. Jeon and Y. Cho, "Analysis of positioning accuracy

- corresponding to the number of BLE beacons in indoor positioning system," *2015 17th International Conference on Advanced Communication Technology (ICACT)*, Seoul, 2015, pp. 92-95. doi: 10.1109/ICACT.2015.7224764
- [85] M. A. Al-Ammar *et al.*, "Comparative Survey of Indoor Positioning Technologies, Techniques, and Algorithms," *2014 International Conference on Cyberworlds*, Santander, 2014, pp. 245-252. doi: 10.1109/CW.2014.41
- [86] H. Weinberg, "Using the ADXL202 in Pedometer and Personal Navigation Applications," in *Analog Devices*, 2002. [Online]. Available: <http://www.bdtic.com/Download/ADI/AN-602.pdf>.
- [87] J. W. Kim, H. J. Jang, D. H. Hwang and C. Park, "A Step, Stride and Heading Determination for the Pedestrian Navigation System," in *Journal of Global Positioning Systems*, vol. 3, no. 1-2, pp. 273-279, Feb. 3, 2015. doi: 10.5081/jgps.3.1.273J.
- [88] Scarlett, "Enhancing the Performance of Pedometers Using a Single Accelerometer," in *Analog Devices*, 2007. [Online]. Available: http://www.bdtic.com/download/adi/47076299220991an_900.pdf.
- [89] Q. Ladetto, "On foot navigation: Continuous step calibration using both complementary recursive prediction and adaptive Kalman filtering," in *Proceedings of the 13th International Technical Meeting of the Satellite Division of The Institute of Navigation*, pp. 1735–1740, Sept. 19–22, 2000.
- [90] J. H. Lee, B. Shin, C. Kim, J. Kim, S. Lee and T. Lee, "Real time adaptive step length estimation for smartphone user," *2013 13th International Conference on Control, Automation and Systems (ICCAS 2013)*, Gwangju, 2013, pp. 382-385. doi: 10.1109/ICCAS.2013.6703929
- [91] E. M. Diaz and A. L. M. Gonzalez, "Step detector and step length estimator for an inertial pocket navigation system," *2014 International Conference on Indoor Positioning and Indoor Navigation (IPIN)*, Busan, 2014, pp. 105-110. doi: 10.1109/IPIN.2014.7275473
- [92] B. Sijobert *et al.*, "Implementation and Validation of a Stride Length Estimation Algorithm, Using a Single Basic Inertial Sensor on Healthy Subjects and Patients Suffering from Parkinson's Disease," *Health*, (7), pp. 704–714, 2015. doi: 10.4236/health.2015.76084.

- [93] J. Hannink *et al.*, "Mobile Stride Length Estimation With Deep Convolutional Neural Networks," in *IEEE Journal of Biomedical and Health Informatics*, vol. 22, no. 2, pp. 354-362, March 2018. doi: 10.1109/JBHI.2017.2679486
- [94] V. Renaudin, M. Susi and G. Lachapelle, "Step length estimation using handheld inertial sensors," *Sensors (Basel, Switzerland)*, vol. 12, (7), pp. 8507-8525, 2012.
- [95] *Invensense*, 2018. [Online]. Available: www.invensense.com. [Accessed: 16 Oct. 2018].
- [96] *Arduino*, 2018. [Online]. Available: <http://arduino.cc/>. [Accessed: 16 Oct. 2018].
- [97] "nRF24L01+ Single Chip 2.4GHz Transceiver Product Specification v1.0", *Nordic Semiconductor*, 2018. [Online]. Available: https://www.nordicsemi.com/eng/content/download/2726/34069/file/nRF24L01P_Product_Specification_1_0.pdf. [Accessed: 16 Oct. 2018].
- [98] "Compare iPhone Models", *Apple*, 2019. [Online]. Available: <https://www.apple.com/my/iphone/compare/>. [Accessed: 16 Jan. 2019].
- [99] K. Kawano, S. Kobashi, M. Yagi, K. Kondo, S. Yoshiya and Y. Hata, "Analyzing 3D Knee Kinematics Using Accelerometers, Gyroscopes and Magnetometers," *2007 IEEE International Conference on System of Systems Engineering*, San Antonio, TX, 2007, pp. 1-6. doi: 10.1109/SYSOSE.2007.4304332
- [100] M. Henriksson. (2013, Sept 16). Estimation of Heading using Magnetometers and GPS. [Online]. Available: <https://pdfs.semanticscholar.org/98f3/5084669a7d3926ea96e21e9389c1ce51661c.pdf>
- [101] H. Nguyen, K. Lebel, S. Bogard, E. Goubault, P. Boissy and C. Duval, "Using Inertial Sensors to Automatically Detect and Segment Activities of Daily Living in People With Parkinson's Disease," in *IEEE Transactions on Neural Systems and Rehabilitation Engineering*, vol. 26, no. 1, pp. 197-204, Jan. 2018. doi: 10.1109/TNSRE.2017.2745418
- [102] T. Oberg, A. Karsznia and K. Oberg, "Basic gait parameters: Reference data for normal subjects, 10–79 years of age," *J. Rehabil. Res. Dev.*, vol. 30, no. 2, pp. 210-223, 1993.

- [103] Y. Bengio, A. Courville, and P. Vincent. Representation learning: A review and new perspectives. *IEEE transactions on pattern analysis and machine intelligence*, 35(17):1798–1828, 2013.
- [104] J. K. Moore, S. K. Hnat and A. Vanden Bogert J., "An elaborate data set on human gait and the effect of mechanical perturbations," *PeerJ*, 2015.
doi: 10.7717/peerj.918.
- [105] C. Galvan-Duque et al., "Comparison between classical and intelligent identification systems for classification of gait events," *J. Control Science and Engineering*, vol. 1, pp. 21–34, 2015.
- [106] N. Mezghani, S. Husse, K. Boivin, K. Turcot, R. Aissaoui, N. Hagemeister, and J.A. de Guise. Automatic classification of asymptomatic and osteoarthritis knee gait patterns using kinematic data features and the nearest neighbor classifier. *IEEE transactions on biomedical engineering*, 55(3):1230–1232, 2008.
- [107] Kyoungchul Kong and Masayoshi Tomizuka, "Smooth and continuous human gait phase detection based on foot pressure patterns," *2008 IEEE International Conference on Robotics and Automation*, Pasadena, CA, 2008, pp. 3678-3683.
doi: 10.1109/ROBOT.2008.4543775
- [108] H. Huang, F. Zhang, L. J. Hargrove, Z. Dou, D. R. Rogers and K. B. Englehart, "Continuous Locomotion-Mode Identification for Prosthetic Legs Based on Neuromuscular–Mechanical Fusion," in *IEEE Transactions on Biomedical Engineering*, vol. 58, no. 10, pp. 2867-2875, Oct. 2011.
doi: 10.1109/TBME.2011.2161671
- [109] R. T. Lauer, B. T. Smith and R. R. Betz, "Application of a neuro-fuzzy network for gait event detection using electromyography in the child with Cerebral palsy," in *IEEE Transactions on Biomedical Engineering*, vol. 52, no. 9, pp. 1532-1540, Sept. 2005.
doi: 10.1109/TBME.2005.851527
- [110] Y. Tao, H. Hu and H. Zhou, "Integration of Vision and Inertial Sensors for 3D Arm Motion Tracking in Home-based Rehabilitation," *Int. J. Robotics Res.*, vol. 26, (6), pp. 607, 2007.
- [111] Teixeira T, Jung D, Savvides A (2010) Tasking networked cctv cameras and mobile phones to identify and localize multiple people. In: Proceedings of the 12th ACM international conference on Ubiquitous computing, Ubicomp '10, ACM, New York, NY, USA, pp 213–222

- [112] C. Jia and B. L. Evans, "Online Camera-Gyroscope Autocalibration for Cell Phones," in *IEEE Transactions on Image Processing*, vol. 23, no. 12, pp. 5070-5081, Dec. 2014.
doi: 10.1109/TIP.2014.2360120
- [113] E. Bertino and E. Ferrari, "Temporal synchronization models for multimedia data," in *IEEE Transactions on Knowledge and Data Engineering*, vol. 10, no. 4, pp. 612-631, July-Aug. 1998.
doi: 10.1109/69.706060
- [114] Y. C. Han, K. I. Wong and I. Murray, "Automatic Synchronization of Markerless Video and Wearable Sensors for Walking Assessment," in *IEEE Sensors Journal*, vol. 19, no. 17, pp. 7583-7590, Sept.1, 2019.
doi: 10.1109/JSEN.2019.2916163

Every reasonable effort has been made to acknowledge the owners of copyright material. I would be pleased to hear from any copyright owner who has been omitted or incorrectly acknowledged.